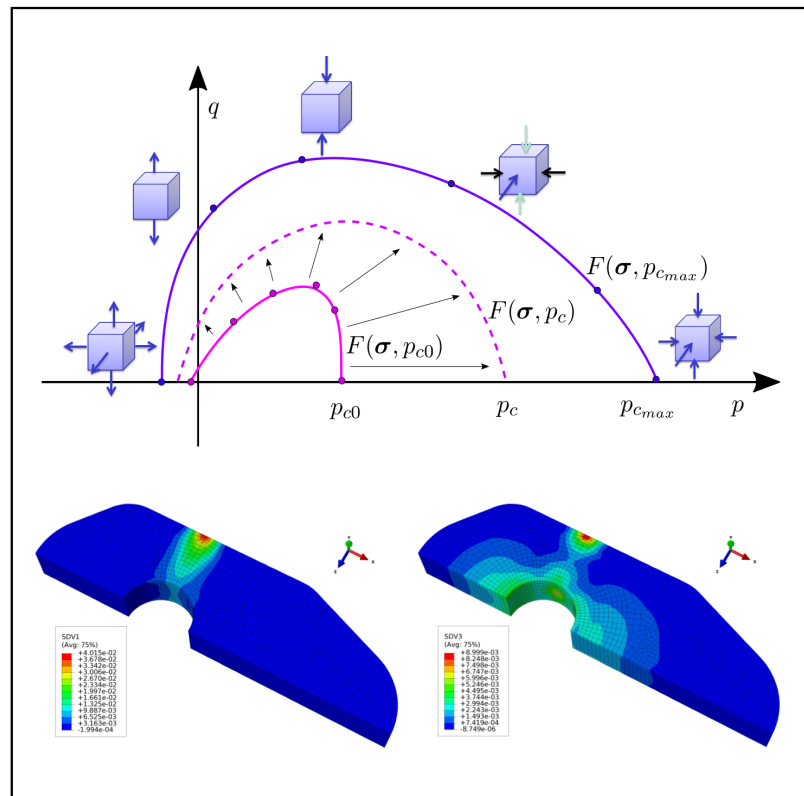


Massimo Penasa

Development of rate-dependent thermoplastic constitutive models for numerical analysis of ceramics at high-temperature



©2017 Massimo Penasa

UNIVERSITY OF TRENTO - Italy
Department of Civil, Environmental
and Mechanical Engineering



Doctoral School in Civil, Environmental and Mechanical Engineering
Topic 3. Modelling and Simulation - XXIX cycle 2015/2017

Doctoral Thesis - April 2017

Massimo Penasa

Development of rate-dependent thermoplastic constitutive models for numerical analysis of ceramics at high-temperature

Supervisor

Prof. Andrea Piccolroaz - University of Trento

Credits of the cover image: created by the author



Except where otherwise noted, contents on this book are licensed under a Creative
Common Attribution - Non Commercial - No Derivatives
4.0 International License

University of Trento
Doctoral School in Civil, Environmental and Mechanical Engineering
<http://web.unitn.it/en/dricam>
Via Mesiano 77, I-38123 Trento
Tel. +39 0461 282670 / 2611 - dicamphd@unitn.it

To my family

Acknowledgements

First and foremost, I owe my greatest gratitude to my advisor Professor Andrea Piccolroaz, for the constant and fundamental encouragements, suggestions and technical support he gave me throughout this research work. His great energy, friendship and overwhelming passion for Mechanics have contributed to my scientific and personal growth.

I also would like to take this occasion to thank Professor Davide Bigoni for having introduced me in the great environment of the Solid Mechanics Group and especially for having guided my research activity.

I am grateful to Dr. Francesco Dal Corso as the scientific coordinator of the European Research Project in which I have been involved.

Special thanks go to Dr. Severine Romero Baivier and all members of the Vesuvius Enabling Technology Group for their remarkable hospitality and great cooperation.

Moreover, I am highly thankful to Prof. Stanislaw Stupkiewicz and Prof. Jozse Korelc for their fundamental technical support in computational mechanics and in the use of AceGen.

Thanks go to Ing. Matteo Cova of Sacmi Imola S.C., Ing. Corrado Meante and Dr. Nuria Moral of Enginsoft S.p.A. for the cooperation.

Furthermore, I want to mention the fruitful collaboration with my brother Ing. Matteo Penasa and CAEmate Engineering.

Finally, the financial support from European Union FP7 project under contract number PIAPP-GA-2013-609758-HOTBRICKS is gratefully acknowledged.

Trento, April 7, 2017
Massimo Penasa

Published Papers

The main results presented in this thesis have been summarized in the following papers:

1. M. Penasa, A. Piccolroaz, L. Argani, D. Bigoni (2015).
Integration algorithms of elastoplasticity for ceramic powder compaction, *Journal of the European Ceramic Society*, **34**, 2775-2788.
2. M. Penasa, A. Piccolroaz, L. Argani, F. Dal Corso, D. Misseroni and M. Cova (2016).
Computational modelling and experimental validation of aluminum silicate forming by cold pressing, *Journal of the European Ceramic Society*, **36**, 2351-2362.
3. M. Penasa, A. Piccolroaz, F. Dal Corso, and D. Bigoni (2017).
An evolutionary thermoplastic constitutive model for compaction and pre-sintering of ceramics, (*Not yet submitted*).

Contents

1	Introduction	1
2	Theory of rate-dependent thermoplasticity	7
2.1	Plasticity	7
2.1.1	Unidimensional perfect plasticity	8
2.1.2	Plasticity with hardening	9
2.1.3	Incremental constitutive equations	12
2.2	Thermo-plasticity	14
2.2.1	Thermo-mechanical coupling	14
2.2.2	Incremental constitutive equations	16
2.3	Rate dependence	17
2.3.1	General concept: overstress and relaxation	18
2.3.2	Viscoplasticity equations	21
2.4	BP yield function	23
2.4.1	Definition	23
2.4.2	Shape distortion and flexibility	24
3	Numerical implementation	27
3.1	User-defined material models in Finite Element Codes	28
3.2	Stress-point integration algorithms for constitutive models with a pathological yield function	30
3.2.1	The ‘centre of mass’ integration algorithm	31
3.2.2	The ‘cutoff-substepping’ integration algorithm	35
3.2.3	Implicit BP yield function and return mapping algorithm	39
3.3	Numerical performance of the proposed algorithms	42
3.3.1	Finite step accuracy and iso-error maps	43
3.3.2	Robustness improvement with implicit BP yield function	48
3.4	Comparison with semi-analytical solutions of plastic benchmark problems	50

3.4.1	Compaction of a thick layer of perfectly-plastic material obeying the BP yield condition against a rigid spherical cup	52
3.4.2	Expansion of a perfectly plastic thick shell obeying the BP yield condition	57
3.5	Comparison with semi-analytical solutions of thermoplastic benchmark problems	60
3.5.1	Hot pressing of a thick layer of perfectly plastic ceramic powder against a rigid spherical mould	62
3.5.2	Thermal heating and expansion of a thick shell of perfectly plastic green body	69
4	Parameter identification through numerical optimization	75
4.0.1	Numerical optimization and objective function	76
4.0.2	Material parameters identification	78
4.0.3	DACE, sensitivity analysis and uncertainty quantification	80
4.1	Optimization algorithms	83
4.1.1	Classification	83
4.1.2	Choosing a method	84
4.1.3	Hybrid optimization	88
5	The constitutive model for cold forming of ceramic powders	91
5.1	Material	92
5.2	Constitutive framework for ceramic powder densification	92
5.2.1	Constitutive formulation	93
5.2.2	Finite Element implementation and integration of the material model into commercial FEM codes	96
5.3	Material parameter identification by simulation of experimental tests	97
5.3.1	Experimental tests on aluminum silicate powder	97
5.3.2	Simulation of uniaxial deformation tests	98
5.3.3	Simulation of compression and extension triaxial tests	99
5.3.4	Material parameter identification by multi objective optimization	101

5.4	Numerical simulation of industrial powder compaction processes	107
5.4.1	Experimental identification of friction coefficient between powder and die wall	107
5.4.2	Numerical simulation of axisymmetric tablet forming	108
5.4.3	Three-dimensional numerical simulation of an industrial tile forming process	112
5.4.4	Estimation of transversal load on the lateral die wall	114
5.4.5	Density distribution in a combed-finish tile after die pressing	115
6	The constitutive model for refractories	117
6.1	Thermoplastic Constitutive formulation	118
6.1.1	Elastic potential and temperature dependence	118
6.1.2	Temperature-dependent hyperbolic strain hardening and thermal softening	119
6.2	Strain softening for material failure description	120
6.2.1	Material damage and softening	121
6.2.2	Softening formulation	122
6.3	Strain limiter criterion	124
6.3.1	The Rankine strain limiter criterion	124
6.4	Material parameters identification	128
6.4.1	Temperature dependent elastic and thermal constants	128
6.4.2	BP yield function parameters	129
6.4.3	Hardening rule parameters through multi-objective optimization	133
6.4.4	Strain limiter criterion	136
6.5	Exploitation of the thermo-elasto-plastic model to describe the behavior of refractories under working conditions	137
6.5.1	Maximum bending load of a steel flow stopper	138
6.5.2	Slide gate thermal-stress analysis	142
6.5.3	VISO submerged pouring tubes thermal-stress analysis	147
7	The unified constitutive model for ceramic powder densification and pre-sintering	153
7.1	Thermo-plastic constitutive formulation	154
7.1.1	The evolution of the BP yield surface	154

- 7.1.2 Elastic potential and temperature dependence 157
- 7.1.3 Plastic potential and non-associative flow rule 157
- 7.1.4 Density-dependent strain hardening 158
- 7.1.5 Thermal softening 160
- 7.2 Experimental tests and FEA of cold forming and pre-sintering of alumina 161
 - 7.2.1 Forming of cylindrical green bodies 161
 - 7.2.2 Uniaxial compression tests at pre-sintering temperatures 162
 - 7.2.3 Thermo-mechanical FE analysis 162
- 7.3 Material parameters identification by inverse analysis 163
 - 7.3.1 Temperature dependent elastic modulus . . . 163
 - 7.3.2 Thermal softening 164
 - 7.3.3 Hardening laws 166
- 7.4 Results and comparison with experimental tests . . . 168

Bibliography **171**

List of Figures

2.1	Perfectly plastic uniaxial constitutive model.	8
2.2	Hardening behavior for metallic materials.	9
2.3	Example of yield surface and possible deformation increments.	11
2.4	Stress ‘jumps’ induced by changes in the strain rate during loading.	18
2.5	Example of creep deformation.	19
2.6	Conceptual illustration of rate-dependent plasticity. For a given strain increment, the viscoplastic solution is found between two limiting stress states: the ‘high rate’ solution σ^H which is the simple trial elastic stress and the ‘low rate solution’ corresponding to the quasistatic plastic solution.	20
2.7	Shape distortion of the BP yield function in the meridian and deviatoric planes and associated governing parameters.	25
3.1	The BP yield function represented as a surface in the p - q plane.	31
3.2	Radius $\rho(\theta)$ and centre of mass of two indicative deviatoric sections (located at different mean stresses p) of the BP yield surface. Due to the isotropy symmetries of the deviatoric sections, the mass centres lie on the hydrostatic axis.	32
3.3	Geometrical sketch of the ‘centre of mass return algorithm’ for the integration of rate elastoplastic constitutive equations.	33
3.4	Cutoff plane for the BP yield surface. Stress points where the return mapping algorithm works correctly are on the side of the plane where the yield surface lies. The false elastic domain is shown brown.	36

3.5 Determination of the position of the cutoff plane. Local stationary (maximum and minimum) and inflection points are denoted by black spots, while the bounds of the non-convex region (in which the Newton-Raphson algorithm can be still used) are shown gray. The dashed lines r_a and r_b are the tangent lines to the meridian function at the points P_a and P_b , respectively. The graph $\tilde{f}(\Phi)$ has been obtained with the following set of parameters: $M = 1$, $m = 3$, $\alpha = 1.5$, $p_c = 100$ MPa, and $c = 10$ MPa. 37

3.6 Construction of the implicit yield function F^* in the $p-q$ space. 39

3.7 A convex and smooth BP yield surface (left). Iso-surfaces of the corresponding implicit BP yield function in the principal stress space (right). The zero-level surface is marked in red color. 40

3.8 Prescribed finite strain steps in the strain-space (upper part) and corresponding elastic trial stresses in the deviatoric plane (central part) and meridian plane (lower part) of the stress-space, for tests 1 to 7 reported in Table 3.1. Finite steps are prescribed in such a way that the norm of the trial stress exceeds by 20% the norm of the corresponding yield stress along the radial path from the origin to the trial stress. . . . 44

3.9 Sections of the yield surface and local reference system employed for the construction of the iso-error maps. 46

3.10 Iso-error maps for Test 3 (see Tab. 3.1 and Fig. 3.8). 47

3.11 Iso-error maps for Test 4 (see Tab. 3.1 and Fig. 3.8). 47

3.12 Iso-error maps for Test 5 (see Tab. 3.1 and Fig. 3.8). 48

3.13 Iso-error maps for Test 6 (see Tab. 3.1 and Fig. 3.8). 48

3.14 Comparison of ‘cut-off-substepping’ and return mapping with implicit defined BP yield function: isotropic strength p_c and pushing head displacements u_1 in the numerical simulation of bending test on refractory steel flow stopper. The analysis with the ‘cut-off-substepping’ algorithm crashes before the end. 49

3.15 Geometry for the compaction of a thick perfectly-plastic layer of ceramic powder against a rigid cup (a) and for the expansion of a thick perfectly-plastic spherical shell under internal pressure (b). In both cases, the boundary of the plasticized zone is represented by δ which moves from $r = a$ to $r = b$ at increasing internal pressure Π . The reference system and stress components are shown in part (c). 51

3.16	Compaction of a perfectly-plastic thick layer, obeying von Mises and BP yield conditions, against a rigid spherical cup, representative of a ceramic powder. Upper part: radial (left) and polar (right) stress components as functions of the dimensionless radial position. Lower part: mean stress p (left) and deviatoric invariant q (right) as functions of the dimensionless radial position. Note that for the von Mises criterion $\sigma_0 = 33.86$ MPa has been chosen, so that the von Mises cylinder is circumscribed around the BP surface in the stress space.	56
3.17	Expansion of a perfectly-plastic thick spherical shell, obeying von Mises and BP yield conditions, representative of a green body. Upper part: radial (left) and polar (right) stress components as functions of the dimensionless radial position. Lower part: mean stress p (left) and deviatoric invariant q (right) as functions of the dimensionless radial position. Note that for the von Mises criterion $\sigma_0 = 100$ MPa has been chosen, so that the von Mises cylinder is circumscribed around the BP surface in the stress space.	59
3.18	Traces of the BP yield surface in the $(\sigma_r, \sigma_\theta)$ -plane for fourth values of temperature $T = 0, 190, 285,$ and 380°C (solid lines) and corresponding traces of the circumscribed Von Mises cylinder (dashed lines). Material parameters have been chosen to be representative of alumina powder.	63
3.19	Hot pressing of a perfectly plastic thick layer, obeying Von Mises and BP yield conditions, against a rigid spherical mould. Upper part: radial (left) and tangential (right) stresses as functions of the dimensionless radial position. Lower part: mean stress p (left) and deviatoric stress q (right) as functions of the dimensionless radial position.	67
3.20	Hot pressing of a perfectly plastic thick layer, obeying Von Mises and BP yield conditions, against a rigid spherical mould. Radial (left) and tangential (right) strains as functions of the dimensionless radial position.	68
3.21	Hot pressing of a perfectly plastic thick layer, obeying Von Mises and BP yield conditions, against a rigid spherical mould. Radial (left) and tangential (right) strains as functions of the dimensionless radial position.	69
3.22	Traces of the BP yield surface in the $(\sigma_r, \sigma_\theta)$ -plane for fourth values of temperature $T = 0, 190, 285,$ and 380°C (solid lines) and corresponding traces of the circumscribed Von Mises cylinder (dashed lines). Material parameters have been chosen to be representative of a green body partially densified.	70

3.23	Expansion of a thick shell of perfectly plastic green body subjected to both internal pressure and internal heating. Upper part: radial (left) and tangential (right) stresses as functions of the dimensionless radial position. Lower part: mean stress p (left) and deviatoric stress q (right) as functions of the dimensionless radial position.	73
3.24	Expansion of a thick shell of perfectly plastic green body subjected to both internal pressure and internal heating. Radial (left) and tangential (right) strains as functions of the dimensionless radial position.	73
4.1	Schematic representation of material parameter identification by inverse analysis.	80
4.2	Convergence rate and robustness for a selection of optimization algorithms.	84
4.3	Working mechanism of the pattern-search algorithm: a) the objective function is evaluated in a collection of directions; b) the system is re-centered to the best function evaluation point (red); c) if no improvement is achieved the step length is reduced.	86
4.4	Example of Pareto front for an optimization problem with two objective functions.	88
5.1	Simplified FE model for uniaxial compaction simulation. Undeformed mesh (left) and deformed mesh at the end of loading step (right, contours denote vertical displacement).	99
5.2	Simplified FE model for triaxial test simulation. Undeformed mesh (left), deformed mesh at the end of Stage 1 (forming of cylindrical specimen, centre) and deformed mesh at the end of Stage 2 (triaxial test, right). The contours denote vertical displacement.	101
5.3	Convergence of the hybrid optimization algorithm for aluminum silicate powder with $w = 5.5\%$ (left) and $w = 7.5\%$ (right) water content.	102
5.6	Experimental set-up used in the uniaxial compaction test of I14730 aluminum silicate powder, performed by Bosi et al. [1]. Cross section (left) and photograph (centre) of the forming device. The elements considered in the simulation: matrix, upper and lower punches, and ceramic powder (right).	108

5.8 Axisymmetric numerical simulation of tablet forming. Stress distribution (lateral stress σ_{xx} and axial stress σ_{yy}) in the ceramic powder and in the mould (composed by matrix, upper and lower punches) at the end of the main stages of powder compaction: geostatic step (upper part), axial loading (central part), axial unloading (lower part, left) and extraction of the tablet (lower part, right). 110

5.9 Three-dimensional numerical simulation of industrial tile forming. Stress distribution (lateral stress σ_{yy} and axial stress σ_{zz}) in the ceramic powder and in the mould (composed by matrix, upper and lower plates) at the end of the main stages of powder compaction: geostatic step (upper part), axial loading (central part), axial unloading (lower part, left) and extraction of the tile (lower part, right). 113

5.10 Description of the performed experimental test: the pressure-sensitive film is placed between the ceramic powder and the steel matrix. 114

5.11 Contact pressure values in the three-dimensional simulation (upper part) and imprint left on the pressure-sensitive film after the experimental test (lower part). 115

5.12 Void ratio distribution in a combed finish tile after die pressing. 116

6.1 Temperature-dependent hardening rules for the proposed thermoplastic constitutive model. The limit value of isotropic strength $p_{c_{max}}$ evolve according expression (6.7), where A^{p_c} is replaced by the ultimate isotropic strength at room temperature $p_{c_{max}0}$ 119

6.2 Influence of C_s , D_s and $p_{c_{Asint}}$ on p_c during softening: C_s regulates the curvature in the transition to the asymptotic value $p_{c_{Asint}}$ while D_s determines if hardening is immediately stopped once $p_{c_{max}}$ is reached. 122

6.3 Two-dimensional representation of the proposed strain limiter criterion (continuous line) and Rankine criterion (dashed line). 126

6.4 Uniaxial compression test at high temperature: the sample is heated through electromagnetic induction. 130

6.5 Evolution of the BP yield surface depending on temperature: the yield surface at room temperature is identified with a series of experimental tests, while only two (uniaxial compression and Brazilian tests) are performed at high temperature. . 131

6.6	Identified value of p_c depending on temperature. This case represents an exception for the considered refractory materials. When increasing the temperature, the material initially becomes more resistant. After reaching 400°C the yield strength of the material starts to decrease. The proposed expression (6.7) is in this case unable to follow properly the identified values of p_c , at least in the first part.	132
6.7	BP yield function at the onset of plasticity F_0 and ultimate yield function F_{ult} defining the beginning of softening behavior.	132
6.8	Numerical stress-strain curves at different temperatures for uniaxial compressive tests with the identified parameters: the dots represent the maximum stresses σ_{max} measured during the experimental tests.	134
6.9	Evolution of the isotropic strength p_c in the simulation of uniaxial compressive tests with the identified parameters: the dots represent the values of $p_{c_{max}}$ identified from the experimental tests according to the procedure described in Sec. 6.4.2.	135
6.10	Cracked sample used in an uniaxial compression test and strain gages for the measurement of the transversal strains. .	136
6.11	Stress strain curves and associated transversal/longitudinal strain in uniaxial compression test. The angles refer to the position of the strain gages around the specimen.	137
6.12	Experimental set-up of the bending tests and longitudinal section of the steel flow stopper with the applied boundary conditions.	138
6.13	Electromagnetically induced heat in the middle part of the refractory steel flow stopper.	139
6.14	Plastic strain distribution in the middle part of the refractory device.	140
6.15	From left to right: temperature T , isotropic compressive yield stress p_c , Von Mises stress q and displacement in x direction u_x at the end of the numerical analysis.	140
6.16	Comparison of experimental and numerical values of break load in the bending test of the refractory steel flow stopper. .	141
6.18	Numerical model of the slide gate composed of steel and refractory material.	142
6.19	Plate and nozzle, composed of different refractory materials. .	143
6.20	Interaction surfaces in the thermo-mechanical simulation. Different convection coefficients are taken into account for molten steel and air.	144
6.21	Temperature distribution in Slide gate at the beginning of the casting process.	145

6.22	Plastic deformation in the refractory plate during the casting process: the results show higher values of inelastic deformation in the external part of the plate, where crack development is typically observed in the real device.	145
6.23	Crack development during an experimental test on the refractory plate. The temperature of the material inside the hole is increased, in order to simulate the liquid steel flow.	146
6.24	Temperature distribution in refractory plate at the beginning (left) and at the end (right) of the casting process.	146
6.25	Schematic of continuous tundish casting, SEN and mold in a steel industry.	147
6.26	Modelization of the refractory VISO - tube.	147
6.27	Assigned symmetric boundary conditions for the thermo-mechanical simulation of the pouring tube.	148
6.28	Applied pressure of 4.2 MPa (1300 Kg) on the highlighted surface, in order to simulate the blocking mechanism of the nozzle.	149
6.29	Left and center: surfaces directly in contact with the molten metal. Right: surfaces subject to air convection.	149
6.30	Prediction of crack formation on the top part of the Sub-Entry Nozzle under working conditions, when p_c meets $p_{c_{max}}$	150
6.31	Temperature distribution in refractory VISO - tube at different time steps of the casting process. Respectively after one second, one minute and one hour.	151
6.32	Von Mises stress in refractory VISO - tube at different time steps of the casting process. Respectively after one second, one minute and one hour.	151
7.1	Example of evolution of the meridian shape of the BP yield function during a simulation. The calibration of the yield function shape of the loose powder (first yielding) $F(\sigma, p_{c0})$ and of the formed green body $F(\sigma, p_{c_{max}})$, should be based on multiple experimental tests. The meridian shape of the yield function is influenced by M , m and α	155
7.2	Example of evolution of the deviatoric shape of the BP yield function during a simulation. The BP yield function parameters that influence the deviatoric shape are β and γ	156
7.3	Plastic potential function $G(\sigma)$ for constant Δ_p and BP yield function $F(\sigma)$ in the $p - q$ plane. The plastic flow direction is shown for three arbitrary loading paths.	158
7.4	Dependence of parameter η (Eq. (7.18)) on the relative density.	160

7.5	Experimental values of the elastic modulus and proposed relationship for $E(T)$ (see Eq. (7.6)) with the identified material parameters.	164
7.6	BP yield criterion at the considered temperatures $T = \{25, 190, 250, 500\} \text{ }^\circ\text{C}$: the yield function shrinks homothetically according to the governing parameter p_c (see (7.19)).	165
7.7	Dependence of hardening parameter p_c and identified parameters for relationship (7.19).	166
7.8	Dependence of hardening parameter $k_1(T)$ on the temperature and identified parameters appearing in expression (7.15).	167
7.9	Dependence of hardening parameter $\delta(T)$ on the temperature and identified parameters appearing in Eq. (7.16).	168

List of Tables

3.1	Deformation steps $\Delta\varepsilon$ used for comparing the performance of the centre-of-mass integration algorithm with the return mapping, the latter performed on the squared version of the BP yield function.	43
3.2	Stress and plastic strain at the end of the finite step calculated with different algorithms for the strain and stress paths 1-6 of Table 3.1, graphically represented in Fig. 3.8.	45
3.3	Stress at the end of the finite step calculated with different algorithms for the strain and stress path 7 of Table 3.1, graphically represented in Fig. 3.8.	45
3.4	Plastic strain at the end of the finite step calculated with different algorithms for the strain and stress path 7 of Table 3.1, graphically represented in Fig. 3.8.	46
5.1	Material parameters for the compaction of aluminum silicate I14730, for two different water contents, $w = 5.5\%$ and $w = 7.5\%$. Seven parameters were obtained directly from the experiments by Bosi et al. [1], the other 15 parameters have been identified by multi-objective optimization.	103
5.2	Dimensions and densities of I14730 aluminum silicate tablets ($w=5.5\%$) after completion of the uniaxial compaction process and extraction from the cylindrical mould.	111
5.3	Dimensions and densities of I14730 aluminum silicate tablets ($w=7.5\%$) after completion of the uniaxial compaction process and extraction from the cylindrical mould.	111
6.1	Values of stress σ , strain ε and isotropic strength p_c in numerical simulations and experimental tests at the considered temperatures.	136
7.1	Values of the elastic modulus in the experimental tests of Gupta et al. [2].	163

- 7.2 Yield stresses in tension σ_{yt} and compression σ_{yc} and identified compressive isotropic strength p_c at the considered temperatures for the experimental tests of Gupta et al. [2]. 165
- 7.3 Values of the parameters k_1 and δ at the considered temperatures identified through inverse analysis. 167
- 7.4 Material parameters for cold forming and pre-sintering of alumina. 170

Abstract

Three constitutive models for the mechanical description of the behavior of ceramic materials are developed, implemented into a numerical code, calibrated on experimental data, and validated.

- The first model is elastic-plastic and addresses the cold compaction of ceramic powders, combining nonlinear elasticity, elastoplastic coupling and increase of cohesion.
- The second model is thermal-viscous-elastic-plastic and is specifically tailored to describe the thermo-mechanical behavior of refractory devices under working conditions at high-temperature.
- The third model is thermal-elastic-plastic and implements a shape evolution of the BP yield function, calibrated to simulate the forming of green bodies and their pre-sintering phase.

Three algorithms are developed for the integration of constitutive equations when pathological yield functions are involved. The algorithms are coded in user material subroutines to be used in commercial FE softwares and their accuracy is evaluated in model problems allowing for semi-analytical solutions.

Material constitutive parameters are obtained from a combination of experimental tests and multi-objective optimization and employed in FE simulations of industrial processes, such as cold-forming of combed finish ceramic tiles and metal flow confinement by means of refractory devices.

This PhD thesis is the outcome of the secondment period at the Vesuvius Group, within the framework of the IAPP European project HOTBRICKS (contract number PIAPP-GA-2013-609758).

Chapter 1

Introduction

Ceramic materials are essential in a wide range of engineering applications, such as aerospace, automotive, thermal protection, braking systems, and electronics. Their industrial employment is related to their excellent mechanical strength, high thermal shock resistance and formidable phase stability in a broad range of pressure and temperature.

A negative aspect of the production of ceramic devices is that it represents one of the most polluting industrial processes, particularly from the point of view of the energy waste and related greenhouse gas emission.

The design of refractory materials to be used in the liquid steel technology faces several problems, particularly related to the safety and reliability of the pieces.

The modeling and optimization of such processes is an extremely complex and challenging goal, especially for the variety of the observed nonlinear effects, caused by significant changes in the material micro-structure due to inelastic deformations and thermal effects.

Constitutive models for ceramic materials are invaluable tools in the design of forming of ceramic pieces from powder and in the design of refractories to be employed at high temperature. However, reliable constitutive models, providing a realistic descriptions of thermo-elasto-plastic behavior of ceramics are still not available.

The development of constitutive models for ceramics, for describing both powder densification and the high-temperature mechanical response of refractories, their numerical implementation and their calibration and validation on experiments is the aim of the present PhD thesis. Specifically, three different constitutive

models are developed, implemented in external subroutines to be used in FE codes and validated through comparison with experimental tests in particular conditions, including high-temperature.

A mathematical description of the theory of rate-independent and rate-dependent thermo-plasticity is given in Chapter 2, starting from simple perfectly-plastic and isotropic hardening models, elucidating the most important thermo-mechanical couplings and finally introducing the ‘stretchable’ Bigoni-Piccolroaz [3–5] yield function. Figure 1.1 shows schematically the concept of *overstress* (the stress state lies *outside* the yield surface) allowing for rate-dependence of the elasto-plastic constitutive equations.

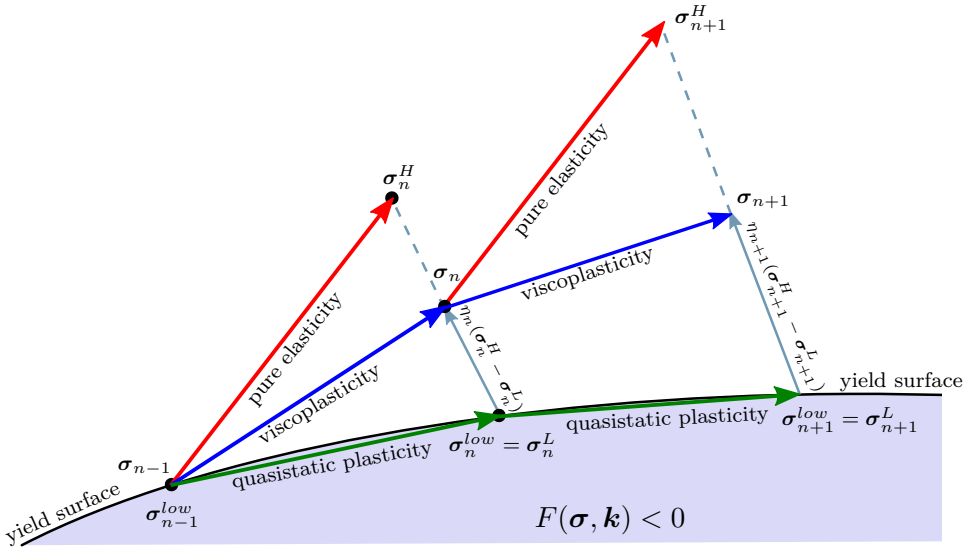


Figure 1.1: Conceptual illustration of rate-dependent plasticity. For a given strain increment, the viscoplastic solution is found between two limiting stress states: the ‘high rate’ solution σ^H which is the simple trial elastic stress and the ‘low rate solution’ σ^L corresponding to the quasistatic plastic solution.

Chapter 3 is devoted to the illustration of the developed numerical strategies for the efficient solution of the *central problem of computational plasticity*, namely the integration of the local constitutive equations. Three innovative algorithms for the integration of non-standard constitutive models are introduced and applied to the Bigoni-Piccoroaz criterion:

- (i) An explicit integration scheme based on a forward Euler technique with a return correction directed towards the ‘centre-of-mass’ of the yield surface;

- (ii) An implicit integration scheme based on a ‘cutoff-substepping’ return algorithm, especially designed to avoid so-called ‘false-elastic domains’ (definition introduced by Brannon and Leela-
vanichkul [6]);
- (iii) A return mapping procedure combined with the implicit definition of the considered yield function [7]. Figure 1.2 shows a convex and smooth BP yield surface (left part) and the iso-surfaces of the corresponding implicit yield function (right part) in the principal stress space.

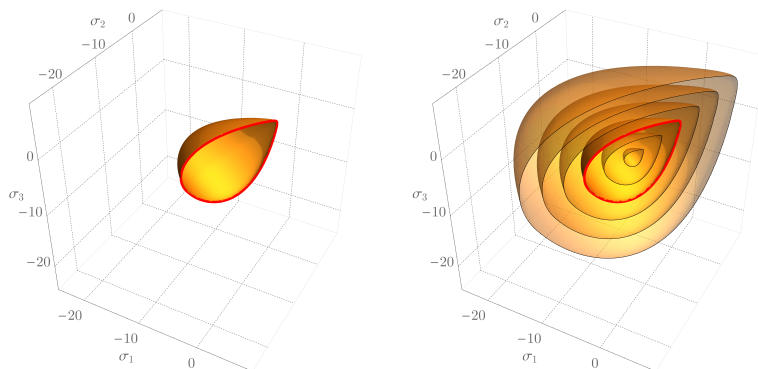


Figure 1.2: A convex and smooth BP yield surface (left). Iso-surfaces of the corresponding implicit BP yield function in the principal stress space (right). The zero-level surface is marked in red color.

The computational performance of each of the developed algorithms and the correctness of the results are investigated through particular tests and comparisons with the semi-analytical solutions of selected mechanical and thermo-mechanical problems.

The calibration of the constitutive models on experimental data is a difficult task, because the response of the material model depends strongly on several constants appearing in the constitutive equations. An overview of the most effective numerical strategies for efficient parameter identification is given in Chapter 4, with emphasis on the algorithms employed in the present work. Figure 1.3 shows the convergence of the hybrid optimization algorithm for aluminum silicate powder with $w = 5.5\%$ (left) and $w = 7.5\%$ (right) water content.

Chapters 5, 6 and 7 present the newly developed constitutive models for ceramic materials.

More specifically, Chapter 5 introduces a non-associative elastoplastic model designed for the simulation of the cold forming pro-

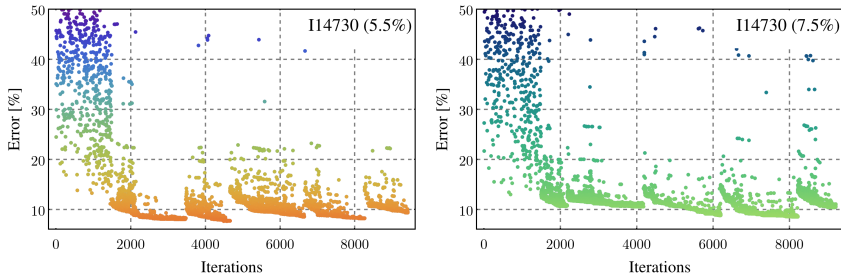


Figure 1.3: Convergence of the hybrid optimization algorithm for aluminum silicate powder with $w = 5.5\%$ (left) and $w = 7.5\%$ (right) water content.

cess of ceramic powders. Its formulation combines nonlinear elasticity and elasto-plastic coupling with specific hardening laws governing the increase of cohesion. The model is validated through comparison of the experimental results obtained from uniaxial deformation tests and triaxial test on aluminum silicate samples. A series of simulations of particular industrial processes for the forming of tiles is carried out, employing material parameters identified through a multi-objective optimization.

In Chapter 6 a rate-dependent thermo-plastic model for refractories is proposed. The development of this model is related to the collaboration with the Vesuvius Group, as part of the IAPP HOTBRICKS European project. In particular, the model aims to describe the behavior of refractory devices under working conditions, thus at extremely high-temperature. This Chapter illustrates the thermo-mechanical couplings and the material failure criteria included in the model together with a parameter identification procedure of general validity. Simulation of complex heat resistant devices employed in the foundry industries are discussed at the end of the Chapter. Figure 1.4 shows plastic strains in a refractory plate during the casting process. The results show higher values of inelastic deformations in the external part of the plate, where crack development is typically observed in the real device. This simulation confirms the validity of the constitutive model in predicting damage evolution in heat resistant components.

Finally, Chapter 7 is devoted to the unified thermo-mechanical modelling of forming and subsequent pre-sintering of ceramics. Pre-sintering is the initial phase of the sintering process, in which the green body undergoes numerous endothermic and exothermic processes, including dehydration, organic removal, decomposition, phase formation in the case of reactive systems. Accurate mod-

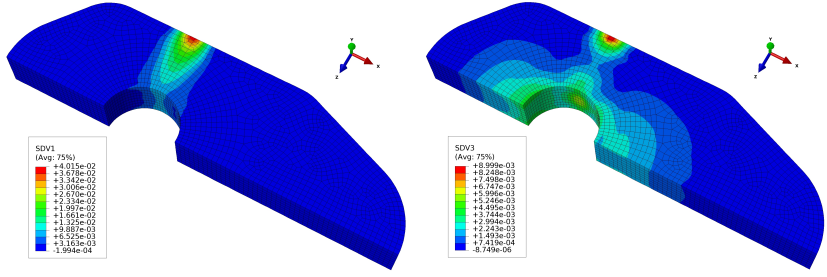


Figure 1.4: Plastic deformation in a refractory plate during the casting process: the results show higher values of inelastic deformation in the external part of the plate, where crack development is typically observed in the real device.

eling and simulation of the presintering stage of firing is of great interest, given the importance of avoiding defects before the final stage of densification is reached [2]. In the proposed model, the ‘shape evolution’ of the BP yield surface, see Fig. 1.5, is introduced and applied for the first time to powder densification processes. Thermal effects at pre-sintering temperatures are studied in detail, comparing numerical and experimental results of tests on alumina green bodies. A specific plastic potential function is employed for efficient regulation of the plastic flow direction and combination of density-dependent hardening laws.

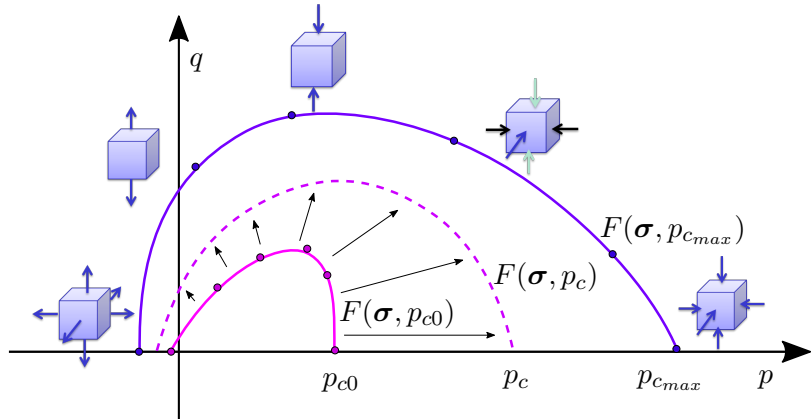


Figure 1.5: Example of evolution of the meridian shape of the BP yield function during a simulation. The calibration of the yield function shape of the loose powder (first yielding) $F(\sigma, p_{c0})$ and of the formed green body $F(\sigma, p_{c_{max}})$, should be based on multiple experimental tests. The meridian shape of the yield function is influenced by M , m and α .

Chapter 2

Theory of rate-dependent thermoplasticity

Nonlinearities are evident in the response of almost all known materials, when these are subject to extreme actions, leading to inelastic deformations. These effects are further amplified in high-temperature applications, where mechanical and thermal properties of materials are often coupled. Taking into account the effects of the strain rate on the material response introduces an additional degree of complexity into the mathematical description of the observed material behaviors.

In this Chapter, the main assumptions of the so-called theory of thermoplasticity are presented, and both the quasi-static and rate-dependent constitutive equations are derived. Finally, the Bigoni-Piccolroaz yield function [3–5] is introduced and its capability in describing a wide range of materials is described.

2.1 Plasticity

Taking into account the nonlinear effects of inelastic deformations is crucial for the correct representation of the behavior of a wide range of materials. Usually, nonlinear effects appear after a certain stress state, the so-called yield stress, is reached. Depending on the nature of the considered material, the causes of such inelastic behavior are caused by dislocations (typically in metals), micro-cracking (rock-like, concrete-like materials) or changes in the material micro-structure (e.g. increase/reduction of the void ratio).

In solid mechanics, a description of such behaviors is made possible by the so-called *theory of plasticity*, which is described in

the following, starting from its most simple forms.

2.1.1 Unidimensional perfect plasticity

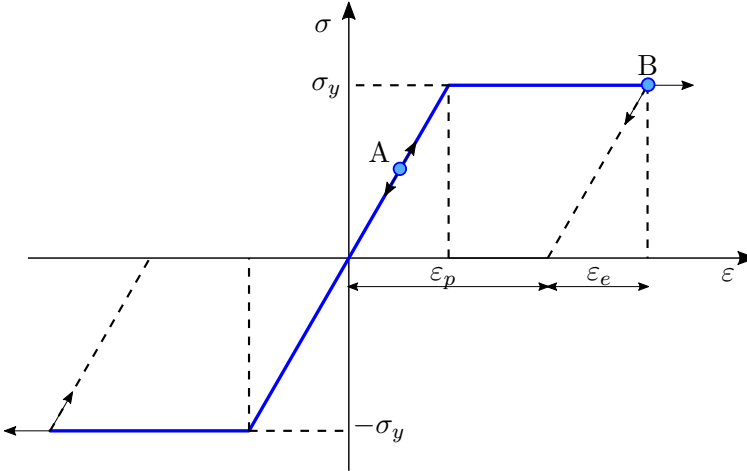


Figure 2.1: Perfectly plastic uniaxial constitutive model.

We consider a material with a perfectly plastic behavior as represented in Fig.2.1. The features of such constitutive model can be resumed as follows:

- Existence of a purely elastic domain $\sigma \in (-\sigma_y, \sigma_y)$ where no inelastic deformation occurs; σ_y is the so-called yield stress.
- Additive strain decomposition: $\varepsilon = \varepsilon_e + \varepsilon_p$.
- If $-\sigma_y < \sigma < \sigma_y$ (e.g. at point A), then the stress state is purely elastic, and the relationship $\sigma = E\varepsilon$ is valid.
- If $\sigma = \sigma_y$, (e.g. at point B) then inelastic deformation occurs. From this point it is possible to follow the plastic load path (horizontal line) where the stress increment $\dot{\sigma} = 0$ generates plastic deformation $\dot{\varepsilon}_p \neq 0$, or the elastic unload path (descending line) reentering the elastic domain and $\dot{\sigma} = E\dot{\varepsilon}$, $\dot{\varepsilon}_p = 0$.

It is therefore necessary to adopt an incremental approach to solve the problem, since both stress and strain states depend on the load history. To better describe the behavior of ductile materials is however necessary to introduce a more general formulation, which takes hardening into account.

2.1.2 Plasticity with hardening

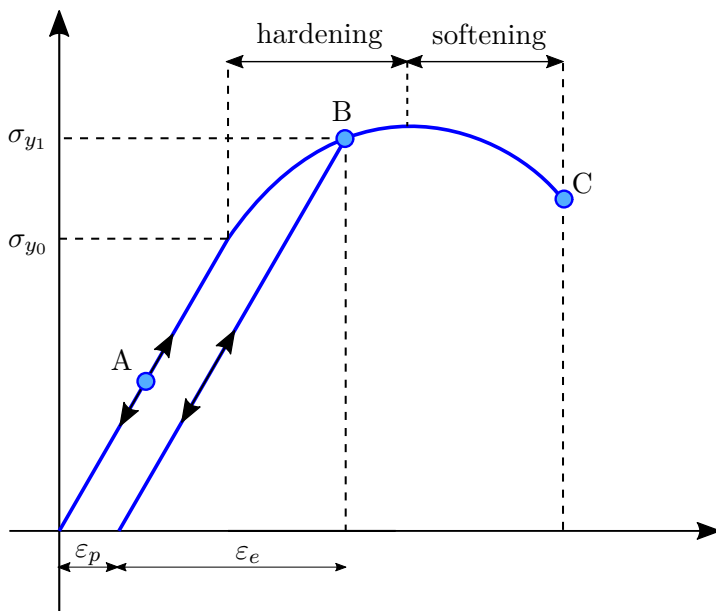


Figure 2.2: Hardening behavior for metallic materials.

We consider a material characterized by hardening behavior, which can be qualitatively illustrated as in Fig.2.2. The properties described in the previous section are valid also for materials showing hardening behavior.

However, as shown in Fig.2.2, the stress σ_y after the yield point is in this case not constant. A nonlinear response is observed after the ‘virgin’ material is loaded over the initial yield stress σ_{y0} up to point B. The occurred plastic deformation ε_p increases the yield stress, so that in case of unloading and subsequent reloading, the new yield stress is $\sigma_{y1} > \sigma_{y0}$.

A complete description of the behavior of a material showing inelastic deformations requires the three-dimensional generalization of the cited observations by means of incremental equations and also requires the definition of ‘yield function’.

A yield function F is a concept introduced to discriminate between purely elastic and elastoplastic states. The present description of the theory of plasticity is based on the stress-space formulation of a general yield function, in which the material state is

defined by the stress $\boldsymbol{\sigma}$ and a vector \mathbf{k} of so-called internal variables, which define the occurred inelastic deformation.

Therefore, a yield function is a scalar-valued tensor function depending on the tensor $\boldsymbol{\sigma}$ and a given set of state variables \mathbf{k} . Negative and null values of a general yield function are respectively associated to elastic states and states for which plastic flow becomes possible, namely,

- If $F(\boldsymbol{\sigma}, \mathbf{k}) < 0$ then the response of the material is purely elastic,
- If $F(\boldsymbol{\sigma}, \mathbf{k}) = 0$ then plastic flow is possible.

The yield surface is the level set $F(\boldsymbol{\sigma}, \mathbf{k}) = 0$ in the hyper-space of the variables $\boldsymbol{\sigma}$ and \mathbf{k} .

If we assume that the elastic tensor \mathbb{E} remains constant ($\dot{\mathbb{E}} = 0$), the stress increment becomes

$$\dot{\boldsymbol{\sigma}} = \dot{\mathbb{E}}\boldsymbol{\varepsilon} + \mathbb{E}\dot{\boldsymbol{\varepsilon}} = \mathbb{E}\dot{\boldsymbol{\varepsilon}}. \quad (2.1)$$

The additive strain decomposition can be written in incremental form as

$$\dot{\boldsymbol{\varepsilon}} = \dot{\boldsymbol{\varepsilon}}_e + \dot{\boldsymbol{\varepsilon}}_p. \quad (2.2)$$

The so called flow rule is introduced to define the increment of plastic strain $\dot{\boldsymbol{\varepsilon}}_p$:

$$\dot{\boldsymbol{\varepsilon}}_p = \dot{\lambda} \mathbf{P}, \quad (2.3)$$

in which $\dot{\lambda}$ is a positive or zero valued scalar, defined as ‘plastic multiplier’. ($\dot{\lambda} = 0$ indicates null plastic flow, while $\dot{\lambda} > 0$ indicates active plastic flow), and \mathbf{P} is a symmetric tensor that can be expressed as

$$\mathbf{P} = \frac{\partial G(\boldsymbol{\sigma})}{\partial \boldsymbol{\sigma}}, \quad (2.4)$$

in which G is the so-called *plastic potential function*.

In case of associative plasticity, \mathbf{P} is taken equal to the gradient of the yield function.

$$\mathbf{P} = \mathbf{Q} = \frac{\partial F(\boldsymbol{\sigma}, \mathbf{k})}{\partial \boldsymbol{\sigma}}, \quad (2.5)$$

so that the plastic flow direction is normal to the yield surface in all its points.

In case of non-associative plasticity, plastic flow directions different from the normal to the yield surface can be defined. This is achieved by introducing a potential function different from the considered yield function. This is particularly important in case of frictional and pressure-sensitive materials, such as soils, ceramic or metallic powders, where associated plasticity often give unrealistic high values of plastic dilatancy.

A non-associative constitutive model is usually computationally more expensive than the corresponding associative model, since the constitutive tangent operator, which will be introduced later, becomes asymmetric. As a consequence, the computation of the global tangent matrix in the context of Finite Element Analysis and the solution of the associated linear system require a larger number of operations.

In the considered three-dimensional case of plasticity with hardening, the increase in yield strength is obtained by increasing or modifying the size and possibly the shape (see Sec. 7.1.1) of the yield surface. Therefore, assuming a stress value on the surface, an increment of deformation can yield to the three different cases presented in Fig. 2.3:

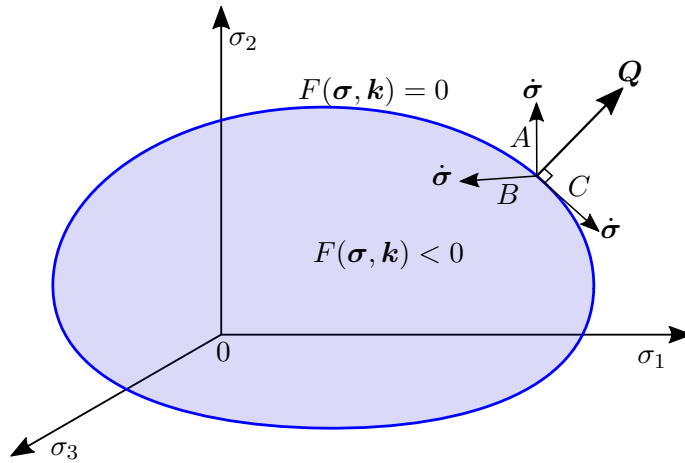


Figure 2.3: Example of yield surface and possible deformation increments.

- **Plastic loading** (case A): The strain increment $\dot{\sigma}$ is directed externally to the yield surface and ‘drags’ it with itself:
 $\dot{\sigma} \cdot Q \geq 0 \Leftrightarrow \dot{\lambda} > 0$;

- **Elastic unloading** (case B): The strain increment $\dot{\boldsymbol{\sigma}}$ is directed internally to the yield surface and the yield function remains unchanged:
 $\dot{\boldsymbol{\sigma}} \cdot \mathbf{Q} < 0 \Leftrightarrow \dot{\lambda} = 0$;
- **Neutral loading** (case C): The strain increment $\dot{\boldsymbol{\sigma}}$ is directed tangentially to the yield surface:
 $\dot{\boldsymbol{\sigma}} \cdot \mathbf{Q} = 0 \Leftrightarrow \dot{\lambda} = 0$.

During an inelastic deformation process, the actual stress vector $\boldsymbol{\sigma}$ moves ‘carrying’ the yield function with itself and remaining on it. In other words, for each instant of time $F(\boldsymbol{\sigma}, \mathbf{k}) = 0$ and consequently $\dot{F}(\boldsymbol{\sigma}, \mathbf{k}) = 0$.

This condition is the so-called *Prager consistency condition*, according to which any stress state outside the yield surface is considered unfeasible, at least in case of rate-independent plasticity. Otherwise, rate-dependent plasticity (see Sec. 2.3) allows stress states outside the yield surface.

2.1.3 Incremental constitutive equations

Considering the case of plastic loading (case A of Fig. 2.3), we can apply the chain rule to the Prager consistency condition to obtain

$$\dot{F}(\boldsymbol{\sigma}, \mathbf{k}) = \frac{\partial F}{\partial \boldsymbol{\sigma}} \cdot \dot{\boldsymbol{\sigma}} + \frac{\partial F}{\partial \mathbf{k}} \cdot \dot{\mathbf{k}} = 0. \quad (2.6)$$

From equation (2.5), we can define the hardening modulus $H(\boldsymbol{\sigma}, \mathbf{k})$ as

$$\frac{\partial F}{\partial \mathbf{k}} \cdot \dot{\mathbf{k}} = -\dot{\lambda} H(\boldsymbol{\sigma}, \mathbf{k}), \quad (2.7)$$

and rewrite Eq. (2.6) as

$$\mathbf{Q} \cdot \dot{\boldsymbol{\sigma}} - \dot{\lambda} H = 0. \quad (2.8)$$

By substituting (2.2) and (2.3) in the constitutive equation, we obtain

$$\dot{\boldsymbol{\sigma}} = \mathbb{E} \dot{\boldsymbol{\varepsilon}}_e = \mathbb{E} \dot{\boldsymbol{\varepsilon}} - \dot{\lambda} \mathbb{E} \mathbf{P}. \quad (2.9)$$

Dot product with \mathbf{Q} yields

$$\mathbf{Q} \cdot \dot{\boldsymbol{\sigma}} = \mathbf{Q} \cdot \mathbb{E} \dot{\boldsymbol{\varepsilon}} - \dot{\lambda} \mathbf{Q} \cdot \mathbb{E} \mathbf{P}. \quad (2.10)$$

This expression, substituted in (2.8), gives

$$\mathbf{Q} \cdot \mathbb{E}\dot{\boldsymbol{\varepsilon}} - \dot{\lambda}(H + \mathbf{Q} \cdot \mathbb{E}\mathbf{P}) = 0, \quad (2.11)$$

from which we can obtain

$$\dot{\lambda} = \frac{\mathbf{Q} \cdot \mathbb{E}\dot{\boldsymbol{\varepsilon}}}{H + \mathbf{Q} \cdot \mathbb{E}\mathbf{P}}. \quad (2.12)$$

By substituting (2.12) in (2.8) we get

$$\dot{\boldsymbol{\sigma}} = \mathbb{E}\dot{\boldsymbol{\varepsilon}} - \frac{\mathbf{Q} \cdot \mathbb{E}\dot{\boldsymbol{\varepsilon}}}{H + \mathbf{Q} \cdot \mathbb{E}\mathbf{P}}\mathbb{E}\mathbf{P}, \quad (2.13)$$

or

$$\dot{\boldsymbol{\sigma}} = \mathbb{C}\dot{\boldsymbol{\varepsilon}}, \quad (2.14)$$

with \mathbb{C} being a fourth order tensor named ‘elastoplastic tensor’ or ‘constitutive tangent operator’.

In case of non-associative plastic flow, the main equations for hardening plasticity can be summarized as:

$$\dot{\boldsymbol{\sigma}} = \begin{cases} \mathbb{E}\dot{\boldsymbol{\varepsilon}} - \frac{\mathbf{Q} \cdot \mathbb{E}\dot{\boldsymbol{\varepsilon}}}{H + \mathbf{Q} \cdot \mathbb{E}\mathbf{P}}\mathbb{E}\mathbf{P}, & \text{if } F(\boldsymbol{\sigma}, \mathbf{k}) = 0 \text{ and } \mathbf{Q} \cdot \mathbb{E}\dot{\boldsymbol{\varepsilon}} > 0, \\ \mathbb{E}\dot{\boldsymbol{\varepsilon}}, & \text{if } F(\boldsymbol{\sigma}, \mathbf{k}) = 0 \text{ and } \mathbf{Q} \cdot \mathbb{E}\dot{\boldsymbol{\varepsilon}} \leq 0, \\ \mathbb{E}\dot{\boldsymbol{\varepsilon}}, & \text{if } F(\boldsymbol{\sigma}, \mathbf{k}) < 0. \end{cases} \quad (2.15)$$

We can rewrite the last constitutive equations in a more compact way by introducing the *Macaulay bracket* operator $\langle x \rangle$, which return the value 0 if $x \leq 0$ or x if $x > 0$.

Equation (2.15) becomes therefore

$$\dot{\boldsymbol{\sigma}} = \begin{cases} \mathbb{E}\dot{\boldsymbol{\varepsilon}} - \frac{\langle \mathbf{Q} \cdot \mathbb{E}\dot{\boldsymbol{\varepsilon}} \rangle}{H + \mathbf{Q} \cdot \mathbb{E}\mathbf{P}}\mathbb{E}\mathbf{P}, & \text{if } F(\boldsymbol{\sigma}, \mathbf{k}) = 0, \\ \mathbb{E}\dot{\boldsymbol{\varepsilon}}, & \text{if } F(\boldsymbol{\sigma}, \mathbf{k}) < 0. \end{cases} \quad (2.16)$$

To obtain the inverse expression it is sufficient to write Eq. (2.2) in explicit form

$$\dot{\boldsymbol{\varepsilon}} = \dot{\boldsymbol{\varepsilon}}_e + \dot{\boldsymbol{\varepsilon}}_p = \mathbb{E}^{-1}\dot{\boldsymbol{\sigma}} + \dot{\lambda}\mathbf{P}, \quad (2.17)$$

so that we obtain

$$\dot{\boldsymbol{\varepsilon}} = \mathbb{E}^{-1}\dot{\boldsymbol{\sigma}} + \frac{\mathbf{Q} \cdot \dot{\boldsymbol{\sigma}}}{H}\mathbf{P}. \quad (2.18)$$

2.2 Thermo-plasticity

Temperature can induce important mechanical effects, such as strength reduction, lower stiffness or thermal deformation. Similarly, thermal effect as a consequence of mechanical loading are also possible, so that the differential equations describing both elastic and inelastic material behavior can usually not be considered separately.

The formulation of two constitutive models proposed in this work is based on the theory of thermo-plasticity. In the following the main assumptions of this theory are described.

2.2.1 Thermo-mechanical coupling

Taken separately, the equilibrium equation (in absence of body forces), the heat conduction equation and (isotropic) Fourier law can be respectively written as

$$\operatorname{div} \boldsymbol{\sigma} = 0, \quad \boldsymbol{\sigma} = \boldsymbol{\sigma}(\boldsymbol{\varepsilon}), \quad (2.19)$$

and

$$\begin{aligned} c\rho\dot{T} + \operatorname{div} \mathbf{q} - Q &= 0, \\ \mathbf{q} &= -k\nabla T, \end{aligned} \quad (2.20)$$

where c is the specific heat capacity, ρ is the mass density, k is the thermal conductivity and Q is the volumetric heat flux.

In the analysis of simultaneous thermal and mechanical loads, the material response must consider the couplings between the equilibrium equation and the heat conduction equation.

In particular, the following thermo-mechanical coupling equations are taken into account:

- **Thermal expansion:** the temperature increase generates thermal deformation according to the following equation

$$\boldsymbol{\varepsilon}_T = \alpha(T - T_0)\mathbf{I}, \quad (2.21)$$

where α and T_0 are the thermal expansion coefficient and the reference temperature, respectively.

- **Thermal plastic softening:** in a wide range of materials (e.g. metals, concrete), high temperature induces a reduction

of the yield strength. For a simple unidimensional constitutive model with linear hardening, the yield strength can be therefore expressed as

$$\sigma_y(\varepsilon_p, T) = \sigma_y^0 + h\varepsilon_p - \omega T, \quad (2.22)$$

where ω and h are respectively the thermal softening coefficient and the strain hardening coefficient. In more general three-dimensional constitutive models, the same effect can be achieved by imposing a relationship between the parameters regulating the size of the yield surface and the temperature (see Sec. 7.1.5). Positive temperature increment can reduce the size of the yield function and consequently the yield strength of the material.

- **Piezocaloric effect:** usually materials generate heat if subjected to volumetric elastic strain according to the expression

$$H = 3K\alpha T_0 \operatorname{tr}(\dot{\boldsymbol{\varepsilon}} - \dot{\boldsymbol{\varepsilon}}_p) = 3K\alpha T_0 \operatorname{tr} \dot{\boldsymbol{\varepsilon}}, \quad \text{for } \operatorname{tr} \dot{\boldsymbol{\varepsilon}}_p = 0, \quad (2.23)$$

where K is the elastic bulk modulus. In some cases (high external temperature loads or small volumetric strain) this effect can be neglected due to its very small influence. Nevertheless ‘fully coupled’ finite elements have been implemented and compared to analytical solutions during the development of the present work.

- **Plastic heating:** plastic deformation generates heat in the material according to the following equation

$$D_{mech} = \chi \boldsymbol{\sigma} \cdot \dot{\boldsymbol{\varepsilon}}_p, \quad 0 \leq \chi \leq 1, \quad (2.24)$$

where χ is the so-called Taylor-Quinney coefficient.

Under consideration of the thermomechanical couplings, the equilibrium equation (2.19) becomes

$$\operatorname{div} \boldsymbol{\sigma} = 0, \quad \boldsymbol{\sigma} = \boldsymbol{\sigma}(\boldsymbol{\varepsilon}, T), \quad (2.25)$$

and the heat conduction equation (2.20)

$$c\rho\dot{T} + H + \operatorname{div} \mathbf{q} - D_{mech} - Q = 0, \quad (2.26)$$

$$\mathbf{q} = -k\nabla T.$$

Equations (2.25) and (2.26) represent the strong (differential) form of the thermomechanical problem. The use of these formulations for numerical analysis (finite element method) requires their derivation in weak (integral) form through integration per parts and application of the Gauss theorem.

2.2.2 Incremental constitutive equations

As similarly done in Sec. 2.1.3 for isothermal plasticity, the incremental constitutive equations are now introduced while taking into account the thermal effects.

The decomposition of the strain into the elastic (ε_e), plastic (ε_p) and thermal (ε_T) parts,

$$\varepsilon = \varepsilon_e + \varepsilon_p + \varepsilon_T, \quad (2.27)$$

allows us to obtain the incremental elastic strain in the form

$$\dot{\varepsilon}_e = \dot{\varepsilon} - \dot{\varepsilon}_p - \dot{\varepsilon}_T. \quad (2.28)$$

Thermal strain is assumed as an isotropic function of the temperature $T = T_R - T_0$, where T_R is the actual temperature and T_0 is the reference temperature.

Thermal strain is proportional to the coefficient of thermal expansion α_T

$$\varepsilon_T = \alpha_T T \mathbf{I}, \quad (2.29)$$

so we can write it in incremental form as

$$\dot{\varepsilon}_T = \alpha_T \dot{T} \mathbf{I}. \quad (2.30)$$

The ‘accumulated plastic strain’ $P(\varepsilon_p)$ is defined as

$$P(\varepsilon_p) = \int_0^t |\dot{\varepsilon}_p| d\tau. \quad (2.31)$$

By introducing the flow rule

$$\dot{\varepsilon}_p = \dot{\lambda} \mathbf{P}, \quad (2.32)$$

where \mathbf{P} is the gradient of the plastic potential, we obtain that the rate of the accumulated plastic strain is proportional to the plastic multiplier ($\dot{\lambda} \geq 0$) in the form

$$\dot{P}(\varepsilon) = \dot{\lambda} |\mathbf{P}|. \quad (2.33)$$

With a substitution of Eq.(2.28) and Eq.(2.32) into the incremental elastic constitutive equation $\dot{\boldsymbol{\sigma}} = \mathbb{E}\dot{\boldsymbol{\varepsilon}}_0^e + \mathbb{E}_0\dot{\boldsymbol{\varepsilon}}^e$, we obtain

$$\dot{\boldsymbol{\sigma}} = \mathbb{E}\dot{\boldsymbol{\varepsilon}}_0^e + \mathbb{E}_0(\dot{\boldsymbol{\varepsilon}} - \dot{\lambda}\mathbf{P} - \alpha_T\dot{T}\mathbf{I}). \quad (2.34)$$

Note that for simplicity we refer to isotropic elasticity, so that the elastic tensor \mathbb{E} is defined in terms of elastic modulus E and Poisson ratio ν . Moreover we introduce the dependence of the elastic tensor \mathbb{E} on the temperature.

During plastic loading, the stress point must satisfy the yield condition $F(\boldsymbol{\sigma}, \mathbf{k}) = 0$ at every time increment, therefore the Prager consistency can be written as

$$\dot{F} = \mathbf{Q} \cdot \dot{\boldsymbol{\sigma}} + \frac{\partial F}{\partial \mathbf{k}} \cdot \dot{\mathbf{k}} = 0, \quad (2.35)$$

where $\mathbf{Q} = \partial F / \partial \boldsymbol{\sigma}$ is the yield function gradient and \mathbf{k} is the hardening parameters vector. With the dependence of hardening parameters on the accumulated plastic strain and temperature $\mathbf{k}(T, P(\varepsilon_p))$, we can rewrite Eq. (2.35) as

$$\mathbf{Q} \cdot \dot{\boldsymbol{\sigma}} + \frac{\partial F}{\partial \mathbf{k}} \left(\frac{\partial \mathbf{k}}{\partial T} \dot{T} + \frac{\partial \mathbf{k}}{\partial \mathbf{P}} \dot{\mathbf{P}} \right) = 0. \quad (2.36)$$

Substitution of Eq. (2.34) and Eq.(2.33) into Eq.(2.36) allows us to obtain the plastic multiplier in the following form

$$\dot{\lambda} = \frac{\mathbf{Q} \cdot \left\{ \mathbb{E}\dot{\boldsymbol{\varepsilon}}_0^e + \mathbb{E}_0 \left[\dot{\boldsymbol{\varepsilon}} - \alpha_T\dot{T}\mathbf{I} \right] \right\} + \frac{\partial F}{\partial \mathbf{k}} \frac{\partial \mathbf{k}}{\partial T} \dot{T}}{\mathbf{Q} \cdot \mathbb{E}_0\mathbf{Q} - |\mathbf{P}| \frac{\partial F}{\partial \mathbf{k}} \frac{\partial \mathbf{k}}{\partial \mathbf{P}}}. \quad (2.37)$$

By using Eq. (2.37) into Eq. (2.34) yields the thermo-elasto-plastic constitutive equations in the rate form

$$\begin{aligned} \dot{\boldsymbol{\sigma}} = & \mathbb{E}\dot{\boldsymbol{\varepsilon}}_0^e + \mathbb{E}_0\dot{\boldsymbol{\varepsilon}} - \alpha_T\dot{T}\mathbb{E}_0\mathbf{I} + \\ & - \frac{\mathbf{Q} \cdot \left\{ \mathbb{E}\dot{\boldsymbol{\varepsilon}}_0^e + \mathbb{E}_0 \left[\dot{\boldsymbol{\varepsilon}} - \alpha_T\dot{T}\mathbf{I} \right] \right\} + \frac{\partial F}{\partial \mathbf{k}} \frac{\partial \mathbf{k}}{\partial T} \dot{T}}{\mathbf{Q} \cdot \mathbb{E}_0\mathbf{Q} - |\mathbf{P}| \frac{\partial F}{\partial \mathbf{k}} \frac{\partial \mathbf{k}}{\partial \mathbf{P}}} \mathbb{E}_0\mathbf{P}. \end{aligned} \quad (2.38)$$

2.3 Rate dependence

The equations discussed so far are only valid for rate independent problems. In other words, only apply for quasi-static loading.

In case of high strain rates, the elastic material response occurs almost instantaneously. Otherwise, the damage mechanisms responsible of the observed inelastic deformation *can not* take place instantaneously. Materials are characterized by a certain ‘internal resistance’ also called ‘viscosity’ which retards the damage development. In the following the fundamental assumptions and a general viscoplastic formulation is described in detail.

2.3.1 General concept: overstress and relaxation

Cracks in a material grow at finite speed, they cannot change their size instantaneously. In case of stress sufficiently high to cause cracks, the quasi-static solution will not be realized until a sufficiently long time to permit the full crack development has elapsed. In the limit of extraordinary high strain rates (as for example near the source of an explosion), the immediate material response is essentially elastic, since insufficient time exists for plasticity to develop.

To allow for rate dependence, an ‘overstress’ model is used. In presence of high strain-rates, the stress state will lie *outside* the yield surface until a sufficiently long time for the material to equilibrate has passed.

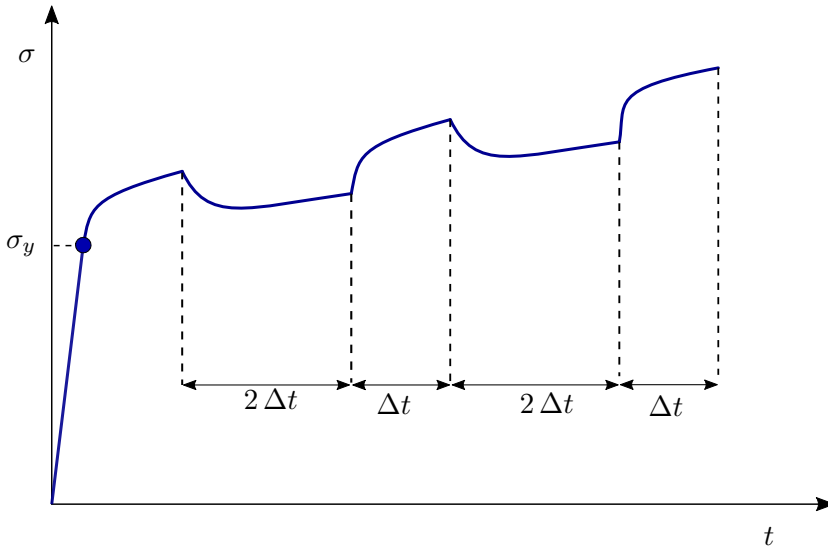


Figure 2.4: Stress ‘jumps’ induced by changes in the strain rate during loading.

Changes in the strain rate during the deformation process will therefore result in stress ‘jumps’, which are qualitatively illustrated

in Figure 2.4. Otherwise, when imposing a constant stress state resulting in material yielding we expect plastic deformation to grow over time (see Fig. 2.5), due to the ‘relaxation’ of the stress state that proceeds towards the quasi-static solution. This mechanism can efficiently simulate creep effects in a wide range of materials.

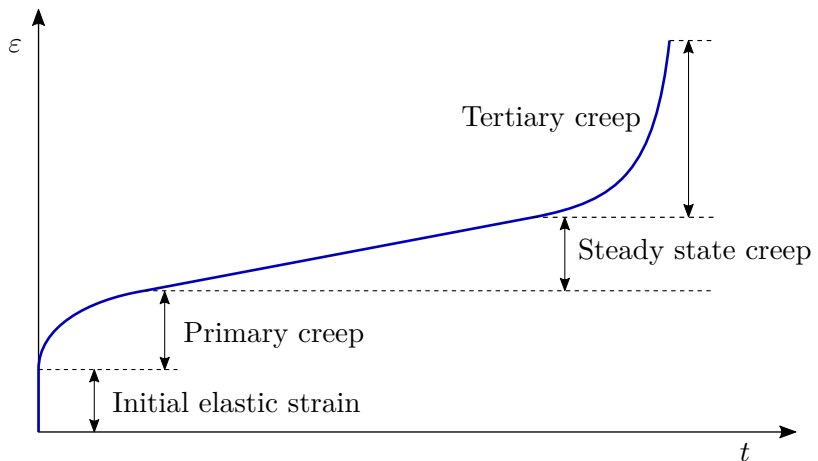


Figure 2.5: Example of creep deformation.

The viscoplasticity theory expressed in the present work is based on a generalized Duvaut-Lions [8–10] rate-sensitive formulation. Its main assumptions are illustrated in Figure 2.6, where for simplicity’s sake no hardening and consequent size growth of the yield function is taken into account.

As qualitatively illustrated in Fig. 2.6, we consider an initial stress state σ_{n-1} and a loading increment Δt during which a certain strain increment $\Delta \varepsilon$ takes place. Assuming the presence of plastic flow, we can compute two limiting solutions for the updated stress σ_n :

1. The **low-rate solution** σ^L , corresponding to the quasistatic solution which can be found by solving the rate-independent (thermo)plasticity equations described in Sections 2.1.3 and 2.2.2. According to the Prager consistency condition, the stress state inevitably lies on the yield surface.
2. The **high-rate solution** σ^H , corresponding to insufficient time for any inelastic damage to develop. This solution is therefore a purely elastic step, corresponding to the trial elastic stress lying outside the yield function.

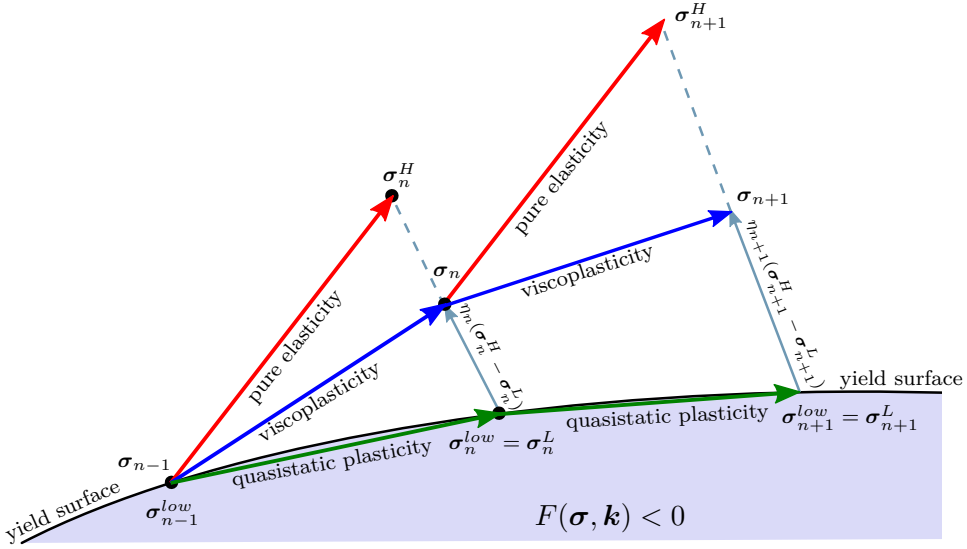


Figure 2.6: Conceptual illustration of rate-dependent plasticity. For a given strain increment, the viscoplastic solution is found between two limiting stress states: the ‘high rate’ solution σ^H which is the simple trial elastic stress and the ‘low rate solution’ corresponding to the quasistatic plastic solution.

We can therefore assume that there exist a strain dependent scalar η between 0 and 1 allowing the linear interpolation

$$\sigma \approx \sigma^L + \eta(\sigma^H - \sigma^L). \quad (2.39)$$

If the initial stress is on the yield surface, the expression of the rate factor η which depends on the time-step Δt can be written as

$$\eta = \frac{1 - e^{-\Delta t/\tau}}{\Delta t/\tau}, \quad (2.40)$$

where τ is a material parameter called the *characteristic response time* of the material.

In the following, it will be proven that starting from the end of a viscoplastic step, corresponding to a stress state outside the yield function, the scale factor is smaller than the value cited in Eq. (2.40). Consequently, the ‘attraction’ that the viscoplastic stress has for the quasistatic stress increases moving farther from the yield surface.

It is underlined that, due to the increased stiffness in case of high strain rate scenarios, the yield stress might ‘appear’ higher. However, the proposed formulation does not influence the yield point of the material, which is uniquely defined by the yield surface.

2.3.2 Viscoplasticity equations

Rate-independent solutions for stress state $\boldsymbol{\sigma}^L$ and internal variables \mathbf{k}^L are presumed to exist and to be computable from the constitutive equations described in Secs. 2.1.3 and 2.2.2.

Viscous effects are included decomposing the strain rate $\dot{\boldsymbol{\epsilon}}$ as

$$\dot{\boldsymbol{\epsilon}} = \dot{\boldsymbol{\epsilon}}_e + \dot{\boldsymbol{\epsilon}}_{vp}, \quad (2.41)$$

where $\dot{\boldsymbol{\epsilon}}_e$ and $\dot{\boldsymbol{\epsilon}}_{vp}$ are respectively elastic and ‘viscoplastic’ parts of the strain rate. $\dot{\boldsymbol{\epsilon}}_{vp}$ includes both the usual (quasi-static) plastic strain rate and the retarding contributions resulting from viscosity.

The viscoplastic strain rate can be calculated as

$$\dot{\boldsymbol{\epsilon}}_{vp} = \frac{1}{\tau} \mathbb{E}^{-1}(\boldsymbol{\sigma} - \boldsymbol{\sigma}^{low}), \quad (2.42)$$

while the internal state variables vary according to

$$\dot{\mathbf{k}} = \frac{-1}{\tau}(\mathbf{k} - \mathbf{k}^{low}), \quad (2.43)$$

where $\boldsymbol{\sigma}^{low}$ and \mathbf{k}^{low} are respectively the values of the rate-independent stress and internal variables throughout the time interval, which are ultimately equal to the low rate solutions $\boldsymbol{\sigma}^L$ and \mathbf{k}^L at the end of the step.

As usual, the stress rate is given by

$$\dot{\boldsymbol{\sigma}} = \mathbb{E}\dot{\boldsymbol{\epsilon}}_e. \quad (2.44)$$

Thus, using Eq.(2.42), we can write

$$\dot{\boldsymbol{\sigma}} = \dot{\boldsymbol{\sigma}}^{high} - \frac{1}{\tau}(\boldsymbol{\sigma} - \boldsymbol{\sigma}^{low}), \quad \text{where} \quad \dot{\boldsymbol{\sigma}}^{high} = \mathbb{E}\dot{\boldsymbol{\epsilon}}, \quad (2.45)$$

where $\boldsymbol{\sigma}^{high}$ is the elastic trial stress throughout the time step, ultimately equal to $\boldsymbol{\sigma}^H$ at the end of the step.

Equation 2.45 represents a set of first order differential equation that could be solved exactly if the analytical expression of $\boldsymbol{\sigma}^{low}$ as a function of time would be known throughout the time step. However, since the solution of the quasistatic equations is usually computed numerically, with the use of the methods introduced in Ch. (3), the value of $\boldsymbol{\sigma}^{low} = \boldsymbol{\sigma}^L$ is known only at the end of the time step.

Nevertheless, $\boldsymbol{\sigma}^{low}$ can be well approximated over the step in the manner described in the following.

Let us introduce a new variable \mathbf{u} defined as

$$\mathbf{u} = \boldsymbol{\sigma} - \boldsymbol{\sigma}^{high}, \quad (2.46)$$

so that Eq. (2.45) can be written as

$$\dot{\mathbf{u}} = -\frac{1}{\tau}(\mathbf{u} + \boldsymbol{\sigma}^{high} - \boldsymbol{\sigma}^{low}). \quad (2.47)$$

The increment $\dot{\boldsymbol{\sigma}}^{low}$ is assumed to be constant over the step and consequently the rate-independent stress $\boldsymbol{\sigma}^{low}$ varies linearly over the step. Therefore, the quasi-static stress rate $\dot{\boldsymbol{\sigma}}^{low}$ is an oblique projection of the (known) trial stress rate $\boldsymbol{\sigma}^{high}$. By applying the mean value theorem, we can write that

$$(\boldsymbol{\sigma}^{high} - \boldsymbol{\sigma}^{low}) \approx (\boldsymbol{\sigma}^H - \boldsymbol{\sigma}^L) \left(\frac{t - t_0}{\Delta t} \right) + (\boldsymbol{\sigma}_0^{high} - \boldsymbol{\sigma}_0^{low}) \left(1 - \frac{t - t_0}{\Delta t} \right). \quad (2.48)$$

With the introduced approximation, Eq.(2.47) can be integrated exactly. Being $\boldsymbol{\sigma}^{high} = \boldsymbol{\sigma}^{low}$ at the beginning of the time step, the initial condition is $\mathbf{u} = 0$ at $t = t_0$. Therefore, the solution is found as

$$\boldsymbol{\sigma} = \boldsymbol{\sigma}^L + R_H(\boldsymbol{\sigma}^H - \boldsymbol{\sigma}^L) + r_h(\boldsymbol{\sigma}_0^{high} - \boldsymbol{\sigma}_0^{low}), \quad (2.49)$$

where

$$R_H = \frac{1 - e^{-\Delta t/\tau}}{\Delta t/\tau} \quad \text{and} \quad r_h = e^{-\Delta t/\tau} - R_H. \quad (2.50)$$

If we approximate that $\boldsymbol{\sigma}_0^{high} - \boldsymbol{\sigma}_0^{low}$ is *parallel* to $\boldsymbol{\sigma}^H - \boldsymbol{\sigma}^L$, we can put Eq.(2.49) in the form of Eq. (2.39) as

$$\boldsymbol{\sigma} = \boldsymbol{\sigma}^L + \eta(\boldsymbol{\sigma}^H - \boldsymbol{\sigma}^L), \quad (2.51)$$

while the general expression of η ,

$$\eta = R_H + r_h \Upsilon, \quad \text{where} \quad \Upsilon = \frac{|\boldsymbol{\sigma}_0^{high} - \boldsymbol{\sigma}_0^{low}|}{|\boldsymbol{\sigma}^H - \boldsymbol{\sigma}^L|}, \quad (2.52)$$

is not equal to Eq. (2.40) unless the initial state is on the yield surface and $\boldsymbol{\sigma}_0^{high} = \boldsymbol{\sigma}_0^{low}$. This condition is verified only at the onset of yielding. The increase of Υ results in a lowered value of η , that makes the viscoplastic stress more strongly attracted to the quasistatic solution.

Similarly, the rate dependent update of the internal state variables can be computed as

$$\mathbf{k} = \mathbf{k}^L + R_H(\mathbf{k}^H - \mathbf{k}^L), \quad (2.53)$$

if the time variation over the step is approximated as

$$\mathbf{k} = \mathbf{k}^H + (\mathbf{k}^L - \mathbf{k}^H)(t - t_0)/\Delta t. \quad (2.54)$$

2.4 BP yield function

Piccolroaz and Bigoni [3–5] have proposed a yield function (referred as the BP yield function in the following) which is convex, smooth and extremely flexible, being able to reduce in limiting cases to several well-known models such as Von Mises, Tresca, Drucker-Prager, Mohr-Coulomb or Cam-Clay. The BP yield function is well-suited to represent quasi-brittle materials, rock-like materials, ceramics, concrete, soils. Furthermore, it is useful for the description of the powder-solid transition during industrial compaction processes which may involve high-temperature.

In the context of ceramic materials, both in the state of loose powder as in case of refractory devices, there are countless compositions that yield to the most different mechanical properties. Reproducing the behavior of a wide range of materials with a single constitutive model is a particularly challenging goal. The BP yield function has been used with good results in the development of the present work, with the purpose of generalize and unify procedures and concepts for material characterization and numerical analysis. In the following, the formulation and the main features of this yield criterion are introduced.

2.4.1 Definition

The BP yield function ([3]) is defined in terms of the stress tensor $\boldsymbol{\sigma}$ by

$$F(\boldsymbol{\sigma}) = f(p) + \frac{q}{g(\theta)}, \quad (2.55)$$

where, defining the parameter Φ as

$$\Phi = \frac{p + c}{p_c + c}, \quad (2.56)$$

the meridian and deviatoric functions are respectively written as

$$f(p) = \begin{cases} -Mp_c\sqrt{(\Phi - \Phi^m)[2(1 - \alpha)\Phi + \alpha]}, & \Phi \in [0, 1], \\ +\infty, & \Phi \notin [0, 1], \end{cases} \quad (2.57)$$

and

$$\frac{1}{g(\theta)} = \cos \left[\beta \frac{\pi}{6} - \frac{\cos^{-1}(\gamma \cos 3\theta)}{3} \right], \quad (2.58)$$

in which p , q and θ (the Lode's angle) are the following stress invariants

$$p = -\frac{\text{tr } \boldsymbol{\sigma}}{3}, \quad q = \sqrt{3J_2}, \quad \theta = \frac{1}{3} \arccos \left(\frac{3\sqrt{3}}{2} \frac{J_3}{J_2^{3/2}} \right), \quad (2.59)$$

functions of the second and third invariant of the deviatoric stress \mathbf{S}

$$J_2 = \frac{1}{2} \text{tr } \mathbf{S}^2, \quad J_3 = \frac{1}{3} \text{tr } \mathbf{S}^3, \quad \mathbf{S} = \boldsymbol{\sigma} - \frac{\text{tr } \boldsymbol{\sigma}}{3} \mathbf{I}, \quad (2.60)$$

\mathbf{I} being the identity tensor.

The yield function (2.55)–(2.57) is convex when the seven material parameters defining the meridian shape function $f(p)$ and the deviatoric shape function $g(\theta)$ lie within the following intervals

$$\begin{aligned} M > 0, \quad p_c > 0, \quad c \geq 0, \quad 0 < \alpha < 2, \\ 0 \leq \beta \leq 2, \quad 0 \leq \gamma \leq 1, \quad m > 1. \end{aligned} \quad (2.61)$$

2.4.2 Shape distortion and flexibility

The seven, non-negative material parameters of the BP yield function define the shape of the associated yield surface. In particular:

- The parameter M (dimensionless) controls the pressure-sensitivity.
- Parameters m and α define the distortion of the meridian section.
- The shape of the deviatoric section is regulated by β and γ , where $\gamma \rightarrow 1$ leads to a piece-wise linear deviatoric surface.

The expression (2.58) of $g(\theta)$ was proposed by Podgórski (1984; 1985) and independently by Bigoni and Piccolroaz (2004).

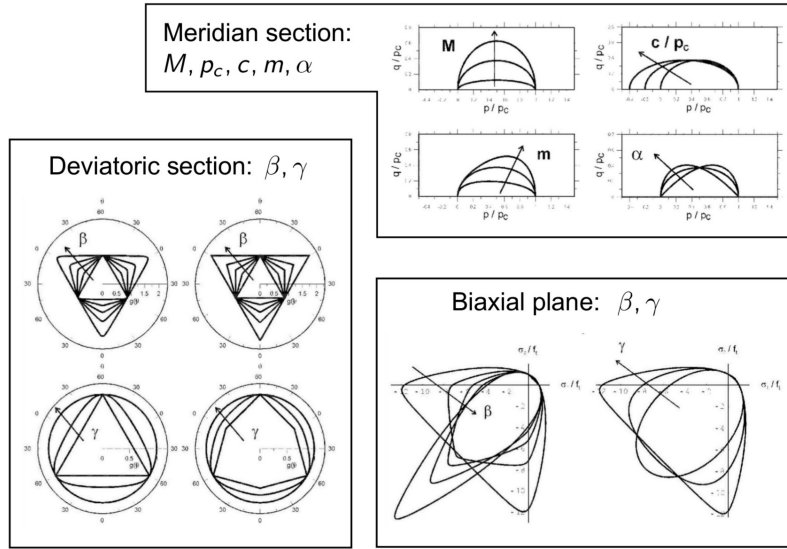


Figure 2.7: Shape distortion of the BP yield function in the meridian and deviatoric planes and associated governing parameters.

- p_c and c are respectively the yield strengths under ideal isotropic compression and tension, respectively.

The effects of each parameter on the yield function shape is qualitatively shown in Fig. 2.7. The distortion of meridian section obtained by changing parameters M , m , c/p_c and α is shown in the upper-right part of Fig. 2.7. In particular, it is to note that the shape distortion induced by the variation of parameters m and α is crucial to fit experimental results relative to frictional materials.

The possibility of extreme shape distortion of the deviatoric section represent a unique capability of the BP model. The deviatoric shape may range between upper and lower convexity limits and approach the Tresca, von Mises and Mohr-Coulomb criteria.

This is depicted on the left part of Fig. 2.7, where function $g(\theta)$ is normalized through division by $g(\pi/3)$ so that all deviatoric sections coincide at the point $\theta = \pi/3$.

The use of the BP criterion therefore may allow one to obtain a convex, smooth approximation of several yielding criteria and possible combinations of them, so that it can be considered of very general validity.

If this is not substantial from a theoretical point of view, it clearly avoids the necessity of introducing independent yielding mechanisms and the related complications.

Chapter 3

Numerical Implementation

In solid mechanics, the solution of nonlinear boundary value problems is based on *iterative numerical* solution of a discretized version of the momentum balance equations. The main steps involved in the procedure can be summarized as follows:

- (a) The discretized equilibrium equations yield to incremental displacements which are used to calculate incremental strains $\Delta\boldsymbol{\varepsilon}$ through the kinematic relations;
- (b) Given valid initial conditions and the incremental strains calculated in step (a), the *local* constitutive equations are integrated and new values of the state variables \mathbf{k} and stress $\boldsymbol{\sigma}$ are computed.
- (c) The equilibrium balance is checked for the computed stresses and, if this is violated, the iterative procedure is continued by returning to step (a).

In the computational solution of the cited problem, steps (a) and (c) are usually carried out at a global level by Finite Element/Finite Differences codes. Step (b) may be considered the *central problem of computational plasticity* [11] and is strongly related to the nature of the considered constitutive model.

This Chapter illustrates the common practices for the use of custom constitutive models inside conventional Finite Element codes and introduces new numerical strategies for the efficient integration of the local constitutive equations in case of pathological yield functions. Pathologies of yield functions may include: complex

valued functions outside the elastic domains, functions with false elastic domains, functions which become non-smooth in some regions of the stress space. Note that the Bigoni-Piccolroaz yield function defined in Sec. 2.4 is affected by one of these pathologies, namely it is defined $+\infty$ in some parts of the stress space outside the elastic domain.

Three algorithms for integration of constitutive models with a pathological yield function are developed and efficiently applied to the BP criterion [3, 4]. These algorithms are: (i.) an explicit integration scheme based on a forward Euler technique with a ‘centre-of-mass’ return correction, (ii.) an implicit integration scheme based on a ‘cutoff-substepping’ return algorithm and (iii.) a return mapping procedure combined with the implicit definition of the yield function.

Special focus is given to the evaluation of the numerical performance of the proposed integration algorithms, both producing particular iso-error maps in the stress-space and comparing semi-analytical solution of mechanical and thermo-mechanical problems with the numerical results obtained with the implemented user-material subroutines.

3.1 User-defined material models in Finite Element Codes

Some advanced FE software (e.g. Abaqus, Ansys, Code Aster, CalculiX) allow the implementation of custom material models in user material subroutines interfacing with the main code through a standardized parameter list. These subroutines define only the material response, while the iterative solution of the momentum equations is handled by the FE software, so that their use in the context of material modeling is extremely convenient.

The material models presented in Chapters 5, 6 and 7 have been implemented in Abaqus UMAT (User MATerial) subroutines. For the ceramic powder densification model presented in Ch. 5, an alternative version of the code has been produced to be used in the Ansys environment, where the user material subroutine is named USERMAT. Although some negligible convention differences between the FE codes are found, the operations executed from the user subroutine are usually coincident and can be summarized as in Box 1.

Box 1: User material subroutine

- (1) At the current time-step $n + 1$ the variables stress $\boldsymbol{\sigma}_n$, strain $\boldsymbol{\varepsilon}_n$, state variables \mathbf{k}_n and strain increment $\Delta\boldsymbol{\varepsilon}_{n+1}$ are provided as input to the user material subroutine;
- (2) Update the total strain $\boldsymbol{\varepsilon}_{n+1} = \boldsymbol{\varepsilon}_n + \Delta\boldsymbol{\varepsilon}_{n+1}$;
- (3) Integrate the constitutive equations using the preferred numerical strategy (see Sec. 3.2);
- (4) Update the stress $\boldsymbol{\sigma}_{n+1}$ and the vector of state variables \mathbf{k}_{n+1} ;
- (5) Compute the Jacobian $\mathbf{J} = \frac{\partial\Delta\boldsymbol{\sigma}}{\partial\Delta\boldsymbol{\varepsilon}}$ and the thermal Jacobian $\mathbf{J}_T = \frac{\partial\Delta\boldsymbol{\sigma}}{\partial\Delta T}$;
- (6) Return $\boldsymbol{\sigma}_{n+1}$, \mathbf{k}_{n+1} , \mathbf{J} and \mathbf{J}_T to the FE code .

At each Gauss point of each element, the user subroutine is called by the main FE code and receives as input the stress $\boldsymbol{\sigma}$, the strain $\boldsymbol{\varepsilon}$ and the vector of state dependent variables \mathbf{k} computed at the previous time-step. The current (guess) strain increment $\Delta\boldsymbol{\varepsilon}$ is also passed to the subroutine. State variables and stress values are updated through integration of the particular constitutive equations associated to the chosen material model using the preferred numerical procedure. As already mentioned, pathological yield criteria such as the BP yield function (see Sec. 2.4) require non-standard integration algorithms, which are described in Sec. 3.2.

Particularly delicate is the computation of the material Jacobian Matrix for the mechanical constitutive model $\frac{\partial\Delta\boldsymbol{\sigma}}{\partial\Delta\boldsymbol{\varepsilon}}$ and, in case of coupled temperature-displacement analysis, the thermal Jacobian $\frac{\partial\Delta\boldsymbol{\sigma}}{\partial\Delta T}$. These operators must be accurately computed and returned to the main FE code in order to achieve rapid convergence of the global Newton scheme. In many cases, their accuracy is the most important factor governing the convergence rate. However, the precision of the Jacobian does not affect the results of the analysis, if these are obtained.

In the computation of the Jacobian matrix, it must be considered that the solution of an asymmetric system of equations is as much as four times more expensive than the corresponding symmetric system. Some features of the constitutive model, such as

non-associative flow rule, lead to asymmetric Jacobian matrix and imply therefore the solution of an asymmetric system of equations at global scale. Thus, in case of slightly asymmetric constitutive Jacobian, it might be computationally more efficient to use a symmetric approximation and accept a slower convergence rate.

The complexity and the size of the tensor derivatives required for the iterative solution of the local constitutive equations and the computation of the consistent Jacobian penalizes the development of advanced constitutive models.

In the implementation of the constitutive models presented in Chapters 5, 6 and 7, the advanced hybrid symbolic-numeric approach implemented in AceGen [12, 13] results to be a particularly valuable tool. This symbolic code generator combines automatic differentiation techniques (AD) and optimization of formulae, providing therefore an optimal environment for designing and implementing numerical code.

AceGen is available as a package of Wolfram Mathematica and permits the automatic generation of computer code in several programming languages (e.g. C++, FORTRAN, MATLAB), therefore speeding up the UMAT development and allowing frequent improvements of the numerical procedures. Benchmarks of the generated code are also possible within the Mathematica environment by means of the FE code AceFEM.

3.2 Stress-point integration algorithms for constitutive models with a pathological yield function

Used in the context of elastoplastic modelling, the BP yield function (defined in Sec. 2.4) introduces the problem that to be convex, it has been defined $+\infty$ in certain regions in the stress-space outside the elastic domain. Therefore, in its original form, the BP yield function cannot be implemented within an elastoplastic integration scheme, if a gradient-based return-mapping algorithm is used, for which the gradient of the yield function is needed everywhere in the stress-space [11]. If a non-convex version of the BP yield function (obtained by squaring the terms) is implemented with a return-mapping algorithm, wrong results can be produced, as a specific example will demonstrate.

The problem of the BP yield surface is also common to other yield surfaces for geomaterials (see Brannon and Leelavanichkul,

2010), so that the aim of the present Section is to overcome the difficulty by proposing three algorithms: the first is based on a forward Euler technique with a correction based on a ‘centre-of-mass’ return scheme, fully applicable to the original form of the BP yield function (defined $+\infty$ outside the yield surface); the second is based on a cutoff-substepping return-mapping algorithm that can be applied on the squared (and non-convex) version of the BP yield function; the last strategy, initially proposed by Stupkiewicz et al. [7], involves the implicit redefinition of the BP yield function, in order to enforce its convexity and finiteness.

3.2.1 The ‘centre of mass’ integration algorithm

As previously mentioned, the problem with the BP yield function is that it is defined $+\infty$ in some regions outside the elastic domain (for $p \notin [-c, p_c]$), Fig. 3.1. Therefore, an integration algorithm based on a standard return mapping technique cannot work, so that the purpose of this Section is to introduce an explicit forward Euler algorithm to solve this problem (while an implicit algorithm will be presented in the next Section defined on a ‘squared version’ of the yield function).

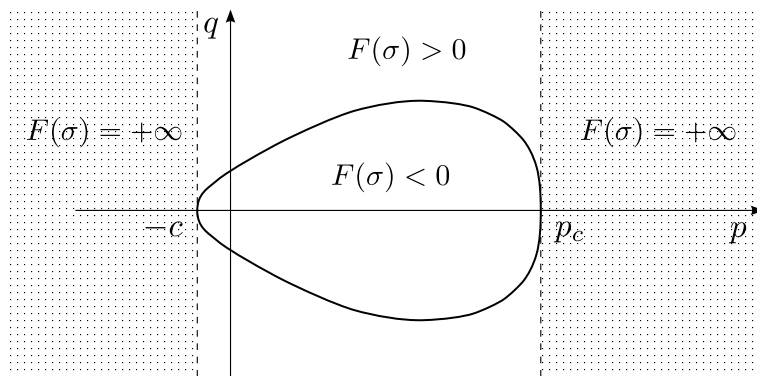


Figure 3.1: The BP yield function represented as a surface in the p - q plane.

Centre of mass of the BP yield surface

The numerical integration algorithm that will be developed later is based on the knowledge of the centre of mass of the yield surface. This, with reference to Fig. 3.2, can be obtained as follows.

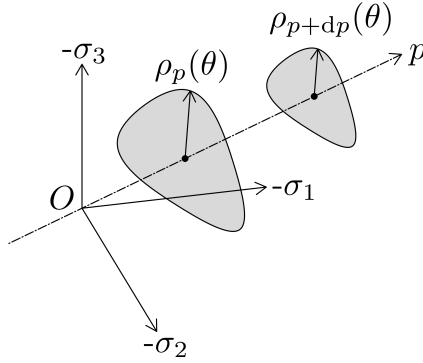


Figure 3.2: Radius $\rho(\theta)$ and centre of mass of two indicative deviatoric sections (located at different mean stresses p) of the BP yield surface. Due to the isotropy symmetries of the deviatoric sections, the mass centres lie on the hydrostatic axis.

We begin by noting that the yield surface possesses the isotropy symmetries in the deviatoric plane (see Bigoni and Piccolroaz, 2004), therefore, the centre of mass of the yield surface lies on the hydrostatic axis. The infinitesimal area of the deviatoric section can be evaluated as

$$dA = \frac{1}{2}\rho^2(\theta) d\theta, \quad (3.1)$$

where

$$\rho(\theta) = \sqrt{\frac{2}{3}}q = -\sqrt{\frac{2}{3}}f(p)g(\theta), \quad (3.2)$$

is the radius of the surface boundary evaluated with respect to the hydrostatic axis, so that the area of the deviatoric section is expressed as

$$A(p) = 2f^2(p) \int_0^{\frac{\pi}{3}} g^2(\theta) d\theta. \quad (3.3)$$

On application of the definition of the centre of mass

$$p_G = \frac{\int_{-c}^{p_c} p A(p) dp}{\int_{-c}^{p_c} A(p) dp}, \quad (3.4)$$

provides the *coordinate of the centre of mass of the BP yield surface along the hydrostatic axis*

$$p_G = \frac{(m+1)p_c [(\alpha-3)m-6] + c[6(\alpha+1) + m(m+7)]}{(m+3)[(\alpha-4)m-2(\alpha+2)]}, \quad (3.5)$$

a formula involving all the *meridian* parameters of the yield function, except M .

The ‘centre of mass’ return algorithm

We propose a numerical integration procedure for rate elastoplastic constitutive equations based on a return algorithm which is geometrically sketched in Fig. 3.3 and can be synthetically described with reference to Box 2.

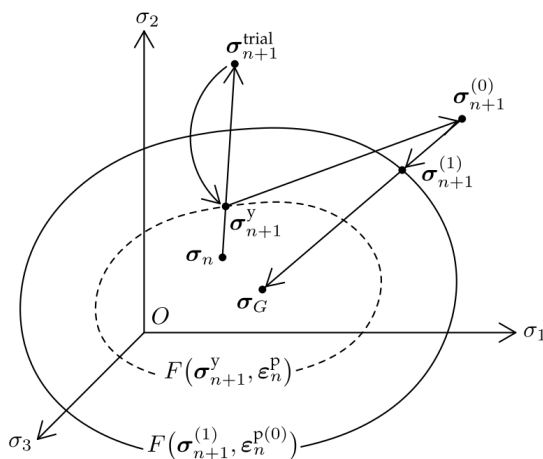


Figure 3.3: Geometrical sketch of the ‘centre of mass return algorithm’ for the integration of rate elastoplastic constitutive equations.

In particular, starting from a given state at a step n [point (1) in Box 2] and after the usual trial elastic step [point (2)], the stress point at yielding is found along the line joining the trial and the initial state [point (3)]; from this point, after the purely elastic strain is eliminated from the strain increment [point (4)], a new stress increment is found using the tangent elastoplastic operator [point (5)]; the plastic strain increment is updated [point (6)]; and finally, a return on the updated yield surface is performed along the line joining with the centre of mass of the yield surface [points (7)–(8)].

Box 2: The ‘centre of mass’ integration algorithm

- (1) Given an initial state at step n , described by the variables $\boldsymbol{\sigma}_n, \boldsymbol{\varepsilon}_n^e, \boldsymbol{\varepsilon}_n^p$ and given a strain increment $\Delta\boldsymbol{\varepsilon}$;

- (2) evaluate the elastic trial solution

$$\boldsymbol{\sigma}_{n+1}^{\text{trial}} = \boldsymbol{\sigma}_n + \mathbb{E}[\Delta\boldsymbol{\varepsilon}];$$

- (3) along the line from $\boldsymbol{\sigma}_n$ to $\boldsymbol{\sigma}_{n+1}^{\text{trial}}$ find the stress point $\boldsymbol{\sigma}_{n+1}^y$ at yielding

$$F(\boldsymbol{\sigma}_{n+1}^y, \boldsymbol{\varepsilon}_n^p) = 0;$$

- (4) evaluate the elastic deformation increment corresponding to $\boldsymbol{\sigma}_{n+1}^y - \boldsymbol{\sigma}_n$

$$\Delta\boldsymbol{\varepsilon}_{n+1}^y = \mathbb{E}^{-1}[\boldsymbol{\sigma}_{n+1}^y - \boldsymbol{\sigma}_n];$$

- (5) evaluate the stress increment via the tangent elastoplastic operator

$$\boldsymbol{\sigma}_{n+1}^{(0)} = \boldsymbol{\sigma}_{n+1}^y + \mathbb{C}[\Delta\boldsymbol{\varepsilon} - \Delta\boldsymbol{\varepsilon}_{n+1}^y];$$

- (6) update the plastic deformation

$$\boldsymbol{\varepsilon}_{n+1}^{p(0)} = \boldsymbol{\varepsilon}_n^p + \Delta\boldsymbol{\varepsilon} - \mathbb{E}^{-1}[\boldsymbol{\sigma}_{n+1}^{(0)} - \boldsymbol{\sigma}_n];$$

- (7) find the stress $\boldsymbol{\sigma}_{n+1}^{(1)}$ on the updated yield surface

$$F(\boldsymbol{\sigma}_{n+1}^{(1)}, \boldsymbol{\varepsilon}_{n+1}^{p(0)}) = 0;$$

- (8) update the plastic deformation for the final stress state on the yield surface

$$\boldsymbol{\varepsilon}_{n+1}^{p(1)} = \boldsymbol{\varepsilon}_n^p + \Delta\boldsymbol{\varepsilon} - \mathbb{E}^{-1}[\boldsymbol{\sigma}_{n+1}^{(1)} - \boldsymbol{\sigma}_n];$$

- (9) EXIT.

There are two ‘find’ in the procedure explained in Box 2: the first is at point (3) and the second is at point (7). Both correspond to a root-finding procedure for a scalar function (the yield function) of tensorial variable (the stress), which can be pursued

with different numerical techniques, so that we have employed a bisection method. Regarding the ‘find’ at point (3), the zero of F is sought along the segment joining σ_n with $\sigma_{n+1}^{\text{trial}}$, while no directions are *a-priori* prescribed for returning on the yield surface from the stress state $\sigma_{n+1}^{(0)}$ at point (5). We propose to find the zero of $F(\sigma_{n+1}^{(1)}, \varepsilon_{n+1}^p{}^{(0)}) = 0$ along the segment drawn from $\sigma_{n+1}^{(0)}$ to the centre of mass of the yield surface, σ_G [defined by parameter p_G , Eq. (3.5)].

Note finally that the presented numerical algorithm has the inconvenient typical of explicit methods, for which there is a small discrepancy at the end of the procedure, in the sense that the stress point lies on a yield surface which does not correspond to the updated values of hardening. A procedure alternative to the centre-of-mass algorithm is introduced in the next Section.

3.2.2 The ‘cutoff-substepping’ integration algorithm

As an alternative to the forward Euler procedure with ‘centre of mass’ return correction introduced in the previous Section, we propose an implicit integration scheme. Since the standard return mapping algorithm does not work in a zone of the stress-space, this zone can be delimited by introducing a cutoff plane orthogonal to the hydrostatic axis, so that a new algorithm can be set up in which the return mapping scheme is augmented of a substepping when the trial elastic stress falls within that zone. In particular, if the trial elastic solution σ^{trial} falls on the same side of the plane as the starting point, the return mapping algorithm correctly converges (as demonstrated in Section 3.2.2), while, if it falls beyond the cutoff plane, an iterative subincrementation is performed, in which the strain increment $\Delta\varepsilon$ is subdivided and the return mapping is iteratively applied with successive updates of the BP yield function, so that, eventually, the entire initial step will be performed remaining within the correct stress zone.

The position of this cutoff plane depends on shape and size of the BP yield surface, see Fig. 3.4, and can be determined as follows.

The squared BP yield function and the cutoff plane

The squared BP yield function is obtained by squaring the terms in equation (2.57), so that its meridian part (divided by

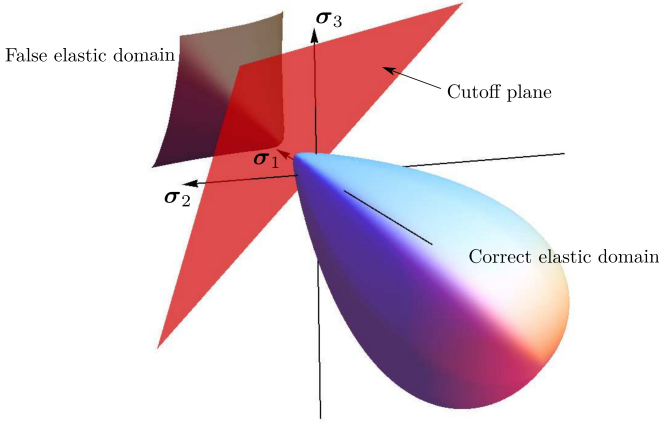


Figure 3.4: Cutoff plane for the BP yield surface. Stress points where the return mapping algorithm works correctly are on the side of the plane where the yield surface lies. The false elastic domain is shown brown.

p_c) can be written as

$$\tilde{f}(\Phi) = M^2 (\Phi - \Phi^m) [2(1 - \alpha)\Phi + \alpha]. \quad (3.6)$$

The first and second derivatives of this function with respect to Φ are

$$\frac{d\tilde{f}(\Phi)}{d\Phi} = M^2 \left\{ 2(1 - \alpha) [2\Phi - (1 + m)\Phi^m] + \alpha(1 - m\Phi^{m-1}) \right\}, \quad (3.7)$$

and

$$\frac{d^2\tilde{f}(\Phi)}{d\Phi^2} = M^2 \left\{ 2(1 - \alpha) \left[2 - m(1 + m)\Phi^{m-1} \right] - \alpha m(m - 1)\Phi^{m-2} \right\}, \quad (3.8)$$

respectively. Note that the squared BP yield function is differentiable (its first and second derivatives are defined everywhere), but, in general, is no longer convex and displays a so-called ‘false elastic domain’ (a nomenclature introduced by Brannon and Leela-
vanichkul, 2010), visible in Fig. 3.4. For this reason, the Newton-Raphson algorithm

$$\Phi_{n+1} = \Phi_n - \frac{\tilde{f}(\Phi_n)}{\left. \frac{d\tilde{f}(\Phi)}{d\Phi} \right|_{\Phi_n}}, \quad (3.9)$$

in general fails to converge. Nevertheless, it is possible to demonstrate that, for the squared BP yield function, a non-convex region exists in which the Newton-Raphson method still converges, despite the non-convexity. The region is delimited by the above-introduced cutoff plane, which position can be determined as follows.

Position of the cutoff plane

Let us consider the situation sketched in Fig. 3.5. The generic

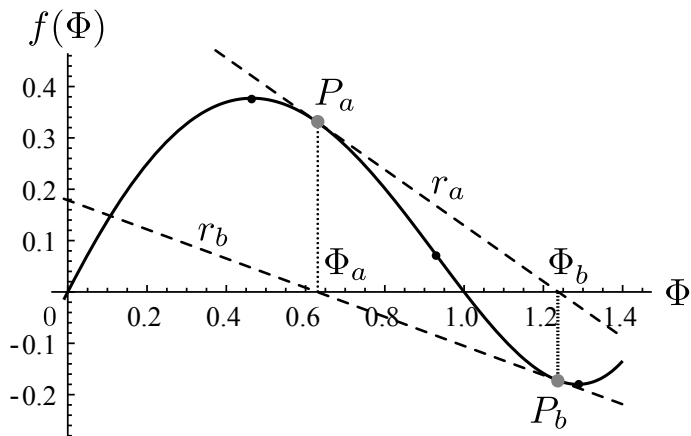


Figure 3.5: Determination of the position of the cutoff plane. Local stationary (maximum and minimum) and inflection points are denoted by black spots, while the bounds of the non-convex region (in which the Newton-Raphson algorithm can be still used) are shown gray. The dashed lines r_a and r_b are the tangent lines to the meridian function at the points P_a and P_b , respectively. The graph $\tilde{f}(\Phi)$ has been obtained with the following set of parameters: $M = 1$, $m = 3$, $\alpha = 1.5$, $p_c = 100$ MPa, and $c = 10$ MPa.

points $P_a = (\Phi_a, \tilde{f}(\Phi_a))$ and $P_b = (\Phi_b, \tilde{f}(\Phi_b))$ lie on the meridian function, so that it is possible to calculate in those points the tangents

$$r_a: \tilde{f}(\Phi) = \tilde{f}(\Phi_a) + \tilde{f}'(\Phi_a)(\Phi - \Phi_a), \quad (3.10)$$

and

$$r_b: \tilde{f}(\Phi) = \tilde{f}(\Phi_b) + \tilde{f}'(\Phi_b)(\Phi - \Phi_b), \quad (3.11)$$

where a prime denotes the derivative with respect to Φ . If we impose that $(\Phi_a, 0) \in r_b$ and $(\Phi_b, 0) \in r_a$, we obtain the following non-linear algebraic system

$$\begin{cases} \tilde{f}(\Phi_a) + \tilde{f}'(\Phi_a)(\Phi_b - \Phi_a) = 0, \\ \tilde{f}(\Phi_b) + \tilde{f}'(\Phi_b)(\Phi_a - \Phi_b) = 0, \end{cases} \quad (3.12)$$

with the unknowns Φ_a and Φ_b ; these values, that can be calculated numerically, define the region $[\Phi_a, \Phi_b]$ in which the Newton-Raphson algorithm can be still used, even though the squared BP yield function is not convex.

As a conclusion, Φ_b is the value defining the position of the cut-off plane, to be used in the subincrementation scheme, as shown in Box 3 (note that Φ_a is not needed, since in the integration algorithm the trial elastic stress always lies outside the elastic domain).

Box 3: The ‘cutoff-substepping’ integration algorithm

- (1) Given an initial state at step n , described by the variables σ_n , ε_n^e , ε_n^p and given a strain increment $\Delta\varepsilon$;
- (2) Set $\Delta\varepsilon_i = \Delta\varepsilon$ and $m = 1$ (where m defines the substep interval);
- (3) INITIALIZE: all variables are set equal to the value at the initial step n ;
- (4) DO $i = 1, m$;
- (5) Evaluate the elastic trial solution

$$\sigma_{n+1,i}^{\text{trial}} = \sigma_n + \mathbb{E}[\Delta\varepsilon_i];$$

- (6) Calculate $\Phi_{n+1,i}^{\text{trial}} = \frac{p_{n+1,i} + c_n}{p_{c,n} + c_n}$ and Φ_b by solving Eq. (3.12);
- (7) Check position with respect to the cutoff plane
IF $\Phi_{n+1,i}^{\text{trial}} \leq \Phi_b$ GOTO Standard Return Mapping;
- (8) Substepping procedure
ELSE $m = 2m$ AND $\Delta\varepsilon_i = \frac{\Delta\varepsilon}{m}$;
- (9) GOTO (3)

3.2.3 Implicit BP yield function and return mapping algorithm

A different strategy [7] to overcome the cited difficulties related to non-convexity or non-finiteness of the BP yield function $F(\boldsymbol{\sigma}, \mathbf{k})$ is to define an alternative yield function $F^*(\boldsymbol{\sigma}, \mathbf{k})$ in such a way that its zero level surface $F^* = 0$ is coincident with that of the original yield function.

By doing so, we maintain the elastic domain and its closure equivalent, while enforcing finiteness and convexity of the new defined BP yield function $F^*(\boldsymbol{\sigma}, \mathbf{k})$.

Yield function redefinition

The problems in the numerical implementation are related to the only pressure-dependent part of the BP yield function $f(p)$. Thus, it is more efficient to apply the implicit definition in the $p - q$ space.

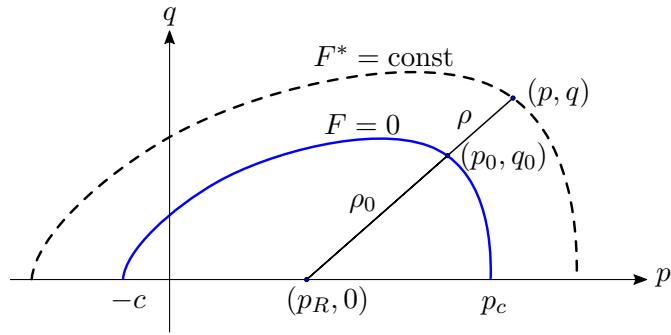


Figure 3.6: Construction of the implicit yield function F^* in the $p - q$ space.

For a fix Lode angle θ , the yield surface $F = 0$ can be represented in the $p - q$ space as shown in Fig. 3.6.

The implicit yield function F^* can be defined as

$$F^*(\boldsymbol{\sigma}, \mathbf{k}) = \frac{\rho}{\rho_0} - 1, \quad (3.13)$$

where ρ is the distance between current stress point (p, q) and a reference point $(p_R, 0)$ located on the p axis

$$\rho = \|\boldsymbol{\rho}\|, \quad \boldsymbol{\rho} = (p - p_R, q), \quad (3.14)$$

while ρ_0 is the distance between the image of (p, q) on the yield surface and $(p_R, 0)$

$$\rho_0 = \|\boldsymbol{\rho}_0\|, \quad \boldsymbol{\rho}_0 = (p_0 - p_R, q_0), \quad \boldsymbol{\rho} = (F^* + 1)\boldsymbol{\rho}_0. \quad (3.15)$$

Through Eq. (3.13) we generate a family of self-similar surfaces, which are scaled with respect to the chosen reference point $(p_R, 0)$, where p_R is assumed equal to $(p_c + c)/2$. It is underlined that different choices for the reference point could be made, as for instance the ‘centre of mass’ of the considered yield function (see Sec. 3.2.1). If the ‘source’ yield surface $F = 0$ is convex, self-similarity implies convexity also of the implicit yield function F^* .

Figure 3.7 shows the iso-surfaces of the BP yield function in the principal stress space, where the cross-section corresponding to the generating yield surface $F = 0$ is marked in red color.

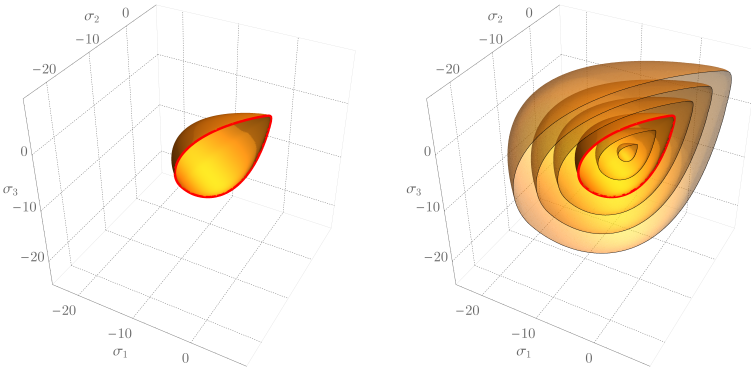


Figure 3.7: A convex and smooth BP yield surface (left). Iso-surfaces of the corresponding implicit BP yield function in the principal stress space (right). The zero-level surface is marked in red color.

The implicit yield function F^* can be calculated according to Eq. (3.13) for given value of the distance ρ_0 . From the condition that the image point lies on the yield surface we obtain the following nonlinear equation in ρ_0 (for fix \mathbf{k} and $\boldsymbol{\sigma}$)

$$F_0 = (\rho_0, \boldsymbol{\sigma}, \mathbf{k}), \quad (3.16)$$

Using the iterative Newton method we can compute numerically the solution ρ_0 as

$$\rho_0^{i+1} = \rho_0^i + \Delta\rho_0^i, \quad \Delta\rho_0^i = - \left(\frac{\partial F_0}{\partial \rho_0} \right)^{-1} F_0(\rho_0^i), \quad (3.17)$$

which implicitly depends on the stress $\boldsymbol{\sigma}$ and hardening variables \mathbf{k} .

Return mapping algorithm

In this particular case, associative flow rule and no thermal effects are considered.

In the following constitutive update problem, we want to find the updated values of plastic strain $\boldsymbol{\varepsilon}^p$, plastic multiplier λ and state variables \mathbf{k} , given their values at the previous time-step n and satisfying the elastic constitutive equation

$$\boldsymbol{\sigma}_{n+1} = \mathbb{E}(\boldsymbol{\varepsilon}_{n+1} - \boldsymbol{\varepsilon}_{n+1}^p), \quad (3.18)$$

the incremental (associative) flow rule

$$\boldsymbol{\varepsilon}_{n+1}^p = \boldsymbol{\varepsilon}_n^p + (\lambda_{n+1} - \lambda_n) \mathbf{Q}(\boldsymbol{\sigma}_{n+1}, \mathbf{k}_{n+1}), \quad \mathbf{Q} = \frac{\partial F}{\partial \boldsymbol{\sigma}}, \quad (3.19)$$

the complementarity conditions

$$F(\boldsymbol{\sigma}_{n+1}, \mathbf{k}_{n+1}) \leq 0, \quad \Delta\lambda \geq 0, \quad \Delta\lambda F(\boldsymbol{\sigma}_{n+1}, \mathbf{k}_{n+1}) = 0, \quad (3.20)$$

and the considered hardening rule

$$\mathbf{k}_{n+1} = \mathbf{h}(\boldsymbol{\varepsilon}_{n+1}^p). \quad (3.21)$$

The functions \mathbf{h} define the dependence of hardening state variables \mathbf{k} (e.g. p_c) on the plastic strain, while \mathbb{E} is the fourth-order elastic moduli tensor.

Box 4: The return mapping algorithm

1. Compute the trial elastic state

$$\boldsymbol{\sigma}_{n+1}^{trial} = \mathbb{E}[\boldsymbol{\varepsilon}_{n+1} - \boldsymbol{\varepsilon}_n^p], \quad F^{trial} = F(\boldsymbol{\sigma}_{n+1}^{trial}). \quad (3.22)$$

2. Check the yield condition: if $F^{trial} \leq 0$ then the step is elastic and

$$\boldsymbol{\varepsilon}_{n+1}^p = \boldsymbol{\varepsilon}_n^p, \quad \Delta\lambda = 0. \quad (3.23)$$

3. If $F^{trial} > 0$ then the step is plastic and the following nonlinear algebraic equations are solved for $\boldsymbol{\varepsilon}_{n+1}^p$ and $\Delta\lambda$:

$$\begin{aligned} 0 &= \boldsymbol{\varepsilon}_{n+1}^p - \boldsymbol{\varepsilon}_n^p - (\lambda_n - \lambda_{n-1}) \mathbf{Q}(\boldsymbol{\sigma}_{n+1}, \mathbf{k}_n), \\ 0 &= F(\boldsymbol{\sigma}_{n+1}, \mathbf{k}_{n+1}), \\ 0 &= \mathbf{k}_{n+1} - \mathbf{h}(\boldsymbol{\varepsilon}_{n+1}^p), \end{aligned} \quad (3.24)$$

where the stress $\boldsymbol{\sigma}_{n+1}$ is given by the constitutive equation (3.18).

The constitutive update problem is solved using the return mapping algorithm [11] which involves the sequence of steps listed in Box 4.

We define $\mathbf{u} = \{\boldsymbol{\varepsilon}_{n+1}^p, \lambda_{n+1}, \mathbf{k}_{n+1}\}$ and $\mathbf{H}(\mathbf{u})$ respectively as the vector of unknowns and the residual vector for the nonlinear system (3.24).

The numerical solution of $\mathbf{H}(\mathbf{u}) = \mathbf{0}$ can be found using the Newton method, which employs the iterative scheme

$$\mathbf{u}^{i+1} = \mathbf{u}^i + \Delta \mathbf{u}^i, \quad \Delta \mathbf{u}^i = - \left(\frac{\partial \mathbf{H}}{\partial \mathbf{u}} \right)^{-1} \mathbf{H}(\mathbf{h}^i), \quad (3.25)$$

with the typical initial guess $\mathbf{u}^0 = \{\boldsymbol{\varepsilon}_n^p, \lambda_n, \mathbf{k}_n\}$, corresponding to the *trial elastic step*.

According to the complementarity conditions, the computed stress $\boldsymbol{\sigma}_{n+1}$ belongs to the updated elastic domain $F(\boldsymbol{\sigma}_{n+1}, \mathbf{k}_{n+1}) \leq 0$. However, the trial elastic stress $\boldsymbol{\sigma}_{n+1}^{trial}$ can lie well outside the yield surface. Thus, the use of the return mapping algorithm requires the yield function to be defined and differentiable for arbitrary stress. The implicit definition of the BP yield function accomplishes these requirements and is therefore suitable for the application of this numerical procedure.

3.3 Numerical performance of the proposed algorithms

Beside the theoretical consistency, the computational performance, robustness and precision of the proposed algorithms are important parameters to evaluate.

In the following, the main purpose is to analyze the discrepancies between the proposed algorithms, while the correctness of the numerical results is not investigated. This task will be discussed in Sections 3.4 and 3.5, where four different model problems allowing for semi-analytical solutions are analyzed.

Special focus is given to the comparison between the newly introduced ‘centre-of-mass’ and ‘cut-off substepping’ algorithms. The robustness and convergence rate of the return mapping algorithm applied to the implicit definition of the BP yield function and of the ‘cut-off substepping’ algorithm are further investigated in a large FE analysis.

3.3.1 Finite step accuracy and iso-error maps

The numerical performance of the centre-of-mass integration technique has been tested by comparing results obtained for a prescribed finite step of deformation (taken in different directions in the hyperspace of symmetric tensors as elucidated in Table 3.1) with those obtained with the cutting-plane return-mapping technique applied to the ‘squared-version’ of the BP yield surface, without subincrementation. In this way, it will become evident that, for certain values of the trial elastic stress, convergence will not occur for the latter algorithm.

		Deformation	
		$\Delta\varepsilon_1$	$\Delta\varepsilon_2 = \Delta\varepsilon_3$
Test 1	Isotropic compression	-0.024	-0.024
Test 2	Isotropic traction	0.00013714	0.00013714
Test 3	Negative uniaxial deformation	-0.0080728	0
Test 4	Positive uniaxial deformation	0.00037312	0
Test 5	Triaxial compression	-0.0092839	-0.0185678
Test 6	Triaxial extension	-0.006091	-0.012182
Test 7	Shear	$\Delta\varepsilon_1 = -\Delta\varepsilon_2$	$\Delta\varepsilon_3$
		0.00078408	0

Table 3.1: Deformation steps $\Delta\varepsilon$ used for comparing the performance of the centre-of-mass integration algorithm with the return mapping, the latter performed on the squared version of the BP yield function.

The comparison between the two integration algorithms has been performed by assuming:

- a form of the yield surface, namely,

$$M = 0.26, \quad m = 2, \quad \alpha = 1.99, \quad \beta = 0.12, \quad \gamma = 0.98,$$

$$p_c = 350 \text{ MPa}, \quad c = 2 \text{ MPa},$$

- elastic parameters in terms of Lamé constants

$$\lambda = 2669.49 \text{ MPa}, \quad \mu = 4745.76 \text{ MPa},$$

- linear strain-hardening.

Note that the above parameters have been selected to be representative of a concrete-like material and the linear-hardening elastoplastic model has been implemented as a UMAT subroutine for Abaqus.

The strain steps prescribed in Table 3.1 for testing the capability of the integration algorithms and the corresponding trial elastic stresses are reported together with the strain-space and stress-space representations of the BP meridian sections, respectively in the upper and lower parts of Fig. 3.8, where θ is the Lode's angle, Eq. (2.59)₃. The trial elastic stresses in the deviatoric plane of the BP yield surface are reported in the central part of Fig. 3.8.

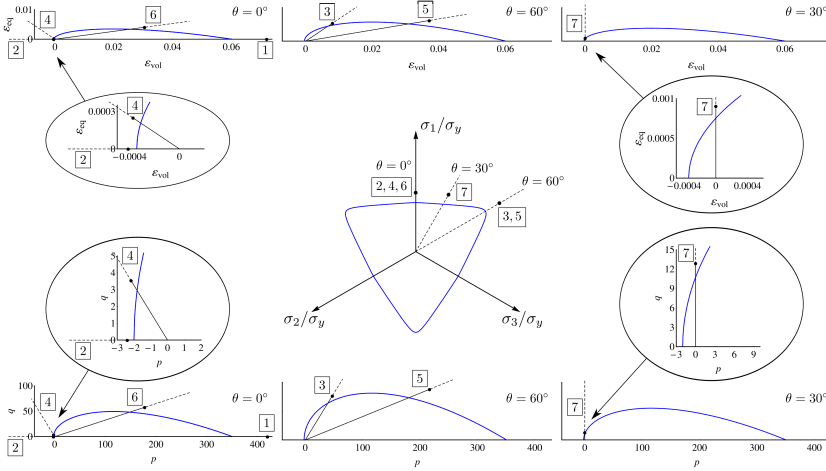


Figure 3.8: Prescribed finite strain steps in the strain-space (upper part) and corresponding elastic trial stresses in the deviatoric plane (central part) and meridian plane (lower part) of the stress-space, for tests 1 to 7 reported in Table 3.1. Finite steps are prescribed in such a way that the norm of the trial stress exceeds by 20% the norm of the corresponding yield stress along the radial path from the origin to the trial stress.

Note that the prescribed trial stresses have been given so that, in all cases, exactly the 20% of its norm lies outside the elastic domain, $\|\boldsymbol{\sigma}^{\text{trial}}\| = 1.2 \times \|\boldsymbol{\sigma}_y\|$. Results, in terms of stress and plastic strain reached at the end of the procedure, are reported in Tab. 3.2 for tests 1 to 6, while results of the test 7 are reported in Tabs. 3.3 and 3.4. In addition to the two algorithms under testing, a so-called ‘exact’ result has also been included. This is obtained through successive subdivision of the strain increment into a sufficiently large number of subincrements to achieve convergence within a high tolerance (so that the relative error between

the last two subincrements lies below 10^{-6}).

For the isotropic compression deformation path ('test 1') the return mapping algorithm fails to converge, as a consequence of the lack of convexity of the squared-version of the BP yield function, and therefore results are not reported in the table.

		Stress		Error	Plastic strain		Error
		σ_1	$\sigma_2 = \sigma_3$	%	ε_1^p	$\varepsilon_2^p = \varepsilon_3^p$	%
Test 1	Centre of mass	-384.8	-384.8	0.05	$-2.0103 \cdot 10^{-3}$	$-2.0103 \cdot 10^{-3}$	0.53
	Return mapping	-	-	-	-	-	-
	Exact	-384.8	-384.8		$-2.0210 \cdot 10^{-3}$	$-2.0210 \cdot 10^{-3}$	
Test 2	Centre of mass	2.002	2.002	0.00	$2.2726 \cdot 10^{-5}$	$2.2726 \cdot 10^{-5}$	0.00
	Return mapping	2.002	2.002	0.00	$2.2726 \cdot 10^{-5}$	$2.2726 \cdot 10^{-5}$	0.00
	Exact	2.002	2.002		$2.2726 \cdot 10^{-5}$	$2.2726 \cdot 10^{-5}$	
Test 3	Centre of mass	-95.56	-25.88	0.89	$-3.7303 \cdot 10^{-4}$	$3.5937 \cdot 10^{-4}$	8.56
	Return mapping	-94.56	-25.23	0.45	$-4.4081 \cdot 10^{-4}$	$3.2748 \cdot 10^{-4}$	4.25
	Exact	-94.89	-25.45		$-4.1833 \cdot 10^{-4}$	$3.3810 \cdot 10^{-4}$	
Test 4	Centre of mass	4.029	0.616	0.23	$3.3229 \cdot 10^{-5}$	$1.9628 \cdot 10^{-5}$	2.14
	Return mapping	4.015	0.628	0.31	$3.4796 \cdot 10^{-5}$	$1.8526 \cdot 10^{-5}$	2.93
	Exact	4.023	0.621		$3.3895 \cdot 10^{-5}$	$1.9159 \cdot 10^{-5}$	
Test 5	Centre of mass	-191.4	-261.2	0.04	$5.2867 \cdot 10^{-4}$	$-1.3881 \cdot 10^{-3}$	0.16
	Return mapping	-191.5	-261.4	0.09	$5.3819 \cdot 10^{-4}$	$1.0881 \cdot 10^{-3}$	1.08
	Exact	-191.3	-261.2		$5.2705 \cdot 10^{-4}$	$-1.3947 \cdot 10^{-3}$	
Test 6	Centre of mass	-193.0	-146.1	0.11	$-4.0150 \cdot 10^{-4}$	$7.4916 \cdot 10^{-4}$	1.52
	Return mapping	-192.8	-145.9	0.00	$-4.1020 \cdot 10^{-4}$	$7.3847 \cdot 10^{-4}$	0.22
	Exact	-192.8	-145.9		$-4.1020 \cdot 10^{-4}$	$7.3847 \cdot 10^{-4}$	

Table 3.2: Stress and plastic strain at the end of the finite step calculated with different algorithms for the strain and stress paths 1-6 of Table 3.1, graphically represented in Fig. 3.8.

		Stress			Error
		σ_1	σ_2	σ_3	%
Test 7	Centre of mass	6.460	-7.826	-0.433	0.61
	Return mapping	6.441	-7.741	-0.354	0.54
	Exact	6.450	-7.782	-0.391	

Table 3.3: Stress at the end of the finite step calculated with different algorithms for the strain and stress path 7 of Table 3.1, graphically represented in Fig. 3.8.

Iso-error maps have been plotted to display the error trend of the two algorithms in the stress-space for a set of different strain increments, chosen with the condition that the trial elastic solutions σ^{trial} lie respectively in the meridian (denoted as $\mathbf{t} - \mathbf{n}$ in Fig. 3.9 on the left) and deviatoric (denoted as $\mathbf{m} - \mathbf{n}$ in Fig. 3.9 on

		Plastic strain			Error %
		ϵ_1^p	ϵ_2^p	ϵ_3^p	
Test 7	Centre of mass	$7.460 \cdot 10^{-5}$	$1.156 \cdot 10^{-5}$	$1.667 \cdot 10^{-5}$	6.64
	Return mapping	$7.888 \cdot 10^{-5}$	$4.924 \cdot 10^{-4}$	$1.075 \cdot 10^{-5}$	5.92
	Exact	$7.686 \cdot 10^{-5}$	$8.082 \cdot 10^{-6}$	$1.352 \cdot 10^{-5}$	

Table 3.4: Plastic strain at the end of the finite step calculated with different algorithms for the strain and stress path 7 of Table 3.1, graphically represented in Fig. 3.8.

the right) planes.

The iso-error maps plotting ranges have been chosen as follows:

$$0 \leq \frac{\Delta\sigma_n^{\text{trial}}}{|\sigma_y|} \leq 0.2, \quad -0.2 \leq \frac{\Delta\sigma_t^{\text{trial}}}{|\sigma_y|} \leq 0.2, \quad -0.2 \leq \frac{\Delta\sigma_m^{\text{trial}}}{|\sigma_y|} \leq 0.2. \quad (3.26)$$

where σ_y is the considered stress at yielding

$$\Delta\sigma^{\text{trial}} = \Delta\sigma_t^{\text{trial}}\mathbf{t} + \Delta\sigma_n^{\text{trial}}\mathbf{n} + \Delta\sigma_m^{\text{trial}}\mathbf{m}. \quad (3.27)$$

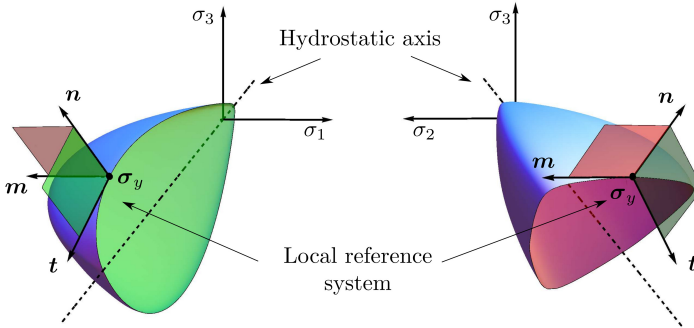


Figure 3.9: Sections of the yield surface and local reference system employed for the construction of the iso-error maps.

The iso-error maps are reported in Fig. 3.10–3.13, assuming as yield stresses σ_y those corresponding to the tests 3, 4, 5, and 6 of Tab. 3.1, graphically represented in Fig. 3.8.

It can be noted from Figs. 3.10 and 3.12 (bottom, left) that the centre-of-mass algorithm has a low accuracy when the yield

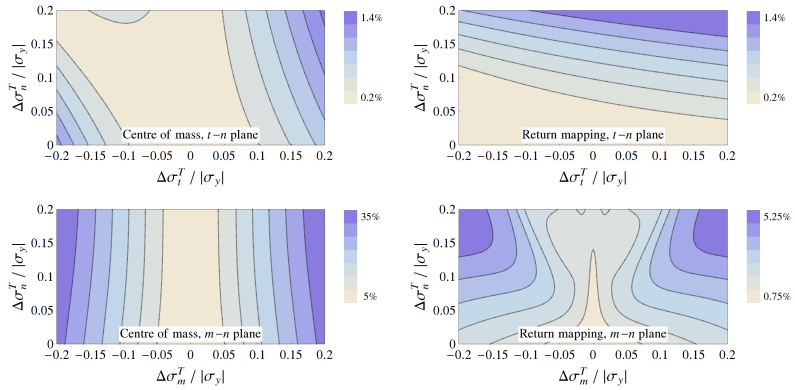


Figure 3.10: Iso-error maps for Test 3 (see Tab. 3.1 and Fig. 3.8).

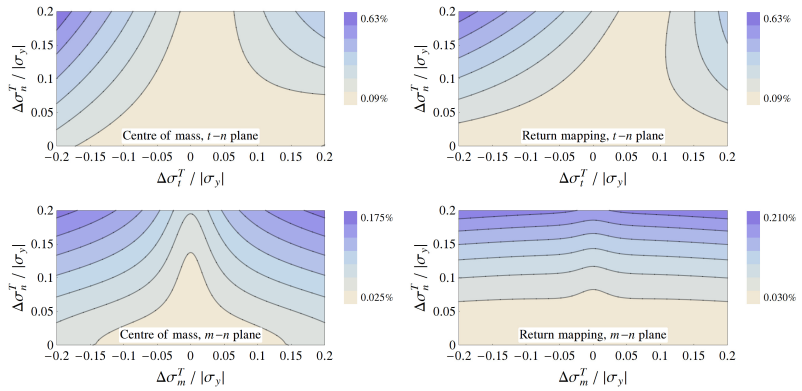


Figure 3.11: Iso-error maps for Test 4 (see Tab. 3.1 and Fig. 3.8).

stress σ_y lies near the corner of the deviatoric section (see Fig. 3.8, central part, tests 3 and 5) and the stress increment is not radial. On the other hand, the accuracy is high in both $t - n$ and $m - n$ planes, when the yield stress σ_y lies near the flat parts of this section (see Fig. 3.8, central part, tests 4 and 6), as shown in Figs. 3.11 and 3.13.

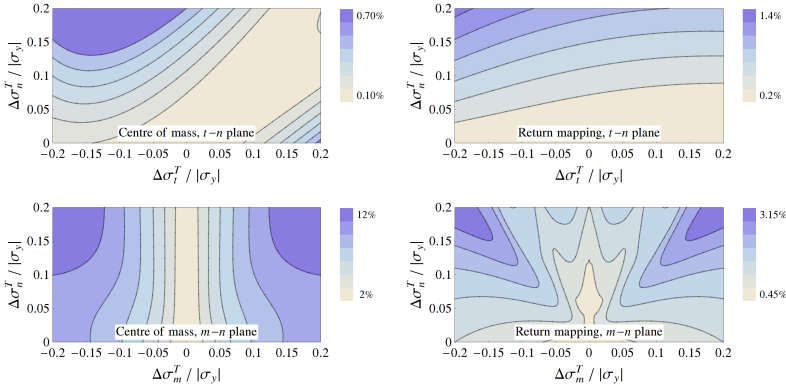


Figure 3.12: Iso-error maps for Test 5 (see Tab. 3.1 and Fig. 3.8).

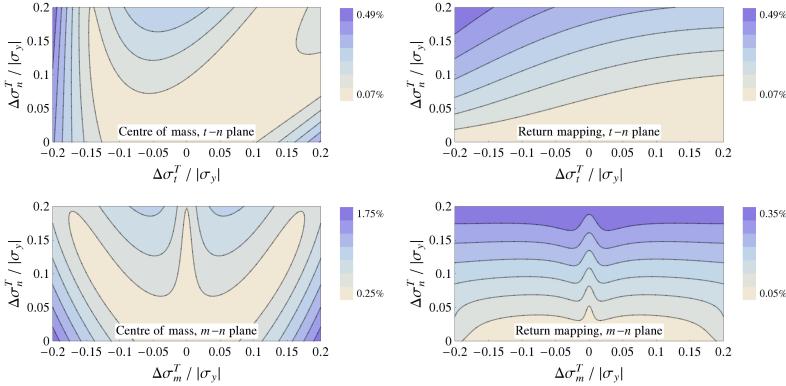


Figure 3.13: Iso-error maps for Test 6 (see Tab. 3.1 and Fig. 3.8).

3.3.2 Robustness improvement with implicit BP yield function

Tests performed on simple numerical models with limited amount of finite elements are often not representative of the stability of a computational implementation. More complex systems, possibly involving non-linearities of different nature (e.g. contact interaction), should be investigated properly to ensure the robustness of the selected integration algorithm for elastoplasticity.

To this end, the computational performance of the cut-off-substepping return algorithm (see Sec. 3.2.2) and the return mapping algorithm combined with the implicit definition of the BP yield function (see Sec. 3.2.3) have been tested on large thermo-

mechanical FE models. Since the final goal is the use of the coded UMAT subroutines in the industrial context, this step is fundamental to evaluate possible differences between the implementations.

While a good number of analyses yield to equivalent results, the numerical simulation of the bending test on refractory steel stoppers shows important differences if different integration algorithms are employed. In this simulation, that is described in detail in Sec. 6.5.1, the flexural strength of a cylindrical refractory device having the middle part heated to 1000 °C is investigated.

As already mentioned at the beginning of this Section, the tests presented here do not analyze the agreement between experimental and numerical results (see Sec. 6.5.1 for this). Instead, we aim to compare convergence rate and robustness of the two investigated integration algorithms.

For this reason, the analysis has been set up in such a way that softening effects or premature termination of the analysis due to failure criteria (see Secs. 6.3 and 6.2) can not occur. Furthermore, the imposed load is much higher than in the real experiment, so that significant inelastic deformations are generated.

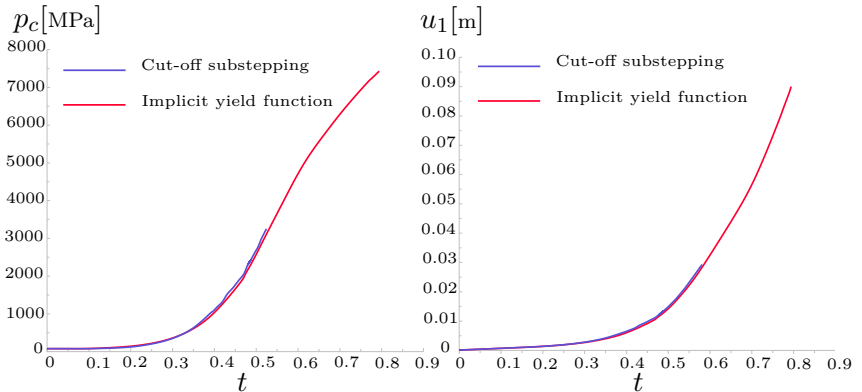


Figure 3.14: Comparison of ‘cut-off-substepping’ and return mapping with implicit defined BP yield function: isotropic strength p_c and pushing head displacements u_1 in the numerical simulation of bending test on refractory steel flow stopper. The analysis with the ‘cut-off-substepping’ algorithm crashes before the end.

Figure 3.14 shows the isotropic strength p_c of the refractory material in the most deformed element of the mesh and the displacement corresponding to the pushing head with both numerical methods. While at the beginning of the analysis the results are coincident, the simulation using the implementation of the cutoff-substepping return algorithm stops considerably before the end,

being unable to achieve convergence.

In the real test, the break load is much smaller than the force corresponding to the crash of the simulation. Therefore, both algorithms are able to entirely simulate this particular experiment. As long as valid results are returned by both procedures, only negligible differences in terms of convergence rate have been observed. Although the causes related to the lower stability of the cut-off-substepping algorithm are still not completely clear, the test highlights the better robustness of the return mapping procedure combined with implicit definition of the BP yield function. For the cited reasons, the last procedure has been preferred in the implementation of the constitutive models presented in the next Chapters.

3.4 Comparison with semi-analytical solutions of plastic benchmark problems

Numerical results obtained by employing the proposed algorithms have been compared with semi-analytical solutions of a simple compaction problem and a deformation of a green body. In particular, in Section 3.4.1, the forming of a thick perfectly-plastic layer of ceramic powder is considered, pressed against a rigid spherical cup, see Fig. 3.15a. Moreover, a thick spherical shell of a green body is considered in Section 3.4.2, subjected to an internal uniform pressure with a traction-free external boundary and expanded until collapse, corresponding to complete plasticization, see Fig. 3.15b. Due to the spherical symmetry of both the problems, it is possible in both cases to obtain accurate semi-analytical solutions for the stress field by direct numerical integration of the equilibrium equations.

These benchmark problems, differing only in the boundary conditions, are used to check the accuracy and efficiency of the proposed algorithms. They represent only model problem simulations of industrial processes and cannot be considered fully realistic, since hardening (and therefore the evolution of the yield surface) is neglected, so that the increase in cohesion is not taken into account.

The problem of the expansion of a thick spherical shell is interesting in itself, due to the applications in geotechnics, and it has been previously solved under a number of hypotheses (Hill, 1950; Bigoni and Laudiero, 1989; Cohen et al. 2009; Rapoport et al.

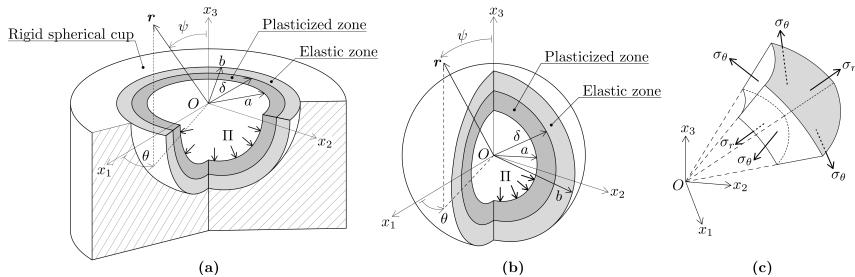


Figure 3.15: Geometry for the compaction of a thick perfectly-plastic layer of ceramic powder against a rigid cup (a) and for the expansion of a thick perfectly-plastic shell under internal pressure (b). In both cases, the boundary of the plasticized zone is represented by δ which moves from $r = a$ to $r = b$ at increasing internal pressure Π . The reference system and stress components are shown in part (c).

2011; Volokh, 2011), although never with the BP yield function. The problem of compaction of a layer of powder against a rigid cup was previously not addressed in analytically.

For both problems, the inner and outer radii of the shell are denoted with a and b respectively, while the internal pressure is Π , which is assumed to increase from zero to the maximum value corresponding to the full plasticization of the shell. Since the geometry shows radial symmetry, we assume a spherical coordinate system. The solution is known in the case of perfect plasticity with the Tresca yield criterion (Hill, 1950), so that our objective is to generalize the solution to the BP yield criterion.

Due to the spherical symmetry, the stress and deformation depend only on the radius r . The non-vanishing deformation radial, azimuthal, and polar components are respectively

$$\varepsilon_r = \frac{du}{dr}, \quad \varepsilon_\theta = \varepsilon_\phi = \frac{u}{r}, \quad (3.28)$$

where u is the radial displacement. The compatibility equation is

$$\varepsilon_r = \frac{d}{dr}(r\varepsilon_\theta), \quad (3.29)$$

while the equilibrium equation in spherical coordinates is

$$\frac{d\sigma_r}{dr} + \frac{2}{r}(\sigma_r - \sigma_\theta) = 0, \quad (3.30)$$

to be complemented by the boundary conditions.

The elastic constitutive equations are

$$\varepsilon_r = E^{-1}(\sigma_r - 2\nu\sigma_\theta), \quad \varepsilon_\theta = E^{-1}[(1 - \nu)\sigma_\theta - \nu\sigma_r], \quad (3.31)$$

where E is the elastic Young modulus and ν the Poisson's ratio. The Tresca yield criterion coincides (under the current assumptions) with the von Mises criterion, which can be written as

$$|\sigma_r - \sigma_\theta| - \sigma_0 = 0, \quad (3.32)$$

where σ_0 is the uniaxial yield stress, while the BP yield criterion (2.55) writes now in the following form

$$F(\boldsymbol{\sigma}) = f\left(\frac{\sigma_r + 2\sigma_\theta}{3}\right) + \frac{|\sigma_r - \sigma_\theta|}{g\left(\frac{\pi}{3}\right)} = 0. \quad (3.33)$$

The elastic solution. Using equations (3.29), (3.30) and (3.31) we obtain

$$\frac{1 - \nu}{2} \frac{d}{dr} (\sigma_r + 2\sigma_\theta) = 0. \quad (3.34)$$

This equation together with Eq. (3.30) forms a system of ODEs, which can be solved exactly and the solution is given by

$$\sigma_r(r) = \frac{C_1}{3} + \frac{C_2}{r^3}, \quad \sigma_\theta(r) = \frac{C_1}{3} - \frac{C_2}{2r^3}, \quad (3.35)$$

where C_1 and C_2 are constants to be defined through the boundary conditions. The associated deformation and displacement fields are obtained from (3.31) and (3.28) and read

$$\varepsilon_r(r) = \frac{1}{E} \left[(1 - 2\nu) \frac{C_1}{3} + (1 + \nu) \frac{C_2}{r^3} \right], \quad (3.36)$$

$$\varepsilon_\theta(r) = \frac{1}{E} \left[(1 - 2\nu) \frac{C_1}{3} - (1 + \nu) \frac{C_2}{2r^3} \right], \quad (3.37)$$

$$u(r) = \frac{1}{E} \left[(1 - 2\nu) \frac{C_1}{3} r - (1 + \nu) \frac{C_2}{2r^2} \right], \quad (3.38)$$

3.4.1 Compaction of a thick layer of perfectly-plastic material obeying the BP yield condition against a rigid spherical cup

For the compaction problem of a thick layer against a rigid spherical cup, Fig. 3.15a, the boundary conditions write as follows

$$\sigma_r|_{r=a} = -\Pi, \quad u|_{r=b} = 0, \quad (3.39)$$

where Π is the internal pressure.

The material parameters defining the shape of the BP yield surface have been chosen to be representative of alumina powder (Piccolroaz et al., 2006), namely

$$\begin{aligned} M = 1.1, \quad m = 2, \quad \alpha = 0.1, \quad \beta = 0.19, \\ \gamma = 0.9, \quad p_c = 40 \text{ MPa}, \quad c = 1.5 \text{ MPa}. \end{aligned}$$

Note that, since hardening and increasing of cohesion are neglected, we assume an initial state corresponding to an intermediate stage of a densification process.

The elastic solution

Initially the problem is purely elastic, which occurs when the internal pressure is sufficiently small, say, $\Pi \leq \Pi_y$, where Π_y is defined as the inner pressure producing the initiation of yielding at the inner radius of the shell.

The solution (3.35)–(3.38) together with boundary conditions (3.39), provides the following stress field within the thick spherical layer, $a \leq r \leq b$,

$$\sigma_r^e(\Pi, r) = -\frac{a^3(1+\nu)\Pi}{a^3(1+\nu) + 2b^3(1-2\nu)} - \frac{2a^3b^3(1-2\nu)\Pi}{a^3(1+\nu) + 2b^3(1-2\nu)} \frac{1}{r^3}, \quad (3.40)$$

$$\sigma_\theta^e(\Pi, r) = -\frac{a^3(1+\nu)\Pi}{a^3(1+\nu) + 2b^3(1-2\nu)} + \frac{a^3b^3(1-2\nu)\Pi}{a^3(1+\nu) + 2b^3(1-2\nu)} \frac{1}{r^3}. \quad (3.41)$$

For the von Mises yield criterion, the critical yield pressure Π_y is represented by the stress state satisfying

$$|\sigma_r^e - \sigma_\theta^e| = \sigma_0, \quad (3.42)$$

and can be evaluated as

$$\Pi_y = \frac{\sigma_0}{3} \left[2 + \frac{1+\nu}{1-2\nu} \left(\frac{a}{b} \right)^3 \right]. \quad (3.43)$$

In the following calculations $\nu = 0.26$ has been assumed. For the BP yield criterion, the critical yield pressure Π_y corresponds to a stress state satisfying

$$\max_{a \leq r \leq b} F(\sigma_r^e(\Pi_y, r), \sigma_\theta^e(\Pi_y, r)) = 0, \quad (3.44)$$

so that Π_y can be evaluated as the numerical solution of the above equation and it can be numerically shown that the plasticization starts from the inner surface of the layer, $r = a$.

The elasto-plastic solution

The elasto-plastic solution holds for an internal pressure $\Pi > \Pi_y$, which implies both elastic and plastic deformation of the layer. The plastic flow starts from the inner surface of the layer and propagates within a spherical region with inner radius a and outer δ and moving toward b . The remaining part of the layer, namely, for $\delta \leq r \leq b$, behaves as an elastic layer with inner radius δ and outer b , subject to an internal pressure Π_δ at the interface with the plasticized zone.

Assuming that the yield pressure at the interface $r = \delta$ is Π_δ , a generic yield criterion writes as

$$F(\sigma_r^e(\Pi_\delta, \delta), \sigma_\theta^e(\Pi_\delta, \delta)) = 0, \quad (3.45)$$

which provides a relation between δ and Π_δ . For example, the pressure at the interface for the von Mises criterion can be obtained from Eq. (3.43) imposing $a = \delta$ as

$$\Pi_\delta = \frac{\sigma_0}{3} \left[2 + \frac{1 + \nu}{1 - 2\nu} \left(\frac{\delta}{b} \right)^3 \right]. \quad (3.46)$$

whereas for the BP criterion the pressure Π_δ has to be evaluated numerically.

The solution for the elastic zone ($\delta \leq r \leq b$) can be obtained from eqs. (3.40) and (3.41) where a and Π are replaced, respectively, by δ and Π_δ which are given by (3.45), so that the stresses become

$$\sigma_r^{\text{ep}}(r) = -\frac{\delta^3(1 + \nu)\Pi_\delta}{\delta^3(1 + \nu) + 2b^3(1 - 2\nu)} - \frac{2\delta^3b^3(1 - 2\nu)\Pi_\delta}{\delta^3(1 + \nu) + 2b^3(1 - 2\nu)} \frac{1}{r^3}, \quad (3.47)$$

$$\sigma_{\theta}^{\text{ep}}(r) = -\frac{\delta^3(1+\nu)\Pi_{\delta}}{\delta^3(1+\nu) + 2b^3(1-2\nu)} + \frac{\delta^3b^3(1-2\nu)\Pi_{\delta}}{\delta^3(1+\nu) + 2b^3(1-2\nu)} \frac{1}{r^3}, \quad (3.48)$$

Hence the elastic part of the solution is known as the relation between the radius δ and the pressure Π_{δ} is known.

The solution for the plasticized zone ($a \leq r \leq \delta$) is obtained from the algebraic-differential system composed by the equilibrium equations (3.30), the boundary conditions (3.39), and the yield condition (3.32) or (3.33) (depending on the criterion assumed). This system writes as

$$\begin{cases} \frac{d\sigma_r}{dr} + \frac{2}{r}(\sigma_r - \sigma_{\theta}) = 0, \\ F(\sigma_r(r), \sigma_{\theta}(r)) = 0, \\ \sigma_r|_{r=a} = -\Pi, \\ \sigma_r|_{r=\delta} = -\Pi_{\delta}, \end{cases} \quad (3.49)$$

which has been solved analytically for von Mises yield and numerically for the BP yield function. In particular, the system (3.49) admits for von Mises the following solution

$$\sigma_r^{\text{ep}}(r) = -\frac{\sigma_0}{3} \left[2 + \frac{1+\nu}{1-2\nu} \left(\frac{\delta}{b}\right)^3 + 6 \log\left(\frac{\delta}{r}\right) \right], \quad (3.50)$$

$$\sigma_{\theta}^{\text{ep}}(r) = -\frac{\sigma_0}{3} \left[-1 + \frac{1+\nu}{1-2\nu} \left(\frac{\delta}{b}\right)^3 + 6 \log\left(\frac{\delta}{r}\right) \right],$$

and the relation between δ and the internal pressure Π writes as

$$\Pi = \frac{\sigma_0}{3} \left[2 + \frac{1+\nu}{1-2\nu} \left(\frac{\delta}{b}\right)^3 + 6 \log\left(\frac{\delta}{a}\right) \right], \quad (3.51)$$

which is a nonlinear relation. Once a fixed value of the radius δ , representing the amplitude of the plasticized zone, is chosen, it is possible to obtain the internal pressure Π and the stresses in every part of the layer, namely for $a \leq r \leq b$.

Results in terms of radial and polar stress components and the two stress invariants p and q are reported in Fig. 3.16 as functions of the through-thickness radius (divided by the mean radius $r_m =$

$(a+b)/2$ of the spherical layer), together with the numerical results obtained with the two proposed algorithms. Three different plastic boundaries δ have been considered (corresponding to the 20%, 40% and 60 % of the thickness) for both von Mises and the BP yield criterion.

Results presented in the figure fully support the validity of the proposed numerical algorithms, which have given coincident results, superimposed on the semi-analytical solution.

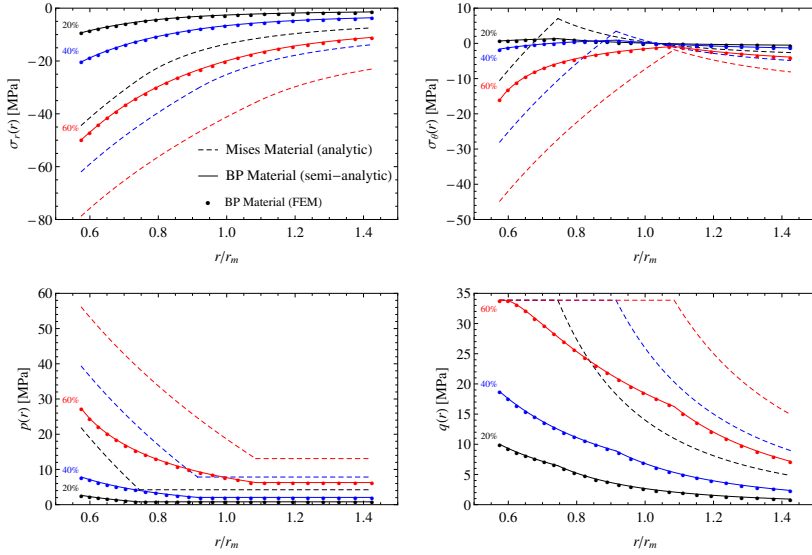


Figure 3.16: Compaction of a perfectly-plastic thick layer, obeying von Mises and BP yield conditions, against a rigid spherical cup, representative of a ceramic powder. Upper part: radial (left) and polar (right) stress components as functions of the dimensionless radial position. Lower part: mean stress p (left) and deviatoric invariant q (right) as functions of the dimensionless radial position. Note that for the von Mises criterion $\sigma_0 = 33.86$ MPa has been chosen, so that the von Mises cylinder is circumscribed around the BP surface in the stress space.

3.4.2 Expansion of a perfectly plastic thick shell obeying the BP yield condition

For the problem of expansion of a thick spherical shell subjected to an internal uniform pressure, Fig. 3.15b, the boundary conditions are as follows

$$\sigma_r|_{r=a} = -\Pi, \quad \sigma_r|_{r=b} = 0, \quad (3.52)$$

where Π is the internal pressure and the outer boundary is assumed traction-free. The material parameters defining the shape of the BP yield surface have been chosen to be representative of a partially densified ceramic powder, namely

$$M = 1.33, \quad m = 2, \quad \alpha = 1, \quad \beta = 1, \\ \gamma = 0, \quad p_c = 150 \text{ MPa}, \quad c = 150 \text{ MPa}.$$

The solution of this problem can be obtained with the same method as the one described in Sec. 3.4.1, since only the boundary conditions are different.

The elastic solution, valid until the internal pressure is sufficiently small, $\Pi \leq \Pi_y$, is given by

$$\sigma_r^e(r) = \frac{\Pi}{\left(\frac{b}{a}\right)^3 - 1} \left[1 - \left(\frac{b}{r}\right)^3 \right], \quad \sigma_\theta^e(r) = \frac{\Pi}{\left(\frac{b}{a}\right)^3 - 1} \left[1 + \frac{1}{2} \left(\frac{b}{r}\right)^3 \right]. \quad (3.53)$$

For the von Mises yield criterion, $|\sigma_r^e - \sigma_\theta^e| = \sigma_0$, the critical yield pressure Π_y is obtained as

$$\Pi_y = \frac{2}{3} \sigma_0 \left[1 - \left(\frac{a}{b}\right)^3 \right], \quad (3.54)$$

whereas for the BP yield criterion, the critical yield pressure Π_y is obtained by solving Eq. (3.44) and it can be numerically proven that the plasticization starts from the inner surface of the shell.

The elasto-plastic solution holds for an internal pressure $\Pi > \Pi_y$, which implies both elastic and plastic deformation of the shell. The plastic flow starts from the inner surface of the shell and propagates within a spherical region with inner radius a and outer δ and moving toward b . The remaining part of the shell, namely, for $\delta \leq r \leq b$, behaves as an elastic shell with inner radius δ and outer b , subject to an internal pressure Π_δ at the interface with the plasticized zone.

The relation between δ and Π_δ is obtained by solving Eq. (3.45). For the von Mises criterion Π_δ is obtained as

$$\Pi_\delta = \frac{2}{3}\sigma_0 \left[1 - \left(\frac{\delta}{b} \right)^3 \right], \quad (3.55)$$

whereas for the BP criterion the pressure Π_δ has to be evaluated numerically.

The solution for the elastic zone, $\delta \leq r \leq b$, is given by

$$\begin{aligned} \sigma_r^{\text{ep}}(r) &= \frac{\Pi_\delta}{\left(\frac{b}{\delta}\right)^3 - 1} \left[1 - \left(\frac{b}{r}\right)^3 \right], \\ \sigma_\theta^{\text{ep}}(r) &= \frac{\Pi_\delta}{\left(\frac{b}{\delta}\right)^3 - 1} \left[1 + \frac{1}{2} \left(\frac{b}{r}\right)^3 \right]. \end{aligned} \quad (3.56)$$

The solution for the plasticized zone, $a \leq r \leq \delta$, is obtained from the algebraic-differential system (3.49). This system has a solution with closed form for the simple case of von Mises yield criterion; in this case the stresses take the form

$$\begin{aligned} \sigma_r &= -\frac{2}{3}\sigma_y \left[1 - \left(\frac{\delta}{b}\right)^3 + \ln \left(\frac{\delta}{r}\right)^3 \right], \\ \sigma_\theta &= \frac{1}{3}\sigma_y \left[1 + 2 \left(\frac{\delta}{b}\right)^3 - 2 \ln \left(\frac{\delta}{r}\right)^3 \right], \end{aligned} \quad (3.57)$$

and the relation between δ and the internal pressure Π writes as

$$\Pi = \frac{2}{3}\sigma_y \left[1 - \left(\frac{\delta}{b}\right)^3 + \ln \left(\frac{\delta}{a}\right)^3 \right]. \quad (3.58)$$

Once a fixed value of the radius δ representing the amplitude of the plasticized zone is chosen, it is possible to obtain the internal pressure Π and the stresses in every part of the shell, namely for $a \leq r \leq b$.

Results in terms of radial and polar stress components and the two stress invariants p and q are reported in Fig. 3.17 as functions of the through-thickness radius (divided by the mean radius $r_m = (a + b)/2$ of the thick shell), together with the numerical results obtained with the two proposed algorithms. Three different plastic boundaries δ have been considered (corresponding to the 28%, 55% and 86% of the thickness) for both von Mises and the

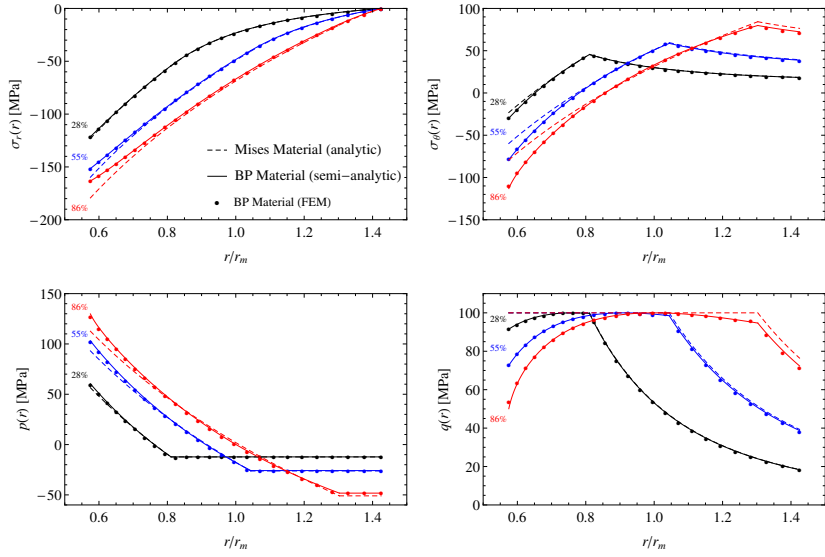


Figure 3.17: Expansion of a perfectly-plastic thick spherical shell, obeying von Mises and BP yield conditions, representative of a green body. Upper part: radial (left) and polar (right) stress components as functions of the dimensionless radial position. Lower part: mean stress p (left) and deviatoric invariant q (right) as functions of the dimensionless radial position. Note that for the von Mises criterion $\sigma_0 = 100$ MPa has been chosen, so that the von Mises cylinder is circumscribed around the BP surface in the stress space.

BP yield criterion. Again the two proposed algorithms have given coincident values, superimposed with the semi-analytical solution, thus confirming once more the validity of the presented numerical approaches.

3.5 Comparison with semi-analytical solutions of thermoplastic benchmark problems

The numerical implementations of the proposed algorithms have been validated by comparison with semi-analytical solutions of two simple benchmark problems involving a spherical geometry. In particular, in Sec. 3.5.1, the hot pressing of a thick perfectly plastic layer of a ceramic powder against a spherical cup is addressed. Moreover, in Sec. 3.5.2, the problem of thermal heating and simultaneous mechanical expansion of a thick spherical shell of a green body is analyzed.

For these problems, the steady-state solution is obtained both using a semi-analytical approach and using the finite element implementation.

In the steady-state solution, the heat conduction problem decouples from the mechanical problem and is solved in closed form. Denoting the inner and outer radii of the shell by a and b , respectively, and assuming that the temperature is increased at the inner surface, the temperature field is the solution of the following differential problem:

$$\frac{\partial^2 T}{\partial r^2} + \frac{2}{r} \frac{\partial T}{\partial r} = 0, \quad \forall r \in (a, b), \quad (3.59)$$

$$T(a) = \Theta, \quad (3.60)$$

$$T(b) = 0, \quad (3.61)$$

where Θ denotes the increase of temperature, with respect to the reference temperature, at the inner surface.

The solution is given by

$$T(r) = \frac{a\Theta}{b-a} \left(\frac{b}{r} - 1 \right). \quad (3.62)$$

For both problems, the internal pressure, denoted by Π , is assumed to increase from zero to the maximum value corresponding to the full plasticization of the shell. In a spherical coordinate system (r, θ, ϕ) , the stress and deformation depend only on the radius r , because of the spherical symmetry. The non-vanishing deformations are:

$$\varepsilon_r = \frac{du}{dr}, \quad \varepsilon_\theta = \varepsilon_\phi = \frac{u}{r}, \quad (3.63)$$

where u is the radial displacement. The compatibility equation is

$$\varepsilon_r = \frac{d}{dr}(r\varepsilon_\theta), \quad (3.64)$$

while the equilibrium equation is

$$\frac{d\sigma_r}{dr} + \frac{2}{r}(\sigma_r - \sigma_\theta) = 0. \quad (3.65)$$

The elastic constitutive equations are

$$\varepsilon_r^e = E^{-1}(\sigma_r - 2\nu\sigma_\theta), \quad \varepsilon_\theta^e = E^{-1}((1 - \nu)\sigma_\theta - \nu\sigma_r), \quad (3.66)$$

where E is the Young modulus and ν the Poisson's ratio. The deformations admit the additive splitting

$$\varepsilon_r = \varepsilon_r^e + \varepsilon_r^T + \varepsilon_r^p = \varepsilon_r^e + \alpha_T T + \varepsilon_r^p, \quad (3.67)$$

$$\varepsilon_\theta = \varepsilon_\theta^e + \varepsilon_\theta^T + \varepsilon_\theta^p = \varepsilon_\theta^e + \alpha_T T + \varepsilon_\theta^p, \quad (3.68)$$

where α_T is the coefficient of thermal expansion.

The Tresca yield criterion coincides (under the current assumptions) with the Von Mises criterion, which takes the form

$$|\sigma_r - \sigma_\theta| - \sigma_Y(T) = 0, \quad (3.69)$$

where

$$\sigma_Y(T) = \sigma_Y^0 - \frac{\sigma_Y^0 - \sigma_Y^f}{T_f} T, \quad (3.70)$$

is a function describing linear thermal softening in the temperature range $T \in (0, T_f)$.

The BP yield criterion with thermal softening assumes the following form

$$F(\sigma_r, \sigma_\theta, T) = f\left(\frac{\sigma_r + 2\sigma_\theta}{3}, p_c(T), c(T)\right) + \frac{|\sigma_r - \sigma_\theta|}{g(\pi/3)} = 0, \quad (3.71)$$

where

$$p_c(T) = p_{c0} - \frac{p_{c0} - p_{cf}}{T_f} T, \quad (3.72)$$

$$c(T) = \Omega p_c(T), \quad (3.73)$$

are functions describing linear thermal softening, with a constant ratio $c/p_c = \Omega$, so to describe an homothetic contraction of the yield surface with temperature (see Figs. 3.18 and 3.22).

The elastic solution: Using Eqs. (3.64)–(3.68) with $\varepsilon_r^p = \varepsilon_\theta^p = 0$, the following equation is derived

$$\frac{1 - \nu}{2} \frac{d}{dr} (\sigma_r + 2\sigma_\theta) + \alpha_T E \frac{dT}{dr} = 0, \quad (3.74)$$

where $T = T(r)$ is given by (3.62). This equation together with the equilibrium equation (3.65) forms a system of ODEs, which can be solved exactly and the solution is given by

$$\sigma_r(r) = \frac{C_1}{3} + \frac{C_2}{r^3} - \frac{\alpha_T E}{1 - \nu} \frac{ab\Theta}{(b - a)r}, \quad (3.75)$$

$$\sigma_\theta(r) = \frac{C_1}{3} - \frac{C_2}{2r^3} - \frac{\alpha_T E}{2(1 - \nu)} \frac{ab\Theta}{(b - a)r}, \quad (3.76)$$

where C_1 and C_2 are constants to be defined through the boundary conditions. The associated deformation and displacement fields are obtained from the constitutive relations (3.66) and the compatibility conditions (3.63), respectively,

$$\begin{aligned} \varepsilon_r(r) &= \frac{1}{E} \left[(1 - 2\nu) \frac{C_1}{3} + (1 + \nu) \frac{C_2}{r^3} \right] - \alpha_T \frac{a\Theta}{b - a}, \\ \varepsilon_\theta(r) &= \frac{1}{E} \left[(1 - 2\nu) \frac{C_1}{3} - (1 + \nu) \frac{C_2}{2r^3} \right] - \\ &\quad \alpha_T \frac{a\Theta [2(1 - \nu)r + b(1 + \nu)]}{2(1 - \nu)(b - a)r}, \end{aligned} \quad (3.77)$$

$$\begin{aligned} u(r) &= \frac{1}{E} \left[(1 - 2\nu) \frac{C_1}{3} r - (1 + \nu) \frac{C_2}{2r^2} \right] - \\ &\quad \alpha_T \frac{a\Theta [2(1 - \nu)r + b(1 + \nu)]}{2(1 - \nu)(b - a)}. \end{aligned}$$

3.5.1 Hot pressing of a thick layer of perfectly plastic ceramic powder against a rigid spherical mould

For the hot pressing of a thick layer of perfectly plastic ceramic powder against a rigid spherical mould, the boundary conditions are as follows

$$\sigma_r(r = a) = -II, \quad u(r = b) = 0, \quad (3.78)$$

where II is the internal pressure. The parameters defining the shape of the BP yield surface are those representative of alumina powder [14]

$$M = 1.1, \quad m = 2, \quad \alpha = 0.1, \quad \beta = 0.19, \quad \gamma = 0.9. \quad (3.79)$$

The parameters describing thermal softening have been chosen to be

$$p_{c0} = 40 \text{ MPa}, \quad p_{cf} = 20 \text{ MPa}, \quad T_f = 1000, \quad (3.80)$$

whereas the ratio between the cohesion c and the consolidation pressure p_c has been fixed to be $\Omega = 0.0375$. The increase of temperature at the inner surface has been chosen to be $\Theta = 380^\circ\text{C}$.

The traces of the BP yield surface in the $(\sigma_r, \sigma_\theta)$ -plane for fourth values of temperature, namely $T = 0, 190, 285$, and 380°C , are shown in Fig. 3.18 (solid lines), together with the traces of the Von Mises cylinder circumscribed to the BP surface (dashed lines).

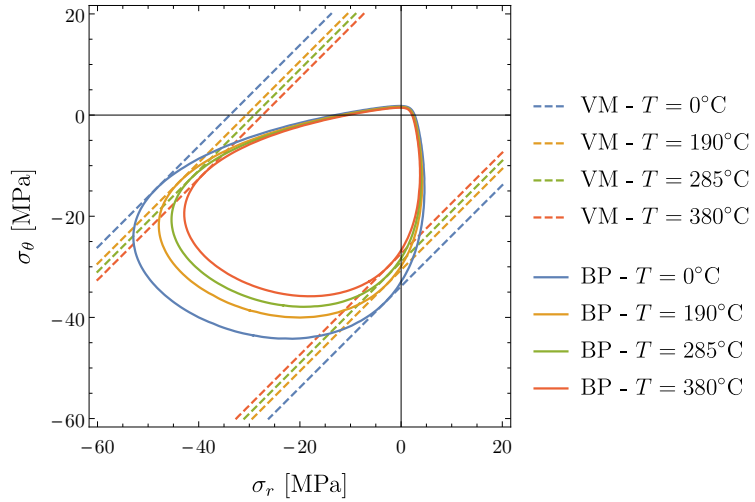


Figure 3.18: Traces of the BP yield surface in the $(\sigma_r, \sigma_\theta)$ -plane for fourth values of temperature $T = 0, 190, 285$, and 380°C (solid lines) and corresponding traces of the circumscribed Von Mises cylinder (dashed lines). Material parameters have been chosen to be representative of alumina powder.

The elastic solution

Initially the problem is purely elastic, which occurs when the internal pressure Π is smaller than Π_Y , defined as the pressure producing the initiation of yielding at the inner surface of the shell. The solution (3.75)–(3.76) together with the boundary conditions (3.78) provides the following stress field within the thick spherical

layer, $a \leq r \leq b$,

$$\begin{aligned} \sigma_r^E(\Pi, \Theta, r) = & \frac{abE\alpha_T\Theta}{a(1-\nu) - b(1-\nu)} \frac{1}{r} - \frac{2a^3b^3(1-2\nu)\Pi}{a^3(1+\nu) + 2b^3(1-2\nu)} \frac{1}{r^3} - \\ & \frac{a^3(1+\nu)\Pi}{a^3(1+\nu) + 2b^3(1-2\nu)} + \frac{a^3b^3E(2b(1-2\nu) - a(1-3\nu))\alpha_T\Theta}{(1-\nu)(b-a)(a^3(1+\nu) + 2b^3(1-2\nu))} \frac{1}{r^3} + \\ & \frac{abE(a^2(1+\nu) + b^2(1-3\nu))\alpha_T\Theta}{(1-\nu)(b-a)(a^3(1+\nu) + 2b^3(1-2\nu))}, \quad (3.81) \end{aligned}$$

$$\begin{aligned} \sigma_\theta^E(\Pi, \Theta, r) = & -\frac{a^3(1+\nu)\Pi}{a^3(1+\nu) + 2b^3(1-2\nu)} + \frac{a^3b^3(1-2\nu)\Pi}{a^3(1+\nu) + 2b^3(1-2\nu)} \frac{1}{r^3} + \\ & \frac{abE(a^2(1+\nu) + b^2(1-3\nu))\alpha_T\Theta}{(1-\nu)(b-a)(a^3(1+\nu) + 2b^3(1-2\nu))} + \frac{abE\alpha_T\Theta}{a(1-\nu) - b(1-\nu)} \frac{1}{2r} - \\ & \frac{a^3b^3E(2b(1-2\nu) - a(1-3\nu))\alpha_T\Theta}{(1-\nu)(b-a)(a^3(1+\nu) + 2b^3(1-2\nu))} \frac{1}{2r^3}. \quad (3.82) \end{aligned}$$

The corresponding strains are given by

$$\begin{aligned} \varepsilon_r^E(\Pi, \Theta, r) = & \frac{a(1+\nu)(b(1-2\nu)(a^2 - b^2) - a^3(1-\nu))\alpha_T\Theta}{(1-\nu)(b-a)(a^3(1+\nu) + 2b^3(1-2\nu))} - \\ & \frac{a^3(1+\nu)(1-2\nu)\Pi}{E(a^3(1+\nu) + 2b^3(1-2\nu))} - \frac{2a^3b^3(1+\nu)(1-2\nu)\Pi}{E(a^3(1+\nu) + 2b^3(1-2\nu))} \frac{1}{r^3} - \\ & \frac{a^3b^3(1+\nu)(a(1-3\nu) - 2b(1-2\nu))\alpha_T\Theta}{(1-\nu)(b-a)(a^3(1+\nu) + 2b^3(1-2\nu))} \frac{1}{r^3}. \quad (3.83) \end{aligned}$$

$$\begin{aligned} \varepsilon_\theta^E(\Pi, \Theta, r) = & \frac{a^3b^3(1+\nu)(1-2\nu)\Pi}{E(a^3(1+\nu) + 2b^3(1-2\nu))} \frac{1}{r^3} \\ & - \frac{a^3(1+\nu)(1-2\nu)\Pi}{E(a^3(1+\nu) + 2b^3(1-2\nu))} + \frac{ab(1+\nu)\alpha_T\Theta}{2(1-\nu)(b-a)} \frac{1}{r} \\ & - \frac{a(1+\nu)(b(1-2\nu)(b^2 - a^2) + a^3(1-\nu))\alpha_T\Theta}{(1-\nu)(b-a)(a^3(1+\nu) + 2b^3(1-2\nu))} \\ & + \frac{a^3b^3(1+\nu)(a(1-3\nu) - 2b(1-2\nu))\alpha_T\Theta}{2(1-\nu)(b-a)(a^3(1+\nu) + 2b^3(1-2\nu))} \frac{1}{r^3}. \quad (3.84) \end{aligned}$$

For the Von Mises criterion, the internal pressure Π_Y producing the first yielding at $r = a$ is given by a stress state satisfying

$$|\sigma_r - \sigma_\theta| = \sigma_Y(T), \quad (3.85)$$

and can be evaluated as

$$\begin{aligned} \Pi_Y = \frac{\sigma_Y(\Theta)}{3} \left[2 + \frac{1+\nu}{1-2\nu} \left(\frac{a}{b} \right)^3 \right] + \\ \frac{\alpha_T \Theta E (a(a+b)(1+\nu) + 4b^2(1-2\nu))}{6b^2(1-\nu)(1-2\nu)}. \end{aligned} \quad (3.86)$$

For the BP yield criterion, the critical yield pressure Π_Y corresponds to a stress state satisfying

$$\max_{a \leq r \leq b} F(\sigma_r^E(\Pi_Y, \Theta, r), \sigma_\theta^E(\Pi_Y, \Theta, r), T(r)) = 0, \quad (3.87)$$

so that Π_Y can be evaluated numerically using for instance the Newton method.

The elasto-plastic solution

For an internal pressure Π exceeding the critical yield pressure Π_Y , $\Pi > \Pi_Y$, plastic deformations develop within the spherical shell starting from the inner surface. The plasticized zone forms an internal layer with inner radius a and outer radius δ . The external part of the shell, having inner radius δ and outer radius b , behaves as an elastic layer subject to an internal pressure Π_δ at the interface with the plasticized zone.

The relationship between the interface radius δ and the corresponding pressure Π_δ can be obtained by imposing the fulfillment of the yield conditions

$$F(\sigma_r^E(\Pi_\delta, \Theta_\delta, \delta), \sigma_\theta^E(\Pi_\delta, \Theta_\delta, \delta), \Theta_\delta) = 0, \quad (3.88)$$

where

$$\Theta_\delta = \frac{a\Theta}{b-a} \left(\frac{b}{\delta} - 1 \right) \quad (3.89)$$

is the temperature at $r = \delta$. For the Von Mises criterion the pressure at the interface Π_δ can be obtained analytically from (3.86) replacing a with δ and Θ with Θ_δ ,

$$\begin{aligned} \Pi_\delta = \frac{\sigma_Y(\Theta_\delta)}{3} \left[2 + \frac{1+\nu}{1-2\nu} \left(\frac{\delta}{b} \right)^3 \right] + \\ \frac{\alpha_T \Theta_\delta E (\delta(\delta+b)(1+\nu) + 4b^2(1-2\nu))}{6b^2(1-\nu)(1-2\nu)}. \end{aligned} \quad (3.90)$$

For the BP criterion the pressure Π_δ has to be evaluated numerically from Eq. (3.88).

The solution for the elastic zone, $\delta < r < b$, can be obtained from Eqs. (3.81)–(3.84) where a , Π and Θ are replaced, respectively, by δ , Π_δ and Θ_δ . Therefore the solution for the elastic part of the shell is known, as the relation between the interface radius δ and the corresponding pressure Π_δ is known.

The solution for the plasticized zone, $a < r < \delta$, is obtained from the algebraic-differential system composed by the equilibrium equation (3.65), the yield condition (3.70) or (3.71), depending on the criterion assumed, and the appropriate boundary conditions. This system writes as

$$\frac{d\sigma_r}{dr} + \frac{2}{r}(\sigma_r - \sigma_\theta) = 0, \quad (3.91)$$

$$F(\sigma_r(r), \sigma_\theta(r), T(r)) = 0, \quad (3.92)$$

$$\sigma_r(\delta) = -\Pi_\delta, \quad (3.93)$$

which can be solved analytically for the Von Mises criterion and numerically for the BP criterion. In particular, the system (3.91)–(3.93) admits for Von Mises the following solution

$$\begin{aligned} \sigma_r(r) = & -\Pi_\delta - 2\sigma_Y^0 \log\left(\frac{\delta}{r}\right) \\ & - 2\Theta_\delta \frac{\sigma_Y^0 - \sigma_Y^f}{T_f} \left[\frac{(r - \delta)b}{(b - \delta)r} + \frac{\delta}{b - \delta} \log\left(\frac{\delta}{r}\right) \right], \end{aligned} \quad (3.94)$$

$$\begin{aligned} \sigma_\theta(r) = & -\Pi_\delta + \sigma_Y^0 \left(1 - 2 \log\left(\frac{\delta}{r}\right) \right) \\ & - \Theta_\delta \frac{\sigma_Y^0 - \sigma_Y^f}{T_f} \left[\frac{(2r - \delta)b}{(b - \delta)r} - \frac{\delta}{b - \delta} \left(1 - 2 \log\left(\frac{\delta}{r}\right) \right) \right], \end{aligned} \quad (3.95)$$

in which Π_δ and Θ_δ are given by (3.90) and (3.89), respectively.

To summarize, the solution for the Von Mises yield condition is fully analytical. Once a fixed value of the radius δ , defining the position of the boundary between the internal plasticized zone and the external elastic part, is chosen, it is possible to obtain the corresponding temperature Θ_δ and pressure Π_δ from (3.89) and (3.90), respectively. Then, the stresses in the elastic part of the

shell, namely for $\delta < r < b$, can be calculated from Eqs. (3.81) and (3.82) with a , Π and Θ replaced by δ , Π_δ and Θ_δ , respectively. Finally, the stresses in the plasticized part, namely for $a < r < \delta$, can be calculated from Eqs. (3.94) and (3.95).

For the BP yield condition, the solution is semi-analytical. The stresses in the elastic part can be obtained analytically, as for the Von Mises criterion, whereas the pressure at the plasticized boundary, Π_δ , and the stresses in the plasticized part are to be obtained from the numerical solution of the equation (3.88) and the system (3.91)–(3.93), respectively. The Wolfram Mathematica computing software can be used to obtain the numerical solutions with any degree of precision, using the built-in functions `Reduce`, for Eq. (3.88), and `NDSolve`, for the system (3.91)–(3.93).



Figure 3.19: Hot pressing of a perfectly plastic thick layer, obeying Von Mises and BP yield conditions, against a rigid spherical mould. Upper part: radial (left) and tangential (right) stresses as functions of the dimensionless radial position. Lower part: mean stress p (left) and deviatoric stress q (right) as functions of the dimensionless radial position.

Results in terms of radial and tangential stress components and the two stress invariants, mean stress p and deviatoric stress q , are reported in Fig. 3.19 as functions of the radial position (normalized by the mean radius $r_m = (a + b)/2$ of the spherical shell), together with the finite element results obtained with the proposed thermoplastic model. Three different plastic boundaries δ have been considered, corresponding to the 20%, 35% and 50% of the thickness, for both Von Mises and BP yield criterion. Results presented

in the figure fully validate the proposed finite element implementation of the thermoplastic model, which has given accurate values, essentially superimposed on the semi-analytical solution.

In addition to the stresses, the plastic strains can be obtained from the solution of the algebraic-differential system composed by the compatibility equation (3.64), the associative plastic flow equation and boundary conditions,

$$\varepsilon_r^e(r) + \varepsilon_r^p(r) + \alpha_T T(r) = \frac{d}{dr} \left[r(\varepsilon_\theta^e(r) + \varepsilon_\theta^p(r) + \alpha_T T(r)) \right], \quad (3.96)$$

$$\varepsilon_\theta^p(r) = \omega(\sigma_r, \sigma_\theta) \varepsilon_r^p(r), \quad (3.97)$$

$$\varepsilon_\theta^e(\delta) + \varepsilon_\theta^p(\delta) + \alpha_T T(\delta) = \varepsilon_\theta^E(\delta), \quad (3.98)$$

where the temperature profile $T(r)$ is given by (3.62), the elastic strains $\varepsilon_r^e(r)$ and $\varepsilon_\theta^e(r)$ are given by the Hooke's law (3.66) with the stresses computed beforehand, and $\varepsilon_\theta^E(\delta)$ is the tangential strain of the elastic part of the shell at the boundary with the plasticized part. The direction of the plastic flow $\omega(\sigma_r, \sigma_\theta)$ is given by the radial and tangential components of the yield surface gradient as follows

$$\omega(\sigma_r, \sigma_\theta) = \frac{Q_\theta}{Q_r} = \frac{1}{2} \frac{\partial F}{\partial \sigma_\theta} \left(\frac{\partial F}{\partial \sigma_r} \right)^{-1}, \quad (3.99)$$

which for the Von Mises criterion takes the simple form $\omega(\sigma_r, \sigma_\theta) = -1/2$.

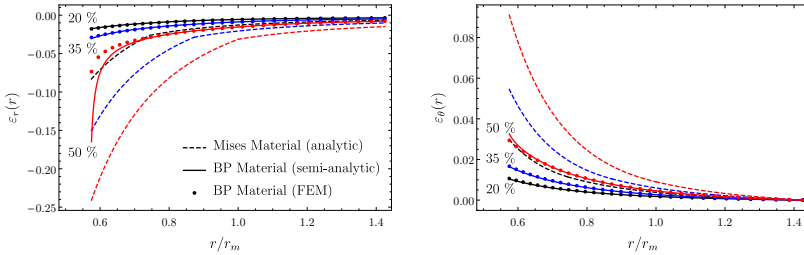


Figure 3.20: Hot pressing of a perfectly plastic thick layer, obeying Von Mises and BP yield conditions, against a rigid spherical mould. Radial (left) and tangential (right) strains as functions of the dimensionless radial position.

Results in terms of radial and tangential strain components are reported in Fig. 3.21 as functions of the radial distance (normalized by the mean radius of the spherical shell), together with the

finite element results, for both Von Mises and the BP yield conditions and the same three fractions of plasticized thickness, namely 20%, 35% and 50%. Results pertaining to the deformation of the layer further validate the finite element implementation of the thermoplastic model. The only visible discrepancy occurs for 50% of plasticized thickness at the inner part of the layer, and it is more pronounced for the radial strain, ε_r . This is due to the fact that the radial strain ε_r tends to become singular at the inner surface of the shell, as the thickness of the plasticized part increases. The finite element discretization using standard linear or quadratic elements cannot capture such singular behaviour.

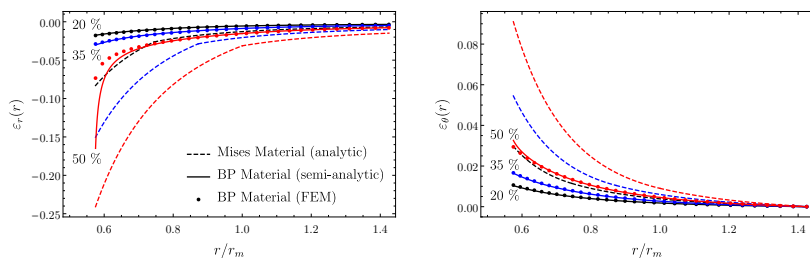


Figure 3.21: Hot pressing of a perfectly plastic thick layer, obeying Von Mises and BP yield conditions, against a rigid spherical mould. Radial (left) and tangential (right) strains as functions of the dimensionless radial position.

3.5.2 Thermal heating and expansion of a thick shell of perfectly plastic green body

For the problem of expansion of a thick shell of perfectly plastic green body subjected to both internal pressure and internal heating, the boundary conditions are as follows

$$\sigma_r(r = a) = -\Pi, \quad \sigma_r(r = b) = 0, \quad (3.100)$$

where Π is the internal pressure and the outer surface is assumed traction-free. The parameters defining the shape of the BP yield surface have been chosen to be representative of a green body partially densified, namely

$$M = 1.33, \quad m = 2, \quad \alpha = 1, \quad \beta = 1, \quad \gamma = 0. \quad (3.101)$$

The parameters describing thermal softening have been chosen to be

$$p_{c0} = 150 \text{ MPa}, \quad p_{cf} = 75 \text{ MPa}, \quad T_f = 1000, \quad (3.102)$$

whereas the ratio between the cohesion c and the consolidation pressure p_c has been fixed to be $\Omega = 1$. The increase of temperature at the inner surface has been chosen to be $\Theta = 380^\circ\text{C}$.

The traces of the BP yield surface in the $(\sigma_r, \sigma_\theta)$ -plane for fourth values of temperature, namely $T = 0, 190, 285$, and 380°C , are shown in Fig. 3.22 (solid lines), together with the traces of the Von Mises cylinder circumscribed to the BP surface (dashed lines).

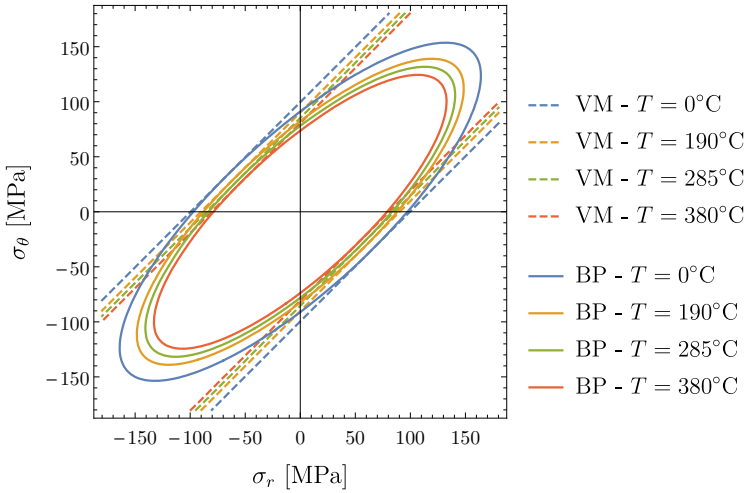


Figure 3.22: Traces of the BP yield surface in the $(\sigma_r, \sigma_\theta)$ -plane for fourth values of temperature $T = 0, 190, 285$, and 380°C (solid lines) and corresponding traces of the circumscribed Von Mises cylinder (dashed lines). Material parameters have been chosen to be representative of a green body partially densified.

The solution of this problem can be obtained with the same procedure as the one used in Section 3.5.1, since only the boundary conditions are different. The elastic solution, which holds until the internal pressure is sufficiently small, ($\Pi \leq \Pi_Y$), is given by

$$\sigma_r^E(\Pi, \Theta, r) = \frac{\Pi}{(b/a)^3 - 1} \left[1 - \left(\frac{b}{r}\right)^3 \right] + \frac{abE(a-r)(b-r)[ab + (a+b)r]\alpha_T\Theta}{(b^3 - a^3)(1-\nu)r^3}, \quad (3.103)$$

$$\begin{aligned} \sigma_{\theta}^E(\Pi, \Theta, r) &= \frac{\Pi}{(b/a)^3 - 1} \left[1 + \frac{1}{2} \left(\frac{b}{r} \right)^3 \right] \\ &\quad - \frac{abE[a^2b^2 + (a^2 + ab + b^2)r^2 - 2(a+b)r^3]\alpha_T\Theta}{2(b^3 - a^3)(1 - \nu)r^3}, \end{aligned} \quad (3.104)$$

$$\begin{aligned} \varepsilon_r^E(\Pi, \Theta, r) &= \frac{\Pi}{E((b/a)^3 - 1)} \left[(1 - 2\nu) - (1 + \nu) \left(\frac{b}{r} \right)^3 \right] \\ &\quad + \frac{a^3b^3(1 + \nu)\alpha_T\Theta}{(b^3 - a^3)(1 - \nu)r^3} - \frac{a[a^2(1 - \nu) + b\nu(a + b)]\alpha_T\Theta}{(b^3 - a^3)(1 - \nu)}, \end{aligned} \quad (3.105)$$

$$\begin{aligned} \varepsilon_{\theta}^E(\Pi, \Theta, r) &= -\frac{\Pi}{2E((b/a)^3 - 1)} \left[2(1 - 2\nu) + (1 + \nu) \left(\frac{b}{r} \right)^3 \right] \\ &\quad - \frac{a^3b^3(1 + \nu)\alpha_T\Theta}{2(b^3 - a^3)(1 - \nu)r^3} + \frac{ab(1 + \nu)\alpha_T\Theta}{2(b - a)(1 - \nu)r} \\ &\quad - \frac{a[a^2(1 - \nu) + b\nu(a + b)]\alpha_T\Theta}{(b^3 - a^3)(1 - \nu)}, \end{aligned} \quad (3.106)$$

For the Von Mises yield condition, the critical yield pressure Π_Y is given by

$$\Pi_Y = \frac{2}{3}\sigma_Y(\Theta) \left[1 - \left(\frac{a}{b} \right)^3 \right] + \frac{E(b - a)(a + 2b)\alpha_T\Theta}{3b^2(1 - \nu)}, \quad (3.107)$$

whereas for the BP yield criterion, the critical yield pressure Π_Y is obtained by solving Eq. (3.87).

For an internal pressure Π exceeding the critical yield pressure Π_Y , $\Pi > \Pi_Y$, plastic deformations develop within the spherical shell starting from the inner surface. The plasticized zone forms an internal layer with inner radius a and outer radius δ . The external part of the shell, having inner radius δ and outer radius b , behaves as an elastic layer subject to an internal pressure Π_{δ} at the interface with the plasticized zone.

The relationship between the interface radius δ and the corresponding pressure Π_{δ} can be obtained by imposing the fulfillment

of the yield conditions (3.88). For the Von Mises criterion, Π_δ is obtained as

$$\Pi_\delta = \frac{2}{3}\sigma_Y(\Theta_\delta) \left[1 - \left(\frac{\delta}{b} \right)^3 \right] + \frac{E(b-\delta)(\delta+2b)\alpha_T\Theta_\delta}{3b^2(1-\nu)}, \quad (3.108)$$

The solution for the elastic zone, $\delta < r < b$, can be obtained from Eqs. (3.103)–(3.106) where a , Π and Θ are replaced, respectively, by δ , Π_δ and Θ_δ .

The solution for the plasticized zone, $a \leq r \leq \delta$, is obtained from the algebraic-differential system (3.91)–(3.93). This system has a solution with closed form for the simple case of Von Mises yield condition. In this case the stresses takes the form (3.94) and (3.95), in which Π_δ and Θ_δ are given by (3.108) and (3.89), respectively.

Results in terms of radial and tangential stress components and the two stress invariants, mean stress p and deviatoric stress q , are reported in Fig. 3.23 as functions of the radial position (normalized by the mean radius $r_m = (a+b)/2$ of the spherical shell), together with the finite element results obtained with the proposed thermoplastic model. Three different plastic boundaries δ have been considered, corresponding to the 20%, 35% and 50% of the thickness, for both Von Mises and BP yield criterion.

In addition to the stresses, the plastic strains can be obtained from the solution of the algebraic-differential system (3.96)–(3.98).

Results in terms of radial and tangential strain components are reported in Fig. 3.24 as functions of the radial distance (normalized by the mean radius of the spherical shell), together with the finite element results, for both Von Mises and the BP yield conditions and the same three fractions of plasticized thickness, namely 20%, 35% and 50%. Results pertaining to the deformation of the layer further validate the finite element implementation of the thermoplastic model.

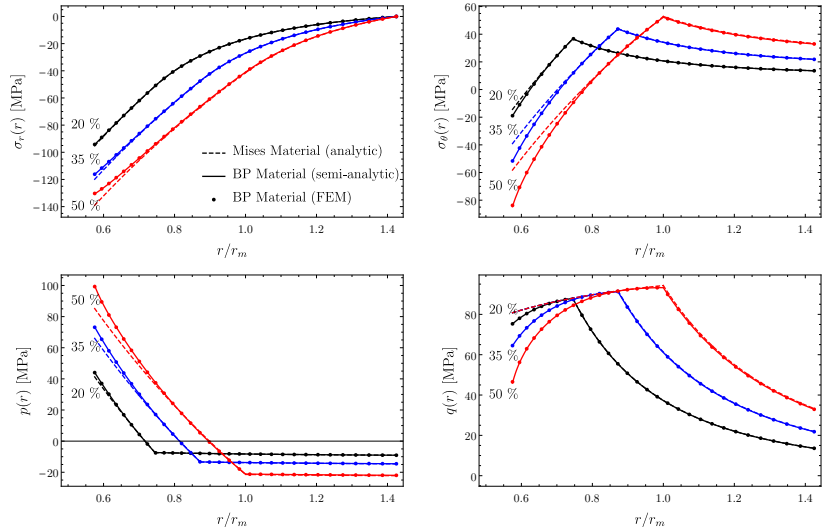


Figure 3.23: Expansion of a thick shell of perfectly plastic green body subjected to both internal pressure and internal heating. Upper part: radial (left) and tangential (right) stresses as functions of the dimensionless radial position. Lower part: mean stress p (left) and deviatoric stress q (right) as functions of the dimensionless radial position.

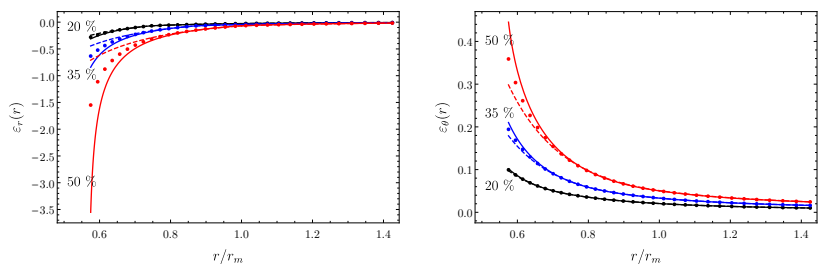


Figure 3.24: Expansion of a thick shell of perfectly plastic green body subjected to both internal pressure and internal heating. Radial (left) and tangential (right) strains as functions of the dimensionless radial position.

Chapter 4

Parameter identification through numerical optimization

In the last decades, numerical simulation has been established as a very powerful design and prototyping tool in the context of structural analysis. Its main advantage is to allow the calculation of detailed models closer to *reality*, where the growth of degrees of freedom would make the time required for any manual calculation prohibitive. Furthermore, in cases where multiple similar calculations must be carried out in a sequence, numerical simulations are extremely time-saving.

Several commercial and open source codes have been developed for the automatic solution of the PDE associated to mechanical, thermal, fluid-dynamic, acoustic or dynamic problems.

The goal of these softwares is the solution of the so-called *direct problem*, where a complete set of input data is used to compute the response of the computational model.

In engineering sometimes is required to solve the *inverse problem*, when some responses of the considered model are known but not some of the ‘causes’ leading to them, namely parameters on which the solution depends.

The relatively young scientific branch dedicated to the solution of the inverse problems takes the name of **inverse analysis** [15].

The growth of computer power according to ‘Moore’s Law’ makes inverse analysis combined with advanced programming techniques an extremely promising field.

In the present work, inverse analysis permitted the identifica-

tion of crucial material parameters entering in the governing equations of the proposed constitutive models (see 5.3, 6.4 and 7.2).

This chapter focus on the description of its fundamentals and a selection of powerful optimization algorithms.

4.0.1 Numerical optimization and objective function

For the solution of a *direct problem* defined by a set of differential equations (e.g. through FEM), the complete description of the input parameters is needed to compute the solution fields (e.g. the nodal displacements in a mechanical FEA). These parameters can be grouped in:

- Initial conditions and state variables
- Boundary conditions
- Model geometry
- Material properties

We speak of *inverse problem* if some of these information are unknown, while the solution fields (or some of them) are given. An example, if we consider a FEM mechanical simulation, is the case when nodal displacements of the model are known (at least in some nodes) while a set of parameters defining material properties, geometry or boundary conditions are missing.

In inverse analysis, differently from the usual direct problems, the collection of parameters giving the desired response might be *not unique*. This concept can be explained with the following trivial example. If we consider as direct problem computing u for a given value of x_1 in equation

$$u = x_1^2, \quad (4.1)$$

we see that a unique value of the solution u exist. However, this is not true if we consider the opposite (inverse) problem, which is to find the value of x_1 returning a known value of u : two values of x_1 corresponds to only one value u .

This lack of uniqueness is common for many inverse problems, as is the possibility of *underdetermined problems*, that is inverse problems where the number of unknowns is higher than the number of equations. This can be illustrated in the following example. Given the equation

$$u = x_1^3 + x_2^2 + x_3, \quad (4.2)$$

a possible inverse problem could be to identify x_1 , x_2 and x_3 in order to get a desired value of $u = u_{exp}$.

In this case, not only the solution (as in the previous example) lacks uniqueness, but infinite solutions are available. To allow a unique solution, or at least to reduce the number of equivalent solutions, additional equations or constraints must be added to the problem.

The single solutions are usually computed numerically, iteratively providing guess values of the unknown vector of parameters $\mathbf{x} = [x_1, x_2, x_3]$.

For this reason, solving the inverse problem implies an optimization procedure, that aims to reduce a problem-dependent **objective function** that can be generally written as

$$f = |\mathbf{u}_{exp} - \mathbf{u}_{num}|. \quad (4.3)$$

A general *constrained optimization* problem [16] is formulated as follows:

$$\begin{aligned} \text{Minimize:} \quad & f(\mathbf{x}) \\ & \mathbf{x} \in \mathbb{R}^n \\ \text{subject to:} \quad & \mathbf{g}_L \leq \mathbf{g}(\mathbf{x}) \leq \mathbf{g}_U \\ & \mathbf{h}(\mathbf{x}) = \mathbf{h}_t \\ & \mathbf{a}_L \leq \mathbf{A}_i \mathbf{x} \leq \mathbf{a}_U \\ & \mathbf{A}_e \mathbf{x} = \mathbf{a}_t \\ & \mathbf{x}_L \leq \mathbf{x} \leq \mathbf{x}_U \end{aligned} \quad (4.4)$$

where \mathbf{x} is a unidimensional vector of unknown *design variables*. The n-dimensional vectors \mathbf{x}_L and \mathbf{x}_U are respectively lower and upper bounds of the design variables. These bounds define the feasible parameter space.

It is to note that $\mathbf{g}(\mathbf{x})$ are the *nonlinear inequality constraints* which are defined by \mathbf{g}_L and \mathbf{g}_U . Similarly, $\mathbf{h}(\mathbf{x})$ are the *nonlinear equality constraints* subject to targets \mathbf{h}_t . The *linear inequality constraints* are defined through the linear system $\mathbf{A}_i \mathbf{x}$ where \mathbf{A}_i is the inequality coefficient matrix. The system $\mathbf{A}_e \mathbf{x}$ defines the *linear equality constraints*, being \mathbf{A}_e the equality coefficients matrix.

Through the applied constraints, the parameter space is divided in feasible and unfeasible regions. Any set of parameters violating one or more of the constraints is considered unfeasible.

The solution of the system (4.4) can be found with several optimization algorithms, which are summarized in Sec. 4.1.

Inverse problems can be categorized relatively to the nature of the missing information, so that an intuitive classification can be written as:

- **Backward problems:** initial conditions or initial state (internal state variables) are the goal of the inverse analysis
- **Boundary inverse problems:** boundary conditions, both of type of Neumann or Dirichlet are unknown. In the most common case the analysis aims to determine unknown external actions (e.g. forces) in order to obtain a certain known response.
- **Shape - Topology optimization:** the geometry of the the model, that is its size and shape, might be unknown. In case of shape optimization, the model is parametrized, so that its form depends on a set of defined variables. This is not required in case of topology optimization, where the optimal geometry is found by iteratively removing unneeded regions of the model in order to minimize a specific objective function (e.g. mass) while satisfying some constraints (e.g. maximum allowable stress).
- **Material parameter identification:** some or all the constants governing the constitutive equations are unknown while the desired responses of the model (e.g. displacements, stress) are known.

The last type of inverse problems is particularly common in material modeling and will therefore be detailed in the next section.

4.0.2 Material parameters identification

The identification of material parameters through inverse analysis is a very interesting field which finds several applications.

Many examples are possible:

- In structural engineering, it can be of interest identifying the minimum volumetric amount of steel fibers to mix with concrete in order to achieve stability in any point of a tunnel.
- In aeronautics, given the maximum deflection of a wing, we could be interested in finding the best composite material to build it, depending on its characteristics.

- In material modeling, assuming that the material behavior is completely defined from sufficient experimental tests, we might want to find the unknown parameters for a constitutive model in order to reproduce exactly the measured behavior.

This section gives particular focus to the problems posed in the form of the latter example.

Developing numerical models able to reproduce the behavior of particular materials is a promising research sector where a big effort was made in the last years.

The main purpose, which is also the motivation of the present work, is to achieve a precise reproduction of the material behavior, such that ‘prediction’ of the performance of a component made of the same material and subjected to different boundary conditions and with any geometry is possible.

Nowadays rather complicated material models are available in commercial and open source codes, which are able to capture a wide range of physical phenomena, such as plasticity, thermoplasticity, viscoplasticity, damage or crack development. Assuming that the chosen model can correctly describe the real phenomenon, the accuracy of the calculation still depends strongly on correct identification of the constants entering into the governing equations.

In many cases, and especially for sophisticated models, these parameters are not directly measurable by performing experimental tests, so that their identification becomes an important issue.

The identification of material parameters from measured responses is an easy task only in some simple cases (for instance, the identification of the yield stress in the von Mises criterion). For more complicated material models the identification of material parameters is not that trivial.

The measured quantities can have different forms: stress-strain or force-displacements curves, measured maximum displacements, temperatures or failure of the sample after a certain elapsed time.

The procedure for parameter identification by inverse analysis is qualitatively illustrated in Fig. 4.1. During an experiment on a material specimen, we measure some meaningful responses \mathbf{u}_{exp} of the system. A numerical simulation of the same process (e.g. by FEA - finite element analysis) is then built in order to produce a numerical counterpart of the real system. For an arbitrary set of material parameters \mathbf{x} the simulation computes the response \mathbf{u}_{num} which can be compared with \mathbf{u}_{exp} in order to evaluate the objective function f .

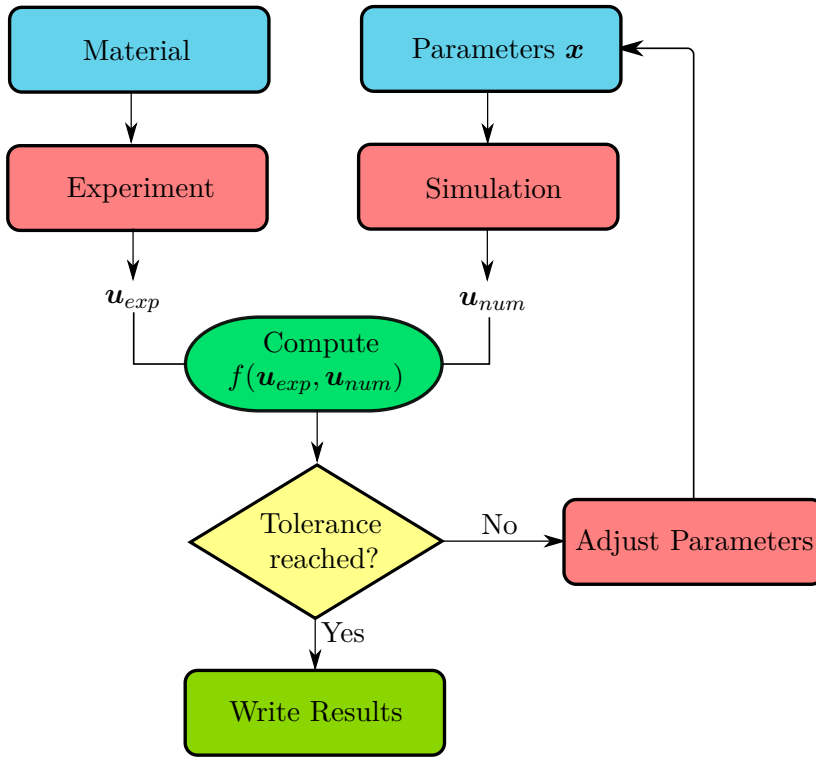


Figure 4.1: Schematic representation of material parameter identification by inverse analysis.

At this point, a certain stopping criterion should be introduced, since a small discrepancy between simulation and experiment is always expected to be present. If the cited criterion (e.g. discrepancy lower than a chosen tolerance) is not satisfied, a new set of parameters is computed by the chosen optimization algorithm and passed again to the simulation.

The constraint consideration can both be taken into account after evaluation of the objective function or directly by the optimization algorithm during the computation of a new set of parameters.

4.0.3 DACE, sensitivity analysis and uncertainty quantification

The modern ‘design and analysis of computer experiments’ (DACE) is a collection of techniques which aims to obtain as much trend data as possible from a parameter space using a limited num-

ber of sample points. There are many possible goals in running a computer experiment:

- **Parameter space exploration:** one might want to explore (randomly or not) the input parameter space in order to better understand the possible ranges of the responses.
- **Variables influence evaluation:** another goal is to determine which inputs mostly influence the output, or how changes in these parameters influence the output. Possibly, one may also want to determine the correlation between the single parameters. This is usually named *sensitivity analysis*.
- **Response surface surrogates:** the sample point can be used to create an approximation of the response surface of the model, for instance a polynomial regression model, a neural net or a Gaussian-process model. This is a particularly useful in case of extremely expensive computational models: some computer models (e.g. in fluid-dynamics) may require 15-30 hours to complete on high-performance calculators, while the associated response surface models may need just a few seconds. Thus, optimizing on the constructed response surface can be extremely efficient for some applications. This procedure is called *surrogate-based optimization*. Response surface models are valuable also in cases where the gradient and the Hessian are required by the selected optimization algorithm but expensive to compute, not available or inaccurate.
- **Optimization start point search:** several optimization algorithms require a good starting point to ensure fast convergence or to be able to converge to the right solution. In this context, the exploration of the design parameter space in order to find promising starting points is particularly important.
- **Uncertainty quantification:** uncertainty quantification (UQ) answer to questions such as: what is the probability that the response of the model is grater than 100? What is the 5th percentile of the output? UQ introduces stochastic distributions of the input parameters and propagates them through the model to obtain realistic distribution of the outputs. Experimental results are very often characterized by a certain variance, so this nondeterministic approach must often be taken into account.

Sensitivity analysis applications are particularly important in many engineering applications. These methods are used to identify the parameters having most influence on the response quantities. This information is helpful prior to starting an optimization study, allowing the detection of those parameters having small or negligible effect on the results. These parameters can then be excluded from the optimization procedure, thus importantly reducing the required computational time.

Through a proper sensitivity analysis, the behavior of the unknown response function can be detected prior starting an optimization procedure, so that the most effective optimization algorithm (see Sec. 4.1.2) can be chosen depending on the output trend (smooth or noisy, modal or multimodal).

During post-processing, sensitivity analysis can provide assessments to the *robustness* of the response function: in presence of multiple local minima, some of them could be particularly sensitive to small perturbation of the design point while some other could show higher stability. This effect must be properly taken into account in the choice of the optimal design parameters. Quasi-Monte Carlo sampling, Latin Hypercube sampling (LHS) and various types of centered/multidimensional parameter study techniques are some of the techniques available for sensitivity analysis.

Uncertainty quantification (UQ) or nondeterministic analysis [16] is defined as the process of characterizing input uncertainties, by propagating them through the computational model so that statistical assessments on the resulting responses are possible.

UQ and sensitivity analysis are related by the common goal of understanding the effects of the variations of the design parameters on the responses of the model. However, in UQ some or all the design parameters are characterized by a particular probability distribution (e.g. Gaussian, Weibull, exponential, extreme value). A good example are the mechanical properties of a material, since these show usually a certain variance. Another example could be the calculation of the failure probability of a structure for a given stochastic distribution of the external actions (e.g. snow, water pressure, wind).

Since sufficient data are generally available for aleatory variables, uncertainty quantification methods are often used to compute response distribution statistics.

4.1 Optimization algorithms

There are several algorithms that can be used to solve the constrained optimization problem expressed in system (4.4).

These algorithms require some initial guess of the design parameters and generate sequence of iterates which terminates when either no more progress can be made, or when it seems that a solution point has been approximated with sufficient accuracy.

In the following, an overview of the most common optimization algorithms and their classification is given. The goal is to present only a small portion of the theory involved in the algorithms, while focusing on the discussion of the most effective available strategies and the criteria to select the right numerical method depending on the optimization problem.

4.1.1 Classification

A first distinction can be made by analyzing the order of the derivatives required by the selected algorithm:

- **Zero order algorithms:** procedures that only require the computation of the objective function (4.3) (e.g. pattern-search methods, DIRECT (DIvision in RECTangles), evolutionary algorithms)
- **First order algorithms:** the computation of the first derivative of the objective function with respect to the design parameters $\frac{\partial f}{\partial \mathbf{x}}$ is needed to compute the solution (e.g: conjugate gradient method, steepest descent method)
- **Second order algorithms:** the second derivative (Hessian) $\frac{\partial^2 f}{\partial \mathbf{x}^2}$ is involved in the optimization procedure (e.g. Newton method)

The latter two groups can be unified as **gradient-based algorithms**, while the first are usually called **derivative-free algorithms**. Detailed information about the field of application of each group is given in Sec. 4.1.2.

A different classification can be proposed depending on the capability of the algorithm to converge to local or global minima:

- **Global methods:** these algorithms are usually able to explore the full parameters space and to return the overall minimum of the objective function. Examples are evolutionary

algorithms such as moga [17], heuristic methods such as DIRECT [16] or surrogate-based methods such as EGO [18]. With the exception of the use associated to response surface approximations, gradient-based algorithms can be used for global optimization just in case of *multi-start* procedures.

- **Local methods:** these family of methods are incapable to distinguish between global and local minima. Examples are zero order algorithms such as pattern-search, first order algorithms such as conjugate gradient methods or second order algorithms as the well known Newton method.

4.1.2 Choosing a method

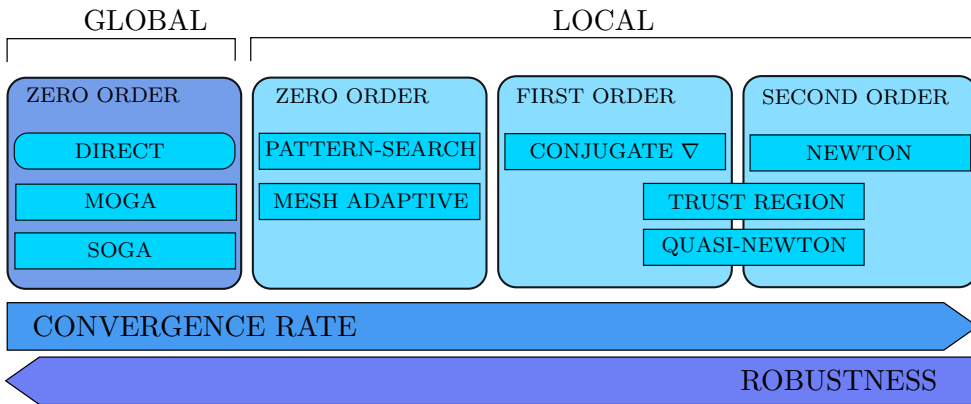


Figure 4.2: Convergence rate and robustness for a selection of optimization algorithms.

The choice of the proper algorithm is always dependent on the type and size of optimization problem that needs to be solved. Figure 4.2 shows the dependency of convergence rate and robustness depending on the chosen algorithm.

Newton methods imply finding the solution of a linear system of equations by setting the derivative of second-order Taylor series to zero. A full Newton method requires the computation of both gradient and Hessian of the objective function f with respect to the design variables \boldsymbol{x} in order to achieve quadratic convergence rates near the solution. Since in the usual case of a computational model the responses are not analytically defined, derivatives are usually computed numerically by finite differences.

Given a vector of n design parameters, the computation of the

gradient requires therefore $n + 1$ evaluations of the response function, where a ‘small’ perturbation Δx_i is applied to each parameter x_i in order to obtain a component of the gradient. If we consider the case of a two parameter set, the computation of the gradient will therefore require three operations.

The computation of the Hessian by finite differences will require at least additional n^2 function evaluations. The computation of the Hessian penalizes the second order methods, so most commonly **quasi-Newton methods** or first order methods are used instead. For quasi-Newton methods the Hessian approximation is calculated from an accumulation of gradient data. In this case, superlinear convergence rates can be obtained.

Second order optimization methods show high convergence rates, and for this reason must be chosen if the the problem is smooth, unimodal, and ‘behaves well’. However, gradient-based methods, and particularly second-order methods, can be among the least robust if the optimization problem is nonsmooth, discontinuous or shows multiple minima.

A first-order optimization algorithm of interest is the **conjugate gradient** method, which can however only be applied to *unconstrained* problems.

Conjugate gradient methods minimize a quadratic function over a space defined by the gradient and directions that are mutually conjugate with respect to the Hessian, even though the Hessian never needs to be computed. Some of the most well-known variants include the Fletcher-Reeves conjugate gradient method and the Polak-Ribiere conjugate gradient method.

The **trust region** method is based on the Newton method: it first selects the maximum distance - the so-called *trust region* Δk - and then sets the direction and the step length in order to improve the objective function inside the trust region. The sub-problem solved at each step of a trust region procedure involves

$$\begin{aligned} \text{Minimize:} \quad & m_k(\mathbf{x}_k) = f(\mathbf{x}_k) + \mathbf{x}_k^T \nabla f(\mathbf{x}_k) + \frac{1}{2} \mathbf{x}_k^T \nabla^2 f(\mathbf{x}_k) \mathbf{x}_k \\ \text{subject to:} \quad & |\mathbf{x}_k| \leq \Delta k \end{aligned} \tag{4.5}$$

where the Hessian $\nabla^2 f(\mathbf{x}_k)$ is usually approximated similarly as in the quasi-Newton methods. Differently from trust region, the **line search** method starts by fixing a direction and then identifies the appropriate distance. In both methods, adaptive computational

procedures that enlarge/restrict either the trust region step or the line-search step can be implemented.

Compared to full Newton methods, trust region and line search show enhanced robustness, while the convergence rate is penalized. The use of these methods can therefore be successful also in less smooth or less regular optimization problems.

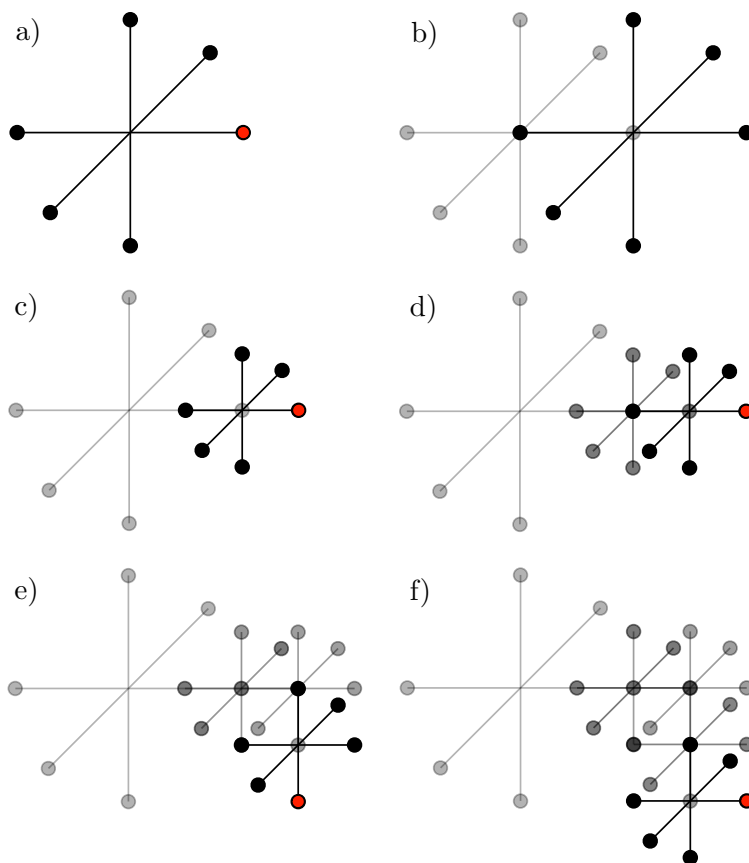


Figure 4.3: Working mechanism of the pattern-search algorithm: a) the objective function is evaluated in a collection of directions; b) the system is re-centered to the best function evaluation point (red); c) if no improvement is achieved the step length is reduced.

Derivative-free optimization methods can be much more robust and parallelizable than gradient-based optimization methods. They can be applied to those optimization problems where gradient calculation is expensive or not possible. Furthermore, they are often successful also in cases where the objective function is locally *not defined* or exhibits high noisiness. They are therefore indicated

in nonsmooth, multimodal and poorly ‘behaving’ problems.

However, the robustness of the zero-order methods is often counterbalanced by much slower convergence rates than gradient-based algorithms. Local derivative-free methods can require hundreds or thousand of iterations (depending on the number of variables) and tens of thousands in case of global derivative-free methods.

In the context of parameter identification for nonlinear constitutive models, numerical simulations might show lack of convergence in case of improper set of material parameters. In this case, such algorithms represent an important resource, which has been often employed in the development of the present work.

Pattern-search algorithms are local heuristic optimization methods that usually walk through the domain along a defined stencil of search directions as illustrated in Fig. 4.3. At each iteration, all search directions might be investigated in order to find the most promising, while the step length is iteratively decreased. The function evaluations corresponding to each stencil can easily be performed in parallel.

The **mesh adaptive search** follows a similar strategy to pattern-search, even though the search direction is defined by a mesh-structure.

Global optimization methods allow a complete exploration of the design parameter space.

DIRECT (DIvision in RECTangles) is a global heuristic method that iteratively subdivides the design parameter space in subregions in order to guarantee that iterates are generated in the neighborhood of a global minimum. It is particularly useful to quickly identify good candidate solutions that can be then refined by local optimizers.

Genetic algorithms such as **moga** (multi-objective genetic algorithm) and **soga** (single-objective genetic algorithm) are based on Darwin’s theory of survival of the fittest. The general approach consist in iterative modification of a distributed ‘population’ of individuals (parameter sets) according to the concept of natural selection, breeding and mutation. Following a sequence of generations, the best design points in the population are allowed to survive, reproduce and mutate. In manners depending on the specific evolutionary algorithm, couples of selected individual contribute their *genes* (the parameter values) to their children until global convergence is achieved.

In cases where the objective function to be minimized has a

large number of local minima, the use of genetic algorithms has shown to be particularly effective.

Analogously to natural evolution, genetic algorithms can require very long time to show their effects. This makes their use prohibitive for several applications, so that their combination with other optimization algorithms is often an efficient strategy. This possibility is described in Sec. 4.1.3.

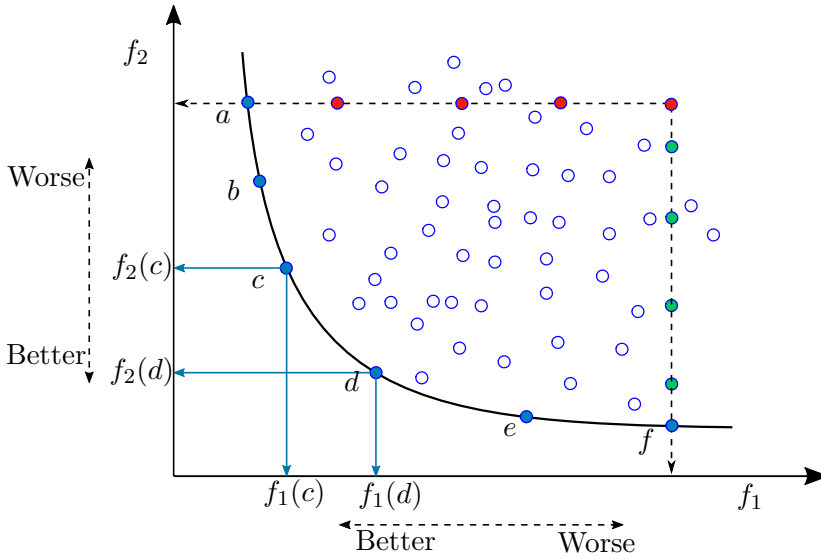


Figure 4.4: Example of Pareto front for an optimization problem with two objective functions.

Multi-objective optimization is employed if two or more objective functions need to be optimized simultaneously. These functions could be conflicting objectives, such as cost and performance. Usually, the solution of a multi-objective problem is not a single point. Rather, it is a set of points (e.g. a curve/two objective functions, a surface/three objective functions) called the *Pareto front*.

The concept of Pareto front is qualitatively illustrated in Fig.4.4: once the Pareto front is reached, one cannot improve (minimize) the value of the objective function f_1 without increasing the value of f_2 .

4.1.3 Hybrid optimization

A particular efficient strategy that has often been used in the development of the present work is the combination of multiple

optimization strategies in a **hybrid optimization**.

The goal of this method is to exploit the strengths of different minimization algorithms through different stages of the minimization process.

Global optimization methods, such as DIRECT and moga, can be used for exploration of the design space in order to identify a reasonably small number n of promising parameter sets. Since in many applications the convergence rate of evolutionary algorithms is too slow and the precision of the solution returned by DIRECT is not sufficiently high, the identified set of parameters can then be employed as starting point for local optimization strategies, such as pattern-search.

Each one of the n parameter sets can be optimized independently, so that the zero-order optimization method will lead to n refined solutions. These solutions can further be improved by employing one of the gradient-based optimization methods described previously and finally compared in order to select the preferred one.

Hybrid optimization has shown to be a valuable tool to semi-automatically determine optimal material parameter sets. Genetic algorithms such as moga allow high parallelization, so that the optimization process speeds up enormously if high-performance calculators are employed.

Chapter 5

The constitutive model for cold forming of ceramic powders

Ceramic forming by cold pressing of powders is a common practice in both traditional and advanced ceramic technologies. Due to its industrial interest, this process has been the focus of much attention by the research community over the past decades. Two main approaches in the modelling of granular matter can be distinguished: a micromechanical approach, to analyse the deformation of individual granules in detail, and a continuum macroscopic approach, to describe averaged deformations at the macroscale.

The micromechanical approach has led to the development of the discrete element method (closely related to molecular dynamics) [19–23]. This method can accurately describe the granular flow during the first stage of the compaction process (low pressure), but it is excessively detailed for later stages (high pressure) where the material is better described as a porous solid [24, 25]. Moreover, this method has the disadvantage that the size of the sample (number of particles) and the duration of a simulation are limited by the available computational power [26, 27]. For this reason, the continuum macroscopic approach is preferable for the simulation of forming of large components. Furthermore, the continuum material model can be implemented in a finite element computer code, which is more accessible to the industry than the discrete element method.

Based on the macroscopic approach, a new rational strategy is proposed in the present Chapter for the computer simulation of

real, large-scale ceramic component forming. The aim is to provide the ceramic manufacturers with an effective tool for the optimal design of moulds, punches, and presses for ceramic forming and, thus, to make virtual prototyping a realistic technology for the ceramic industry.

This Chapter is organized as follows. The continuum mechanics approach to ceramic powder densification is presented in Sec. 5.2. This includes the theoretical model as well as its finite element implementation. In Sec. 5.3 the technique for parameter identification is described by a multi-objective optimization of simulations of experimental tests. Finally, in Sec. 5.4, numerical simulations of industrial powder compaction processes are presented, namely axisymmetric tablet formation and three-dimensional tile forming. Die wall friction and deformation of the mould are taken into account. Simulated densities and lateral forces on die walls are compared with experimental results.

5.1 Material

The material considered in the present study is the aluminum silicate spray dried powder manufactured by Sacmi s.c. (Imola, Italy), labelled I14730, and described in Bosi et al. [1]. Two different water contents are considered, namely, $w = 5.5\%$ and $w = 7.5\%$, corresponding to values used in the industrial forming of traditional ceramics. The granule density, obtained with an helium pycnometer [28], is $\rho_t = 2.599 \text{ g/cm}^3$.

5.2 Constitutive framework for ceramic powder densification

The constitutive model was originally developed for the description of the compaction of alumina powder by Bigoni and co-workers [7, 14, 29–31]. That model has been modified in the present work, in order to make it more suitable for the description of the compaction of aluminum silicate powder.

All the essential equations of the constitutive model are given in the following. For details, the interested reader is referred to the above-mentioned references.

The constitutive model has been implemented in external sub-routines to be used in commercial Finite Element softwares, as elucidated at the end of this Section.

5.2.1 Constitutive formulation

The main features of the model can be summarized as follows:

(a) Non-linear elastic law

Granular materials typically show non-linear response in the elastic regime, whereas partially and fully densified green bodies behave linearly. The elastic law adopted in the model, Eq. (5.2), is able to describe this transition of elastic properties.

(b) Extremely flexible yield function [so-called ‘BP yield function’, 3] (see also Sec 2.4).

Powders and dense materials are described by yield loci of remarkably different shape. The BP yield function has the unique feature to continuously describe a transition between yield surfaces typical of different materials.

(c) Cooper-Eaton hardening law [32]

The first hardening law, Eq. (5.8), describes the densification behaviour of the material subject to isotropic compression. This law is based on a micro-mechanical model originally proposed by Cooper and Eaton [32].

(d) Increase in cohesion

The compaction process of a ceramic powder gives a form to the green body, at the same time making it cohesive and tractable for subsequent processing. The second hardening law, Eq. (5.9), describes the increase in cohesion at increasing forming pressure.

(e) Elasto-plastic coupling

During the compaction of a ceramic powder, the elastic stiffness of the material increases, a phenomenon which is clearly visible, for instance, from the unloading curves of a simple uniaxial compaction test performed at different final forming pressures [see 7]. The elastic stiffening of a ceramic powder during densification is connected with the volumetric plastic deformation of the material and has been addressed both experimentally and computationally [33, 34]. It is accounted for by incorporating into the model the so-called ‘elasto-plastic

coupling' [5, 35–37]. For a description of the concept of elasto-plastic coupling and its use to model ceramic powder compaction, see for instance Stupkiewicz et al. [38].

Compression and extension triaxial tests have been performed on aluminum silicate powder, commonly used in industrial practice to produce ceramic tiles [see 1]. These experimental results, for the first time available for aluminum silicate, indicated the necessity to introduce into the modelling a new hardening law, relating the increase of deviatoric strength to the deviatoric plastic deformation, see Eq. (5.10).

This hardening law has been adapted from the class of isotropic hardening laws proposed in Poltronieri et al. [39] to describe the nonlinear behaviour of concrete. These hardening laws display two crucial features: (i) they can be given both in an incremental and in the corresponding finite form; (ii) they describe a smooth transition from linear elastic to plastic behaviour, incorporating linear and nonlinear hardening, and may approach the perfectly plastic limit in the latter case. In particular, all three hardening laws adopted in the present model can be formulated in a finite form, see Eqs. (5.8)–(5.10), which allows for a more efficient finite element implementation.

The constitutive model is defined by 22 material parameters (see Tab. 5.1), so that an identification of these material parameters is needed and will be performed through a technique combining direct fitting of experimental results together with a multi-objective optimization on simulated experiments (Sec. 5.3).

Constitutive equations of the model for ceramic powder compaction

1. Additive split of strain into an elastic $\boldsymbol{\varepsilon}^e$ and plastic $\boldsymbol{\varepsilon}^p$ components:

$$\boldsymbol{\varepsilon} = \boldsymbol{\varepsilon}^e + \boldsymbol{\varepsilon}^p \quad (5.1)$$

2. Non-linear elastic stress/strain law:

$$\boldsymbol{\sigma}(\boldsymbol{\varepsilon}_e, e_v^p) = \left\{ -\frac{2}{3}\mu e_v^e + c + (p_0 + c) \left[\left(d(e_v^p) - \frac{1}{d(e_v^p)} \right) \frac{(1 + e_0)e_v^e}{\kappa} - \exp \left(-\frac{(1 + e_0)e_v^e}{d(e_v^p)^{1/n}\kappa} \right) \right] \right\} \mathbf{I} + 2\mu \boldsymbol{\varepsilon}^e, \quad (5.2)$$

where $\boldsymbol{\sigma}$ is the stress, $e_v^e = \text{tr } \boldsymbol{\varepsilon}^e$ and $e_v^p = \text{tr } \boldsymbol{\varepsilon}^p$ are the elastic and plastic volumetric strains, respectively, p_0 is the initial confinement and e_0 the initial void ratio.

3. Elasto-plastic coupling:

$$d = 1 + B(p_c - p_{cb}), \quad \mu(d) = \mu_0 + c \left(d - \frac{1}{d} \right) \mu_1, \quad (5.3)$$

4. BP yield function:

$$F(\boldsymbol{\sigma}, M, p_c, c) = f(p, M, p_c, c) + q g(\theta), \quad (5.4)$$

where $p = \text{tr } \boldsymbol{\sigma}$, $q = \sqrt{3 \text{ dev } \boldsymbol{\sigma} \cdot \text{dev } \boldsymbol{\sigma} / 2}$, and $f(p)$ and $g(\theta)$ are the meridian and deviatoric functions:

$$\begin{aligned} f(p, M, p_c, c) &= -M p_c \sqrt{[\phi - \phi^m] [2(1 - \alpha)\phi + \alpha]}, \\ \phi &= \frac{p + c}{p_c + c}, \end{aligned} \quad (5.5)$$

$$g(\theta) = \cos \left[\beta \frac{\pi}{6} - \frac{1}{3} \cos^{-1} (\gamma \cos 3\theta) \right]. \quad (5.6)$$

5. Non-associative plastic flow rule:

$$\dot{\boldsymbol{\varepsilon}}^p = \dot{\lambda} \left[\mathbf{Q} - \frac{1}{3} \epsilon (1 - \phi) (\text{tr } \mathbf{Q}) \mathbf{I} \right], \quad \mathbf{Q} = \frac{\partial F}{\partial \boldsymbol{\sigma}}. \quad (5.7)$$

6. Hardening laws:

$$e_v^p = -\frac{e_0}{1 + e_0} \left\{ a_1 \exp \left(-\frac{\Lambda_1}{p_c} \right) + a_2 \exp \left(-\frac{\Lambda_2}{p_c} \right) \right\}, \quad (5.8)$$

$$c = c_\infty [1 - \exp(-\Gamma < p_c - p_{cb} >)], \quad (5.9)$$

$$M = M_0 + \frac{k_1}{\delta} \frac{(1 + \delta J_2^p)^{n-1} - 1}{(n-1)(1 + \delta J_2^p)^{n-1}},$$

with (5.10)

$$J_2 = \frac{1}{2} \text{dev } \boldsymbol{\varepsilon}^p \cdot \boldsymbol{\varepsilon}^p.$$

5.2.2 Finite Element implementation and integration of the material model into commercial FEM codes

The most efficient way to implement an elastoplastic constitutive model, to be used with commercial Finite Element software, is to develop an external subroutine describing the material response.

This procedure can be carried out in Abaqus FEA by coding a UMAT (User MATerial) subroutine (see Sec. 3.1), which interfaces with the FE software through a standardized parameter list in the subroutine call statement. The UMAT code is compiled and linked to the main Abaqus executable prior to job execution.

The implementation of the constitutive model for ceramic powder compaction must overcome non-standard difficulties, which include nonlinear elastic behavior, even at small strain, and elastoplastic coupling. Furthermore, the “stretchable” pressure-sensitive yield function introduced by Bigoni and Piccolroaz [3] has the inconvenience that, in order to be convex, must be defined $+\infty$ in some regions outside the elastic domain. This fact, which prevents the application of standard return-mapping techniques for the solution of the plasticity equations, has been recently overcome by Brannon and Leelavanichkul [6], Penasa et al. [30], and Stupkiewicz et al. [38], using different strategies.

The last-mentioned technique, based on the implicit definition of the BP yield function described in Sec. 3.2.3, has been used in the current implementation of the constitutive elastoplastic model. In order to increase the stability and robustness of the subroutine, a fully-implicit return mapping technique has been combined with a substepping procedure [40, 41].

As already mentioned in Sec 3.1, the development of the UMAT subroutine code has been carried out by using the advanced hybrid symbolic-numeric approach implemented in *AceGen* [12, 13], a symbolic code generator available as a package of *Wolfram Mathematica*. The combination of automatic differentiation (AD) technique, optimization of formulae and automatic generation of computer code available in *AceGen* made possible to efficiently and rapidly prototype the new numerical procedure and benchmark the generated code, which can also be tested within the Mathematica environment by means of the flexible FE code *AceFEM*[12, 13].

The developed code has also been translated into a USERMAT subroutine for the use in the Ansys environment.

5.3 Material parameter identification by simulation of experimental tests

A novel strategy for the identification of the material parameters governing the constitutive equations of the proposed material model is introduced, based on a combination of:

- (a) Uniaxial deformation tests and triaxial tests respectively on ceramic powder and formed green bodies (see Bosi et al. [1]);
- (b) Finite element discretization and computer implementation of the mechanical model;
- (c) Parametric identification by a multi-objective optimization of simulated experimental tests.

In the following, the experimental tests and the various steps of the parameter identification procedure are accurately described.

5.3.1 Experimental tests on aluminum silicate powder

Some of the material parameters, involved in the constitutive model for ceramic powder densification, were identified directly from the results of a set of experimental tests by Bosi et al. [1]. In particular, the following tests were performed:

- (a) Uniaxial deformation test were carried out by imposing compaction of the aluminum silicate powder in a 30 mm diameter mould, filled up to a height of 4 mm. After reaching the desired pressure $\sigma_1 = \{5, 10, 30, 45, 60, 80\}$ MPa, the green body was unloaded and extracted from the device.

The uniaxial compaction test provided the force-displacement curves, from which the compaction behaviour of the powder, i.e. the relation between forming pressure and density, was deduced. This allowed the calibration of the first hardening law, Eq. (5.8), and the related material parameters, a_1 , A_1 , a_2 , A_2 . However, the identification of these parameters by a uniaxial compaction test is affected by the fact that the state of stress and deformation is not purely isotropic. This made necessary an adjustment of the values identified by Bosi et al. [1], as explained in Sec. 5.3.4.

The logarithmic elastic bulk modulus κ has been evaluated from the linear elastic phase (at very low pressure, prior to the breakpoint pressure p_{cb}).

- (b) Equi-biaxial flexure tests were performed on the green body tablets produced in the cylindrical mould, following the ASTM C 1499-05 ‘Standard Test Method for Monotonic Equi-biaxial Flexural Strength of Advanced Ceramics at Ambient Temperature’. This allowed the calibration of the second hardening law, Eq. (5.9), and the related material parameters, c_∞ , Γ , p_{cb} , describing the increase of cohesion with forming pressure.
- (c) Compression and extension triaxial tests have been performed on pre-compacted (at $\sigma_1 = 40$ MPa) cylindrical specimens (38.2 mm diameter and 70 mm height), according to the ASTM D 2664 95a ‘Standard Test Method for Triaxial Compressive Strength of Undrained Rock Core Specimens Without Pore Pressure Measurements’. The results of these tests have been used together with the results of uniaxial compaction tests in the optimization procedure.

All the other material parameters, not identified directly through the mechanical tests, are determined by simulating the experiments and performing an iterative multi-objective optimization, which was carried out with simplified numerical models, involving a small number of finite elements and neglecting the effects of friction. This approach significantly sped up the FE simulations, so that the entire parameter identification could be performed on a simple laptop computer in a reasonable computational time. This procedure leads to very accurate results, in particular for the uniaxial deformation tests, which are considered with great interest for effective simulation of industrial tile forming processes.

In both uniaxial deformation and triaxial test simulations, the FE analyses were carried out in the Abaqus FEA environment using axisymmetric 8-node biquadratic elements (CAX8).

5.3.2 Simulation of uniaxial deformation tests

The numerical simulation of uniaxial deformation tests, as performed by Bosi et al. [1], involves the execution of the following four steps:

1. **Geostatic step:** As the powder before compaction is cohesionless, the analysis starts by assuming a small confinement

given by an initial value of isotropic stress, p_0 , which is equilibrated by an equivalent external load in a geostatic step. The initial values of isotropic stress and void ratio used in the simulation are $p_0 = 0.9$ MPa and $e_0 = 2.04$.

2. **Loading:** In this step a uniform pressure is applied to the upper face of the sample, see Fig. 5.1, while the constraints at the bottom and lateral surfaces reproduce frictionless contact with the mould.
3. **Unloading:** In this phase the pressure on the upper face is removed, while the boundary constraints at bottom and lateral faces are kept active, in order to simulate the removal of the punch.
4. **Extraction:** The supports on the right side of the sample are deactivated in the last step, so that the compact is free to expand transversally, which reproduces the ejection from the mould.

Figure 5.1 shows the undeformed mesh with the constraints to reproduce uniaxial deformation conditions (left) and the deformed mesh at the end of the loading step (right, the contours denote vertical displacement).

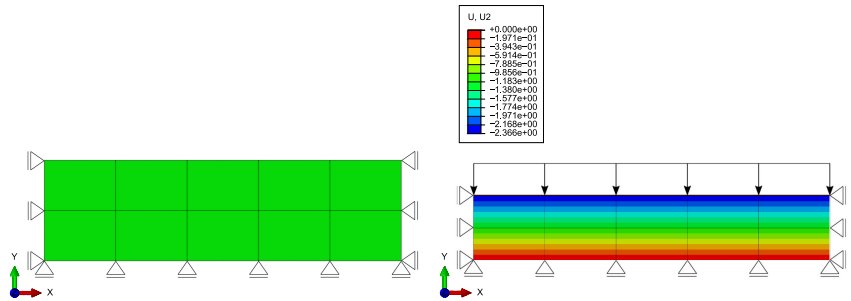


Figure 5.1: Simplified FE model for uniaxial compaction simulation. Undeformed mesh (left) and deformed mesh at the end of loading step (right, contours denote vertical displacement).

5.3.3 Simulation of compression and extension triaxial tests

The FE analysis was carried out to simulate the triaxial tests performed by Bosi et al. [1], on cylindrical samples, pre-compacted

at 40 MPa. This involves two stages. The first stage corresponds to the preparation of cylindrical specimens, formed by uniaxial compaction at 40 MPa, followed by an isotropic compaction at 40 MPa in the triaxial cell. After unloading, the second stage corresponds to the actual triaxial test. Both compression and extension triaxial tests were simulated in the way described below.

Stage 1: forming of cylindrical specimens

1. **Geostatic step:** The first geostatic step aims to equilibrate, by imposing an external pressure, p_0 , the assumed initial isotropic confinement in the ceramic powder. The initial values of isotropic stress and void ratio used in the simulation are $p_0 = 0.9$ MPa and $e_0 = 2.04$.
2. **Uniaxial compaction at $\sigma_2 = 40$ MPa:** The powder is first compacted in a uniaxial deformation step at a final vertical stress equal to 40 MPa.
3. **Unloading:** In this step the sample is unloaded.
4. **Isotropic compaction at $p = 40$ MPa:** An uniform pressure of 40 MPa is applied on both faces of the sample (see Fig. 5.2): $\sigma_1 = \sigma_2 = 40$ MPa.
5. **Unloading:** In this step the sample is unloaded.

Stage 2: triaxial test

1. **Isotropic loading:** The confinement pressure is applied on all faces of the sample: $\sigma_1 = \sigma_2 = \{2, 5, 10, 15, 20, 30\}$ MPa.
2. **Deviatoric loading:** Compression triaxial test: on the upper face of the cylinder a negative displacement is imposed, in order to reduce the height of the sample. Extension triaxial test: on the lateral face of the cylinder a negative displacement is imposed, in order to reduce the width of the sample.

Figure 5.2 shows the undeformed mesh with the constraints to reproduce uniaxial compaction conditions (step 2 of Stage 1, left), the deformed mesh at the end of forming of the cylindrical specimen (end of Stage 1, centre), and the deformed mesh at the end of triaxial test (right). In the central and right figures, contours denote vertical displacement.

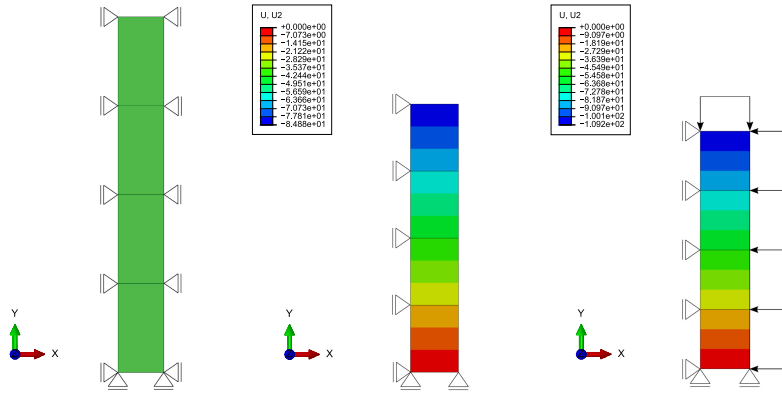


Figure 5.2: Simplified FE model for triaxial test simulation. Undeformed mesh (left), deformed mesh at the end of Stage 1 (forming of cylindrical specimen, centre) and deformed mesh at the end of Stage 2 (triaxial test, right). The contours denote vertical displacement.

5.3.4 Material parameter identification by multi objective optimization

A multi-objective optimization procedure has been performed in order to identify the constitutive parameters not directly calibrated from the experimental tests performed by Bosi et al. [1].

These parameters include: the elasto-plastic coupling parameters, B , n , μ_0 and μ_1 , governing the evolution of elastic properties with plastic deformation, Eq. (5.3); the parameters involved in the deviatoric hardening rule, Eq. (5.10), M_0 , k_1 , δ_1 and n_1 ; the parameter ϵ defining the non-associativity, Eq. (5.7).

In addition, the parameters a_1 , Λ_1 , a_2 , Λ_2 , governing the pressure-density behaviour of the powder in isotropic compression, were included in the optimization. This was done because isotropic compression tests are not available, and thus the values identified by Bosi et al. [1] through uniaxial compaction tests require an adjustment.

With the introduction of the deviatoric hardening rule, Eq. (5.10), the parameter M , describing the pressure-sensitivity, Eq. (5.5), evolves during the densification. This fact is expected to influence also the other parameters governing the meridian shape of the BP yield function, m and α , which are therefore also included in the optimization.

The multi-objective optimization has been performed by employing the algorithms available in the Dakota Framework [16],

which allows the optimization with both gradient and nongradient-based methods. The chosen optimization strategy aims to find the best possible fit between simulated results and experimental curves, both for uniaxial compression and triaxial compression tests.

The random combination of material parameters, even inside their allowable ranges, may lead to inconsistent results or lack of convergence. For this reason a gradient-free approach has been preferred in the optimization procedure. As a sufficiently precise starting point was not available, both global and local optimization methods have been used to efficiently estimate the material parameters.

The ‘hybrid’ procedure involves first a Pareto optimization, by means of moga (multi-objective genetic algorithm). After a sufficiently high number of iterations of the global algorithm, the best five solutions are refined by a local optimization method (pattern-search). The convergence of the optimization strategy, in terms of relative error as a function of the number of iterations, is shown in Fig. 5.3.

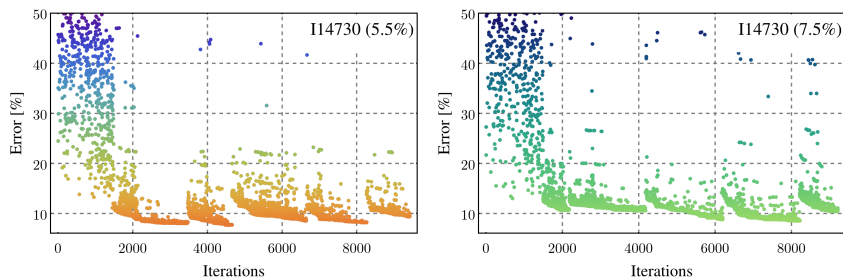


Figure 5.3: Convergence of the hybrid optimization algorithm for aluminum silicate powder with $w = 5.5\%$ (left) and $w = 7.5\%$ (right) water content.

The graph shows how, with the increase of the number of iterations, the parameters generating low error tend to become more dense (moga algorithm). After 1500 iterations, the best five solutions of the global algorithm are refined using a local optimization method (pattern-search algorithm) until convergence.

In order to reduce the size of the problem, the optimization focused on reaching the best fit for the experimental tests considered of highest industrial interest, namely:

- Uniaxial compaction tests at $\sigma_2 = \{45, 60\}$ MPa
- Triaxial compression tests at cell confinement: $\sigma_1 = \sigma_3 = \{20, 30\}$ MPa

The final set of parameters for the compaction of aluminum silicate for two different water contents, $w = 5.5\%$ and $w = 7.5\%$ are reported in Tab. 5.1.

Table 5.1: Material parameters for the compaction of aluminum silicate I14730, for two different water contents, $w = 5.5\%$ and $w = 7.5\%$. Seven parameters were obtained directly from the experiments by Bosi et al. [1], the other 15 parameters have been identified by multi-objective optimization.

		Parameter	Aluminium Silicate I14730	
			$w = 5.5\%$	$w = 7.5\%$
Parameters identified directly from experiments				
Log. Bulk Modulus	(1)	κ	0.08	0.099
	(2)	p_{c0}	0.09 MPa	0.09 MPa
Yield Surface	(3)	β	0.1	0.08
	(4)	γ	0.9	0.9
Hardening law (5.9)	(5)	p_{cb}	0.22 MPa	0.17 MPa
	(6)	c_∞	1.10 MPa	1.35 MPa
	(7)	Γ	0.06 MPa^{-1}	0.10 MPa^{-1}
Parameters identified by multi-objective optimization				
Yield Surface	(8)	M_0	0.398	0.506
	(9)	m	2.26	3.17
	(10)	α	1.09	1.367
Hardening law (5.8)	(11)	a_1	0.763	0.780
	(12)	Λ_1	0.702 MPa	0.507 MPa
	(13)	a_2	0.154	0.154
	(14)	Λ_2	36.285 MPa	25.19 MPa
Hardening law (5.10)	(15)	k_1	301.417	30.08
	(16)	δ_1	456.806	165.405
	(17)	n_1	3.647	9.149
E-P Coupling (5.3)	(18)	B	9.580 MPa^{-1}	6.908 MPa^{-1}
	(19)	n	11.949	11.749
	(20)	μ_0	0.223 MPa	9.822 MPa
	(21)	μ_1	24.678	5.269
Plastic flow (5.7)	(22)	ε	0.916	0.586

With the identified parameters, it is possible to obtain a good agreement between numerical and experimental results also in tests

which are not considered in the optimization. This is an indication of the consistency of the constitutive model and of the validity of the optimization procedure. Figure 5.4 shows the uniaxial compaction (force vs. displacement) curves for water content $w = 5.5\%$ (left) and $w = 7.5\%$ (right). Figure 5.5 shows the compression/extension triaxial (von Mises stress vs. axial strain) curves for water content $w = 5.5\%$ (left) and $w = 7.5\%$ (right).

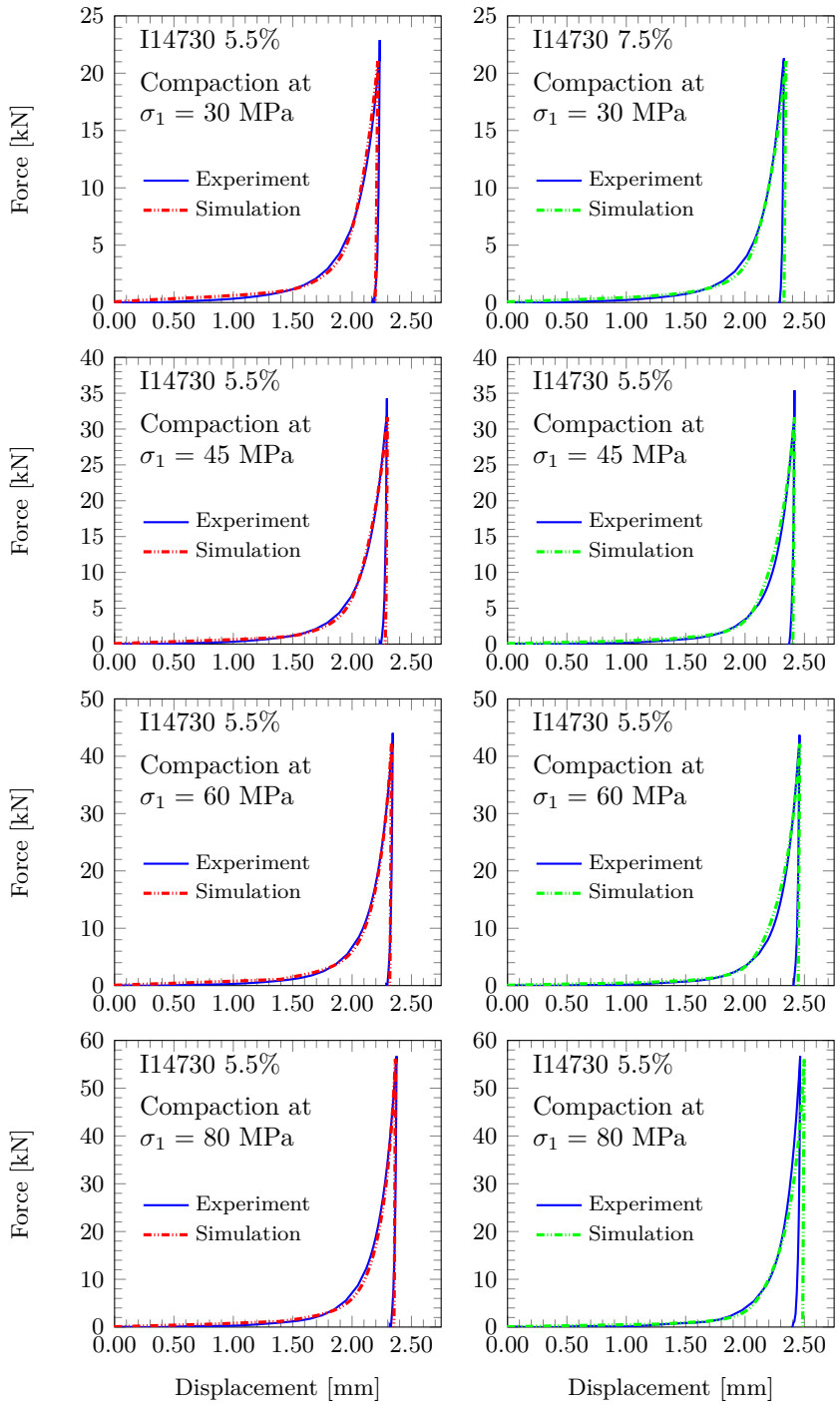


Figure 5.4: Uniaxial compaction test: Comparison between experimental results and numerical simulations obtained with the identified material parameters (Tab. 5.1), for water content $w = 5.5\%$ (left) and $w = 7.5\%$ (right).

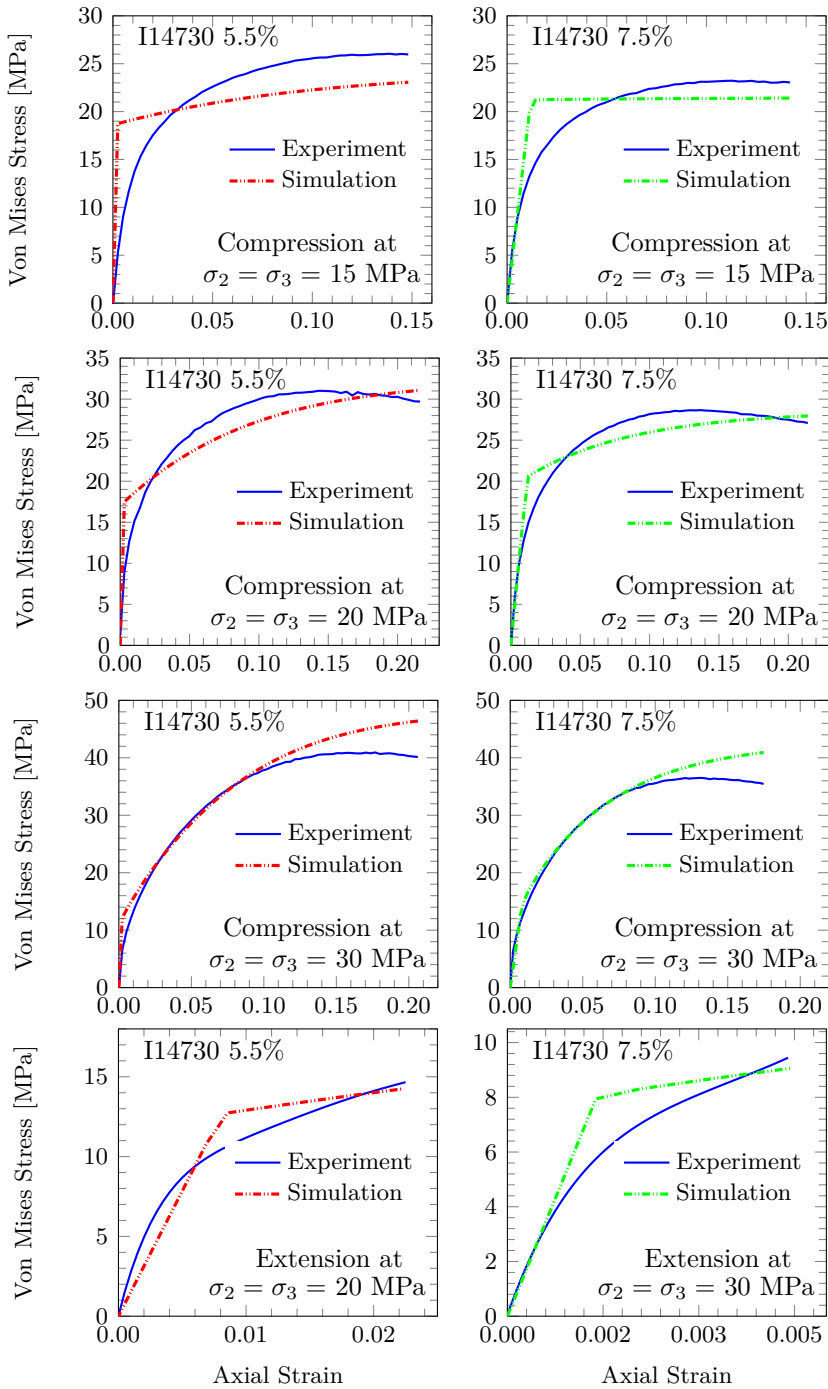


Figure 5.5: Compression/extension triaxial test: Comparison between experimental results and numerical simulations obtained with the identified material parameters (Tab. 5.1), for water content $w = 5.5\%$ (left) and $w = 7.5\%$ (right).

5.4 Numerical simulation of industrial powder compaction processes

The capabilities of the proposed constitutive model are highlighted through computer simulations of realistic industrial compaction processes, namely, the forming of an axisymmetric tablet and of a three-dimensional ceramic tile, where the material parameters identified according to the procedure described in Sec. 5.3 are considered.

The transversal load on the lateral die wall computed in the numerical analyses results particularly in agreement with the values of contact pressure measured during the uniaxial deformation tests. The density values and void ratio distribution at the end of the compaction process appear compatible with the experimental data.

In the following, the results of the numerical simulations are discussed and compared with those obtained in the experiments.

5.4.1 Experimental identification of friction coefficient between powder and die wall

At the end of process of powder compaction, the sample is unloaded and extracted from the forming device. In this phase, friction between the green body and the steel matrix requires the application of an axial force on the tablet to complete the extraction.

In the experimental tests performed by Bosi et al. [1], it was possible to measure the tangential force T required to remove the green body from the mould. The normal force N on the steel matrix can be calculated from the measured radial deformation of the sample after extraction and the elastic moduli, measured by means of ultrasound technique by Argani et al. [33].

The static friction coefficient can be estimated from the relationship between tangential and normal forces acting on the die wall. The calculation of static friction coefficient for forming pressure of 45 MPa yielded $\mu_s = T/N = 0.18$. This value has been used in the following FE simulations in order to accurately reproduce the contact interaction between ceramic powder and steel matrix.

5.4.2 Numerical simulation of axisymmetric tablet forming

Finite element analyses, involving contact interaction and friction, have been performed to accurately reproduce the uniaxial compaction tests performed by Bosi et al. [1]. In these simulations, the complete forming device, composed by matrix, upper and lower punches, was modelled, and the interaction between each single part and the ceramic powder was taken into account.

The experimental set-up used in the uniaxial compaction test of I14730 aluminum silicate powder, performed by Bosi et al. [1] is shown in Fig. 5.6: the schematic cross section on the left and a photograph in the centre. The elements considered in the simulation are shown on the right: ceramic powder, cylindrical matrix, bottom and upper punches.

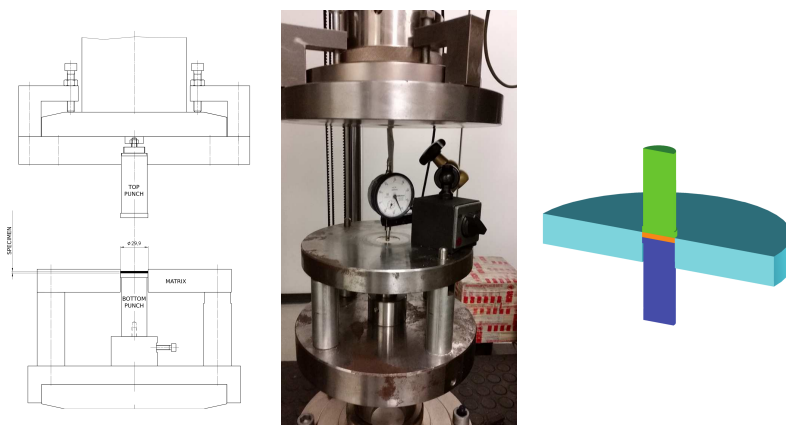


Figure 5.6: Experimental set-up used in the uniaxial compaction test of I14730 aluminum silicate powder, performed by Bosi et al. [1]. Cross section (left) and photograph (centre) of the forming device. The elements considered in the simulation: matrix, upper and lower punches, and ceramic powder (right).

The simulation comprises the following steps: geostatic step, in which an initial confinement p_0 is imposed on the powder; uniaxial compaction phase, in which the upper punch is loaded by the given vertical pressure; unloading step, in which the load on the upper punch is removed; extraction, in which the matrix is removed in order to simulate the removal of the tablet from the cylindrical mould.

The stresses developing in the ceramic powder as well as in the mould are shown in Fig. 5.8. The analysis made also possible to

investigate the influence of friction in the forming process and to determine the transversal pressure on the steel matrix.

The dimensions and densities of the formed tablets are reported in Tables 5.2 and 5.3, for aluminum silicate powder with water content 5.5% and 7.5%, respectively. The simulation results are in good agreement with the experimental values. We note that a reduced radial ‘springback’ after extraction of the tablet from the mould was predicted by the numerical simulations.

A comparison of experimental and simulated compact densities is shown in Fig. 5.7, for water content 5.5% (left) and 7.5% (right).

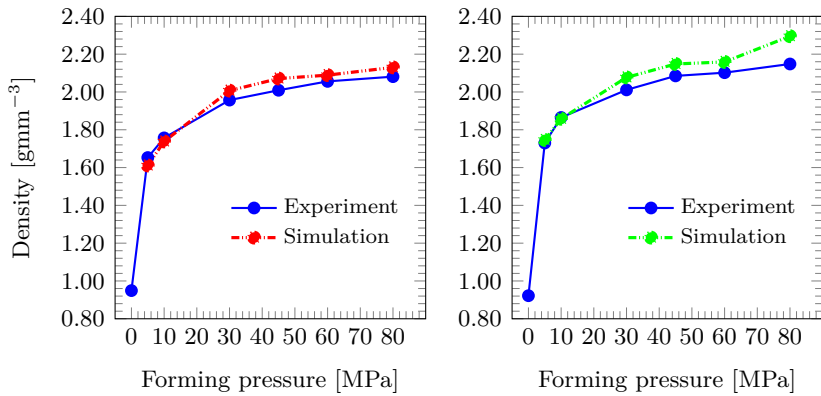


Figure 5.7: Densities of I14730 aluminium silicate tablets, with 5.5% and 7.5% of water content: comparison between experimental result and numerical simulation for different forming pressures. The first experimental point shows the average bulk density of the ceramic powder when inserted in the cylindrical mould.

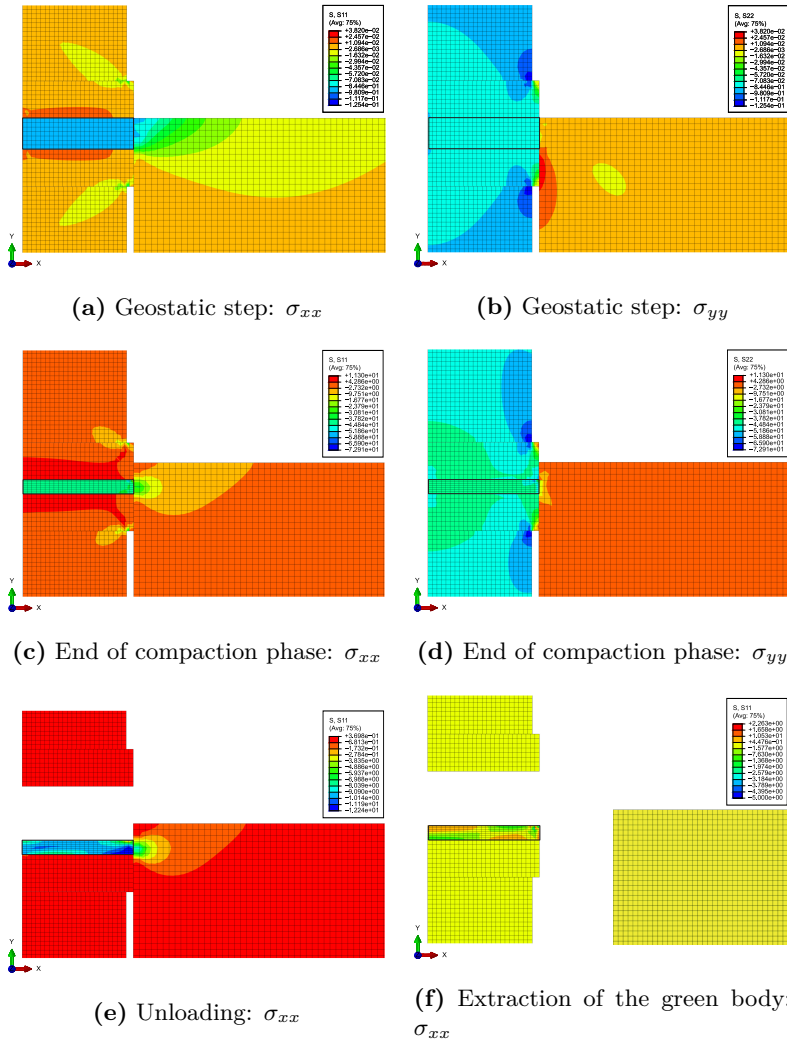


Figure 5.8: Axisymmetric numerical simulation of tablet forming. Stress distribution (lateral stress σ_{xx} and axial stress σ_{yy}) in the ceramic powder and in the mould (composed by matrix, upper and lower punches) at the end of the main stages of powder compaction: geostatic step (upper part), axial loading (central part), axial unloading (lower part, left) and extraction of the tablet (lower part, right).

Table 5.2: Dimensions and densities of I14730 aluminum silicate tablets (w=5.5%) after completion of the uniaxial compaction process and extraction from the cylindrical mould.

Pressure [MPa]		Area [mm ²]	Height [mm]	Diameter [mm]	Density [g cm ⁻³]
5	Experiment	706.387	2.338	29.990	1.653
	Simulation	708.452	2.392	30.034	1.611
10	Experiment	706.858	2.198	30.000	1.757
	Simulation	705.841	2.225	29.978	1.738
30	Experiment	708.273	2.042	30.030	1.957
	Simulation	703.554	2.004	29.930	2.007
45	Experiment	708.745	1.966	30.040	2.009
	Simulation	703.225	1.923	29.923	2.071
60	Experiment	708.745	1.880	30.040	2.056
	Simulation	703.065	1.865	29.919	2.089
80	Experiment	708.745	1.844	30.040	2.081
	Simulation	702.962	1.817	29.917	2.130

Table 5.3: Dimensions and densities of I14730 aluminum silicate tablets (w=7.5%) after completion of the uniaxial compaction process and extraction from the cylindrical mould.

Pressure [MPa]		Area [mm ²]	Height [mm]	Diameter [mm]	Density [g cm ⁻³]
5	Experiment	705.916	2.236	29.980	1.730
	Simulation	704.175	2.221	29.943	1.746
10	Experiment	705.916	2.074	29.980	1.865
	Simulation	703.451	2.089	29.928	1.858
30	Experiment	707.801	1.918	30.020	2.011
	Simulation	702.981	1.870	29.918	2.077
45	Experiment	707.943	1.836	30.023	2.085
	Simulation	702.905	1.795	29.916	2.148
60	Experiment	708.745	1.772	30.040	2.102
	Simulation	702.868	1.740	29.915	2.159
80	Experiment	708.273	1.814	30.030	2.148
	Simulation	702.868	1.711	29.915	2.295

5.4.3 Three-dimensional numerical simulation of an industrial tile forming process

Three-dimensional FE simulations of an industrial tile forming process have been performed in Abaqus FEA environment using the developed constitutive model and the identified parameters listed in Tab. 5.1. The 3D model involves contact interactions between ceramic powder, steel matrix and top/bottom steel plates, where the friction coefficient reported in Sec. 5.4.1 has been used.

Figure 5.9 shows the vertical and transverse stress distributions in the ceramic powder and in the mould (composed by matrix, upper and lower plates) at the end of the main stages of powder compaction.

The initial values of isotropic stress and void ratio prescribed in the geostatic step are $p_0 = 0.09$ MPa and $e_0 = 2.04$, respectively, which are the same values used in the axisymmetric case. This step corresponds to the initial confinement inside the mould, see Fig. 5.9a and 5.9b.

At the end of the compaction phase, Fig. 5.9c and 5.9d, we notice a non-uniform stress distribution, especially for the transversal stress σ_{yy} , in the external part of the tile, which is in contact with the die wall. This effect is mainly due to friction between the ceramic powder and the mould.

After the unloading step (removal of the upper plate), see Fig. 5.9e, the transversal stress σ_{yy} in the green tile is still quite high, approximately 8 MPa, due to the lateral constraint given by the matrix.

The residual stresses at the end of the extraction phase, predicted by the finite element simulation, are shown in Fig. 5.9f. We notice a compressive transversal stress σ_{yy} at the upper edge of the tile, which is balanced by a tensile σ_{yy} at the lower edge. The capabilities of the model to predict residual stresses are crucial, since residual stresses may lead to fracture of the green body, by end capping or lamination.

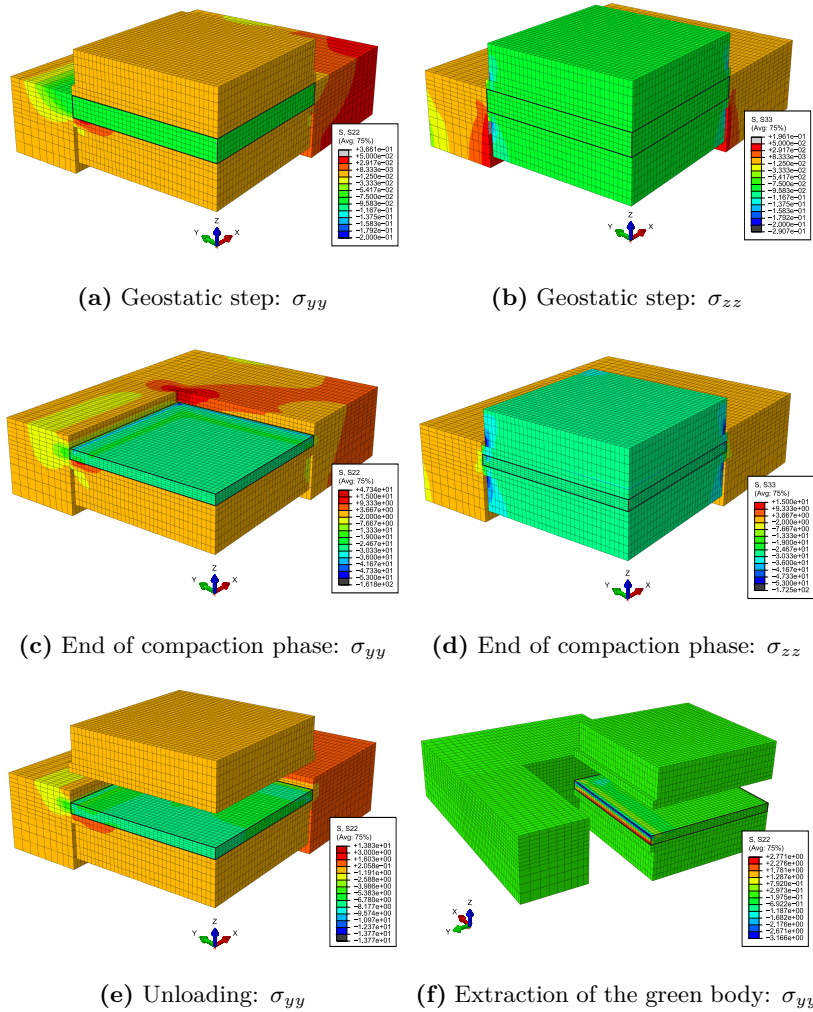


Figure 5.9: Three-dimensional numerical simulation of industrial tile forming. Stress distribution (lateral stress σ_{yy} and axial stress σ_{zz}) in the ceramic powder and in the mould (composed by matrix, upper and lower plates) at the end of the main stages of powder compaction: geostatic step (upper part), axial loading (central part), axial unloading (lower part, left) and extraction of the tile (lower part, right).

5.4.4 Estimation of transversal load on the lateral die wall

All FE analyses denoted high contact pressure values on the steel matrix. For an applied axial load of 45 MPa, three-dimensional and two-dimensional simulations yielded average transversal pressure values equal to 37.73 MPa and to 39.45 MPa, respectively. The contact pressure for the three-dimensional simulation is shown in Figure 5.11 (upper part). The average contact pressure has been calculated by dividing the resultant of the nodal contact forces by the contact area.

These values of lateral contact pressure on the die wall are much higher than those usually considered in the design of tile forming devices. In the industrial practice, the lateral contact pressure is empirically assumed to be one sixth of the axial pressure applied on the powder.

To clarify this point, a specific experimental investigation has been performed, by placing a pressure-sensitive *Fuji Prescale MS* film between ceramic powder and steel matrix, see Fig. 5.10.

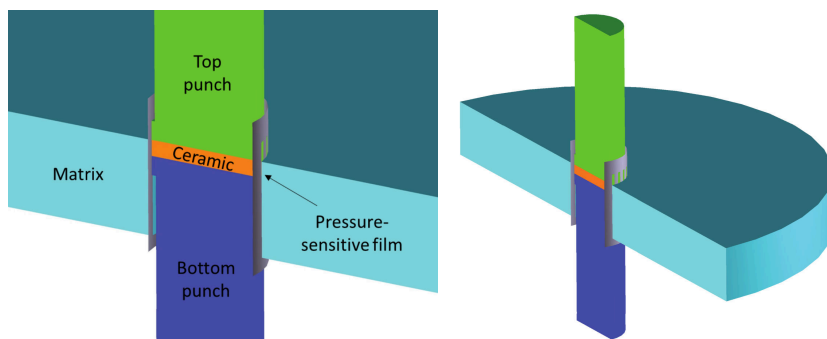


Figure 5.10: Description of the performed experimental test: the pressure-sensitive film is placed between the ceramic powder and the steel matrix.

This film is composed of a polyester base on which a colour-developing material is coated, with the micro-encapsulated colour-forming material layered on top. When pressure is applied on the film, the microcapsules are broken and the colour-forming material reacts with the colour-developing material, and this process causes magenta colour forming. Microcapsules are designed to react to various degrees of pressures, releasing their colour forming material at a density that correspond to specific levels of applied pressure.

Figure 5.11 (lower part) shows the imprint left by the ceramic powder on the pressure-sensitive film. The lateral pressure on the

matrix was obtained by analysing the image using a dedicated program that converts magentascale to RGB values. For a forming axial pressure of 45 MPa, the measured average lateral pressure on the matrix is equal to 39 MPa, confirming the results of the simulations with a very good accuracy.

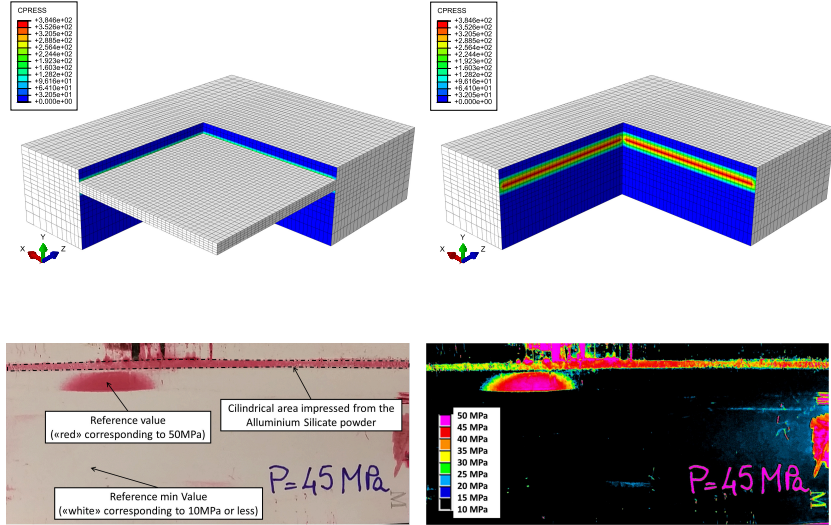


Figure 5.11: Contact pressure values in the three-dimensional simulation (upper part) and imprint left on the pressure-sensitive film after the experimental test (lower part).

5.4.5 Density distribution in a combed-finish tile after die pressing

The density distribution in green bodies is of primary importance in the optimization of tile forming processes. In fact, non-uniform density can affect the subsequent sintering process, resulting in poor quality of the final ceramic product. Figure 5.12 shows the void ratio distribution in a combed finish tile green body, predicted by the finite element simulation. The void ratio, defined as the ratio of the volume of voids to the volume of solid, $e = V_V/V_S$, is related to the relative density by

$$\frac{\rho}{\rho_0} = \frac{1 + e_0}{1 + e}, \quad (5.11)$$

where ρ_0 and e_0 are the initial values. We notice higher void ratio values, corresponding to lower density, in correspondence of the

protrusions. These results pave the way to more advanced virtual prototyping analyses, aiming at the optimization of the design of tile forming devices, in order to produce green bodies with improved density distribution.

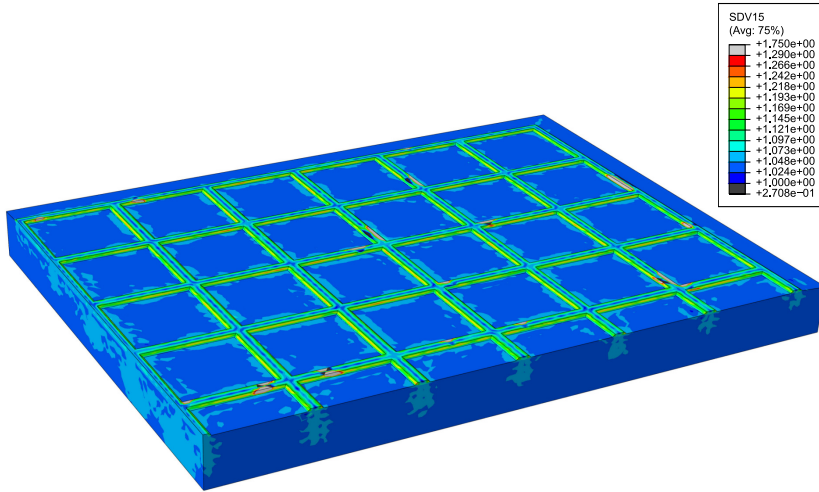


Figure 5.12: Void ratio distribution in a combed finish tile after die pressing.

Chapter 6

The constitutive model for refractories

This chapter presents innovative approaches to the mechanics of refractory materials at high-temperature for advanced industrial design. The applications are envisaged in several industrial sectors, in particular in the molten metal flow engineering sector.

One of the key issues is the development and implementation of a specific constitutive model for refractories, in order to enhance the description of their thermo-mechanical properties and thus improve their performance and reliability.

In the following, the formulation of the presented model is described in detail. Special focus is given to the identification of material parameters, where experimental tests and multi-objective optimization techniques were successfully employed. Finally, comparisons between experiments and numerical simulations are discussed.

This constitutive model is one of the outcomes of the collaboration between University of Trento and Vesuvius Group within the HOTBRICKS European project. Please note that information about the chemical composition and the constitutive parameters describing the features of Vesuvius materials are strictly confidential and therefore not presented in the current work. The main goal is to give a description of the constitutive formulation, parameter identification procedure and performed experimental tests, avoiding disclosure of protected information.

6.1 Thermoplastic Constitutive formulation

The proposed constitutive model for refractories is formulated in the frame of thermo-plasticity. Thermal effects are crucial for refractories, which are subject to high temperature under working conditions.

Particular care is given to the proper description of the effects of temperature on the mechanical properties of the investigated materials. As explained in more detail in Sec. 6.4, the temperature usually affects the material yield strength and ultimate strength but, for some material compositions, opposite effects are observed. The temperature has an influence also on the elastic properties, so these effects are taken into account in the proposed model.

Differently from the model for ceramic powder densification presented in Ch. 5, linear behavior is assumed inside the elastic domain, which is defined through the BP yield criterion.

The constitutive model is formulated with regard to associative plasticity, so that the plastic flow direction is always normal to the yield surface.

Rate-dependence has been included in the proposed thermo-plastic constitutive model according to the general formulation illustrated in Sec. 2.3. However, at present, experimental results on this particular effect are still not sufficient for a comparison.

6.1.1 Elastic potential and temperature dependence

Heat resistant materials show an evident dependence of the elastic properties on temperature. Therefore, a temperature dependent elastic potential is introduced as

$$W(T, \boldsymbol{\varepsilon}) = \frac{\lambda(T)}{2} \text{tr} \boldsymbol{\varepsilon}^2 + \mu(T) \boldsymbol{\varepsilon}^2, \quad (6.1)$$

where $\lambda(T)$ and $\mu(T)$ are the Lamè constants. It is assumed that the Young's modulus is temperature-dependent, $E(T)$, whereas the Poisson ratio is constant, ν . The Lamè constants can be obtained as

$$\lambda(T) = \frac{E(T)}{(1 + \nu)(1 - 2\nu)}, \quad (6.2)$$

$$\mu(T) = \frac{E(T)}{2(1 + \nu)}. \quad (6.3)$$

Experimental tests on different refractory compositions have shown very dissimilar dependence of the elastic properties on the temperature. For this reason, a general analytic expression for the elastic modulus is of difficult identification. The most general way to describe the relationship between elastic modulus and temperature is by introducing a polynomial in the form

$$E(T) = \sum_{i=0}^n p_i T^i \quad (6.4)$$

where the vector of coefficients \mathbf{p} can be easily identified by polynomial regression for each considered material.

6.1.2 Temperature-dependent hyperbolic strain hardening and thermal softening

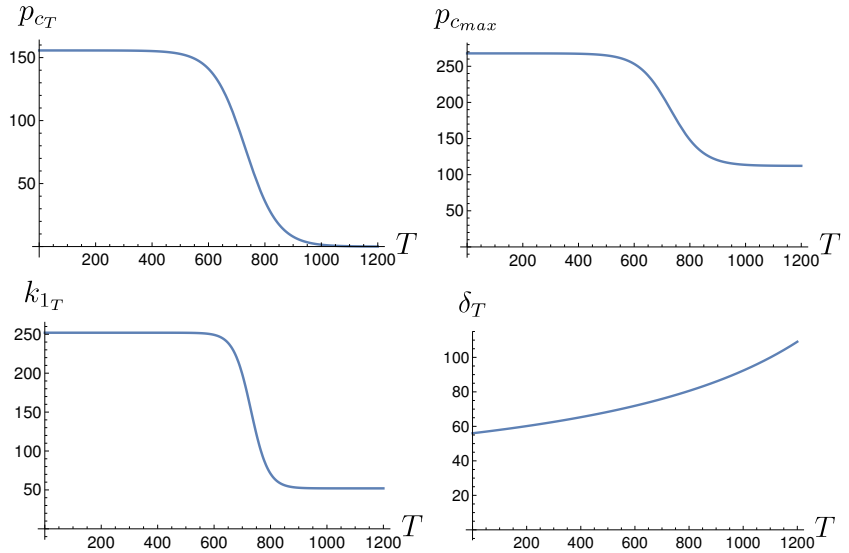


Figure 6.1: Temperature-dependent hardening rules for the proposed thermo-plastic constitutive model. The limit value of isotropic strength $p_{c_{max}}$ evolve according expression (6.7), where A^{p_c} is replaced by the ultimate isotropic strength at room temperature $p_{c_{max0}}$.

The BP yield function is regulated by possibly conflicting contributions due to strain hardening and thermal softening.

The dependence of isotropic strength in compression p_c and in

tension c on the temperature is set in the following form

$$p_c = p_{c_T} + \frac{k_{1T}}{1 + \delta_T P(\boldsymbol{\varepsilon}_p)} P(\boldsymbol{\varepsilon}_p), \quad (6.5)$$

$$c = c_T = \Omega p_{c_T}, \quad (6.6)$$

where $P(\boldsymbol{\varepsilon}_p)$ is the accumulated plastic strain, see Eq. (2.31), Ω is a material parameter, p_{c_T} , k_{1T} and δ_T are functions of the temperature T and are defined as follows.

The first term in Eq. (6.5) regulates thermal softening and is defined as

$$p_{c_T} = A^{p_c} - B^{p_c} \tanh\left(\frac{T - T_0^{p_c}}{C^{p_c}}\right), \quad (6.7)$$

while strain hardening depends on temperature through the functions

$$k_{1T} = A^{k_1} - B^{k_1} \tanh\left(\frac{T - T_0^{k_1}}{C^{k_1}}\right), \quad (6.8)$$

and

$$\delta_T = \delta_0 \exp\left(-\frac{T - T_0^\delta}{T - T_F}\right). \quad (6.9)$$

In the numerical implementation of the proposed constitutive model, the accumulated plastic strain $P(\boldsymbol{\varepsilon}_p)$ is calculated at each time-step i from its incremental expression (2.33) as

$$P(\boldsymbol{\varepsilon}_p)_i = P(\boldsymbol{\varepsilon}_p)_{i-1} + (\lambda_i - \lambda_{i-1}) |\mathbf{Q}|. \quad (6.10)$$

where \mathbf{Q} is the gradient of the BP yield function $\mathbf{Q} = \frac{\partial F}{\partial \boldsymbol{\sigma}}$.

6.2 Strain softening for material failure description

An important issue with the modeling of refractories is related to the proper simulation of the strain softening branch, which follows local failure of the material. A first problem is the determination of a proper ‘failure criterion’ for the considered materials, since different choices are possible. In the present work, two failure criteria are introduced:

1. A maximum value for the isotropic strength $p_{c_{max}}$ is determined for each considered material. In the hardening phase, p_c can grow according to the hardening rule (6.5) only until this limit value is reached. Analogously to p_c , $p_{c_{max}}$ depends on temperature according to Eq. (6.7), where the limit value of the isotropic strength at room temperature $p_{c_{max0}}$ replaces A^{p_c} . The procedure to numerically identify $p_{c_{max0}}$ is given detailed description in Sec. 6.4.
2. A spherical strain limiter criterion is proposed. Its formulation is illustrated in Sec. 6.3.

6.2.1 Material damage and softening

Sometimes it is desirable to stop the analysis immediately after the material reaches one of the predefined failure criteria (e.g. in pure compression or tension). In other cases, the material damage is particularly localized (e.g. cracks develop in a delimited portion of the material), so that global equilibrium of the loaded device is not compromised. If a numerical simulation of the latter example is performed, this should continue also after the material reaches its limits at some points, since the rest of the material could still be able to equilibrate the external loads.

This is for example the case of the *slide gate* simulation (see Sec. 6.5.2). During casting in foundry industries, it has been observed that cracks develop relatively quickly in the external part of the refractory plate. Nevertheless, the device can still operate for a long time after the initial local failure of the material. The stress is progressively redistributed to other parts of the plate, that must be replaced only once the damage reaches the central hole (see Fig. 6.19), since the metal flow can not anymore be properly confined.

The best way to simulate this kind of phenomena depends on the type of failure. Sometimes, the crack development is extremely localized and the size of the cracks is important. More often, the material fails for an high number of distributed micro-cracks.

In the former case, a computational formulation taking into account fracture mechanics, such as X-FEM, would be reasonable. However, these computations require the crack location to be known in advance and a precise set up to work properly. Their association to non-standard constitutive models complicates further the work flow of the simulation.

Otherwise, failure mechanisms induced by diffused damage or

distributed micro-cracks are better simulated through strain softening, inducing homogeneous stress reduction in the elements reaching the limit state. It must nevertheless be considered that sharp local decrease of stress can affect the convergence of the numerical analyses. Furthermore, the problem is very likely to become *mesh-dependent*, so that the size of the finite elements requires particular consideration.

Another possible option could be the iterative removal of the finite elements once the failure criterion is reached. This procedure is of difficult implementation and has the disadvantage that residual stresses in the failed material can not be taken into account. Nevertheless, the iterative removal of the elements is considered for future developments of the present work.

Strain softening represents a sufficiently precise and general way to obtain the desired effects in the context of industrial design of refractory devices. For this reason, its implementation is included in the proposed constitutive model. In the following, the softening formulation and the effects obtained in simple numerical simulations are presented.

6.2.2 Softening formulation

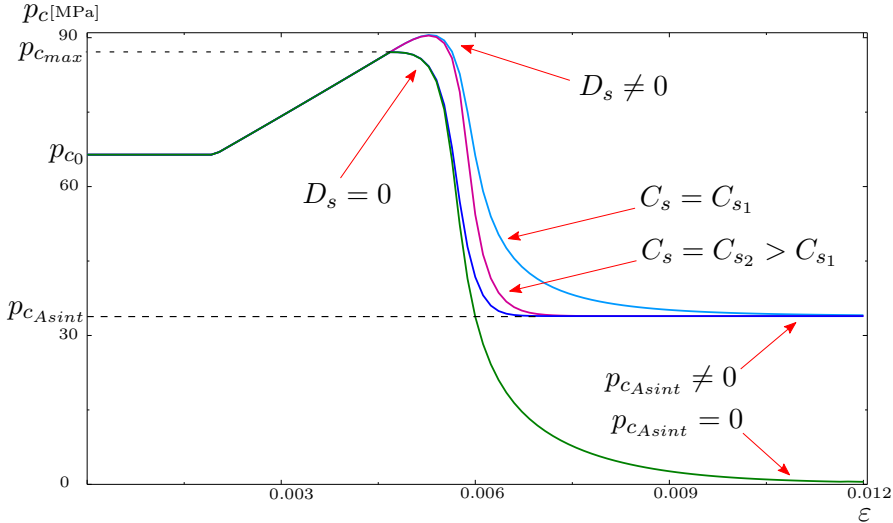


Figure 6.2: Influence of C_s , D_s and $p_{c_{Asint}}$ on p_c during softening: C_s regulates the curvature in the transition to the asymptotic value $p_{c_{Asint}}$ while D_s determines if hardening is immediately stopped once $p_{c_{max}}$ is reached.

The implemented softening formulation follows an incremental approach. In particular, before activating softening, it must be determined if the proposed limits, namely the limit strain (see Sec. 6.3) or $p_{c_{max}}$, have been reached or not in the previous analysis step.

In the former case, the value of the plastic multiplier λ is saved in the state variable λ_f and the material (in the considered Gauss point) assumes the ‘failed’ state, which is maintained until the end of the simulation.

By doing so, we accept a certain loss of precision, since big steps would inevitably delay the activation of softening, so that the saved λ_f is bigger than the ‘exact’ one.

In practice, time-steps are necessarily small when the material is close to failure, since the investigated numerical analyses exhibit high nonlinear behavior. However, an iterative procedure for the precise identification of λ_f could easily be implemented and will be considered in the future work.

If softening is activated, the hardening rule (6.5) is replaced with the following expression

$$p_c - p_{c_T} - \frac{(k_1)_T}{1 + (\delta)_T P(\boldsymbol{\varepsilon}_p)} P(\boldsymbol{\varepsilon}_p) + A_s |s^{B_s}| \left| \frac{(p_c - p_{c_{Asint}})}{p_{c_{max}}} \right|^{\frac{1}{C_s}} = 0, \quad (6.11)$$

where s is a parameter growing with λ and equal to 0 at the onset of softening, defined as

$$s = \frac{\lambda}{\lambda_f} - 1. \quad (6.12)$$

The coefficients A_s , B_s , C_s and $p_{c_{Asint}}$ are material constants defining the softening behavior.

It should be noted that in expression (6.11) the hardening behavior is still active but counterbalanced by the addition of softening. Thus, even with proper set up of the softening parameters, hardening will continue for a while after reaching the failure criteria, as shown in Fig. 6.2. This leads to a tangential trend of p_c and consequently of the stress, that is particularly helpful to ensure convergence of the simulation.

However, this particular behavior can be avoided by replacing the accumulated plastic strain $P(\boldsymbol{\varepsilon}_p)$ with the accumulated plastic strain *at failure* $P_f(\boldsymbol{\varepsilon}_p)$ in Eq. (6.11), thus obtaining

$$p_c - p_{c_T} - \frac{(k_1)_T}{1 + (\delta)_T P_f(\boldsymbol{\varepsilon}_p)} P_f(\boldsymbol{\varepsilon}_p) + A_s |s^{B_s}| \left| \frac{(p_c - p_{c_{Asint}})}{p_{c_{max}}} \right|^{\frac{1}{C_s}} = 0,$$

$$(6.13)$$

so that the third term can not continue to grow with the plastic strain and becomes only dependent on the temperature.

In the implemented constitutive model, the user can select the preferred behavior by setting the boolean D_s , which determines which expression between (6.11) and (6.13) is taken into account in the integration of the constitutive model.

Parameters A_s , B_s and C_s have peculiar effects on the softening behavior (see also Fig. 6.2):

- The parameter A_s regulates the ‘steepness’ of the softening curve. If too high values are chosen, the stress decreases very quickly, so that the convergence of the simulation might be affected. Otherwise, too low values can suppress softening effects.
- The parameter B_s influences the transition between hardening and softening behavior: $B_s = 1$ yields a linear transition, while higher values $B_s = \{2, 3\}$ correspond respectively to parabolic and cubic transition. The smoothness of the transition is therefore higher with values of B_s greater than 1.
- The parameter C_s determines how ‘quickly’ the value of p_c goes to the user defined value $p_{c_{Asint}}$, which determines the residual stress in the material after failure. High values of C_s yield to a quick decrease of p_c , particularly in the last part of the stress curve, as shown in Fig. 6.2.

6.3 Strain limiter criterion

The following strain limiter criterion was introduced as an additional failure condition for simulations involving the proposed thermo-elastoplastic model. Here, softening is activated when a defined maximum strain is reached.

The criterion is a variant of the well-known Rankine failure criterion, but defined in the strain space and in a way that there is no need of evaluating the eigenvalues of the strain tensor.

6.3.1 The Rankine strain limiter criterion

According to the maximum-tensile/compressive-strain criterion proposed by Rankine (see for instance Chen and Han, 1988 [42]),

failure in a brittle material takes place when the maximum or the minimum principal strain at a point inside the material reaches a value equal to the tensile ε_t or compressive strain ε_c (the latter taken in absolute value) as found in an extension or compression uniaxial deformation test.

Rankine failure surface

The equations for the Rankine failure surface can be written as

$$\varepsilon_1 = -\varepsilon_c, \quad \varepsilon_2 = -\varepsilon_c, \quad \varepsilon_3 = -\varepsilon_c, \quad (6.14)$$

in case of compression, and

$$\varepsilon_1 = \varepsilon_t, \quad \varepsilon_2 = \varepsilon_t, \quad \varepsilon_3 = \varepsilon_t, \quad (6.15)$$

in case of tension, which result in six planes perpendicular to the $\varepsilon_1, \varepsilon_2, \varepsilon_3$ axes.

In the three-dimensional strain space, these equations define a cube with center shifted along the diagonal by a length depending on the difference between the values ε_t and ε_c , so that the criterion can be written as

$$F(\boldsymbol{\varepsilon}, \varepsilon_t, \varepsilon_c) = \text{Max}\{-\varepsilon_{\min} - \varepsilon_c, \varepsilon_{\max} - \varepsilon_t\}, \quad (6.16)$$

so that $F < 0$ corresponds to an admissible strain state, while $F = 0$ corresponds to failure.

Spherical failure surface

A similar approach to the Rankine criterion is now introduced, so that, instead than a cubical, a spherical limit surface is considered.

We assume that failure takes place when the maximum or the minimum uniaxial strain at a certain point of a material reaches a value equal to the uniaxial deformation in extension ε_t or in compression ε_c .

We consider a sphere of radius R , centered on the diagonal of the strain space at the point $\hat{\varepsilon}$, so that its equation is described as

$$F(\boldsymbol{\varepsilon}, \hat{\varepsilon}, R) = \sqrt{(\varepsilon_1 - \hat{\varepsilon})^2 + (\varepsilon_2 - \hat{\varepsilon})^2 + (\varepsilon_3 - \hat{\varepsilon})^2} - R. \quad (6.17)$$

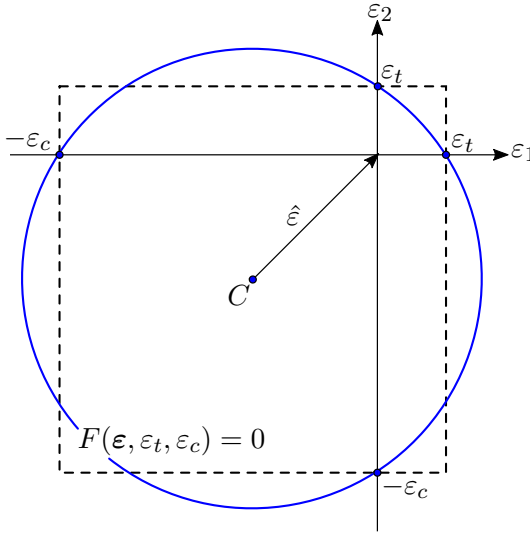


Figure 6.3: Two-dimensional representation of the proposed strain limiter criterion (continuous line) and Rankine criterion (dashed line).

In tensorial notation, the first term of equation (6.17) can be written as

$$|\boldsymbol{\varepsilon} - \hat{\boldsymbol{\varepsilon}}\mathbf{I}| \quad (6.18)$$

where \mathbf{I} is the identity tensor and $|\cdot|$ denotes the norm. Accordingly, equation (6.18) becomes

$$\sqrt{(\boldsymbol{\varepsilon} - \hat{\boldsymbol{\varepsilon}}\mathbf{I}) \cdot (\boldsymbol{\varepsilon} - \hat{\boldsymbol{\varepsilon}}\mathbf{I})} = \sqrt{\boldsymbol{\varepsilon} \cdot \boldsymbol{\varepsilon} - 2\hat{\boldsymbol{\varepsilon}} \text{tr} \boldsymbol{\varepsilon} + 3\hat{\boldsymbol{\varepsilon}}^2}. \quad (6.19)$$

By inserting the last expression in equation (6.17) we obtain

$$F(\boldsymbol{\varepsilon}, \hat{\boldsymbol{\varepsilon}}, R) = \sqrt{\boldsymbol{\varepsilon} \cdot \boldsymbol{\varepsilon} - 2\hat{\boldsymbol{\varepsilon}} \text{tr} \boldsymbol{\varepsilon} + 3\hat{\boldsymbol{\varepsilon}}^2} - R, \quad (6.20)$$

which defines the failure criterion in the strain space as a function of the two geometrical parameters R and $\hat{\boldsymbol{\varepsilon}}$. To obtain the expression of the criterion as a function of the limit uniaxial strain values, ε_c and ε_t , we impose the conditions

$$\begin{cases} F(\boldsymbol{\varepsilon} = \boldsymbol{\varepsilon}_t, \hat{\boldsymbol{\varepsilon}}, R) = 0 \\ F(\boldsymbol{\varepsilon} = \boldsymbol{\varepsilon}_c, \hat{\boldsymbol{\varepsilon}}, R) = 0 \end{cases} \quad (6.21)$$

where $\boldsymbol{\varepsilon}_t$ and $\boldsymbol{\varepsilon}_c$ are defined as

$$\boldsymbol{\varepsilon}_t = \begin{pmatrix} \varepsilon_t & 0 & 0 \\ 0 & 0 & 0 \\ 0 & 0 & 0 \end{pmatrix}, \quad \boldsymbol{\varepsilon}_c = \begin{pmatrix} -\varepsilon_c & 0 & 0 \\ 0 & 0 & 0 \\ 0 & 0 & 0 \end{pmatrix} \quad (6.22)$$

Inserting (6.22) in the system (6.21) and taking into account equation (6.20) yields

$$\begin{cases} \sqrt{\varepsilon_t^2 - 2\hat{\varepsilon}\varepsilon_t + 3\hat{\varepsilon}^2} - R = 0 \\ \sqrt{\varepsilon_c^2 + 2\hat{\varepsilon}\varepsilon_c + 3\hat{\varepsilon}^2} - R = 0. \end{cases} \quad (6.23)$$

Therefore, the parameters $\hat{\varepsilon}$ and R can be written as functions of ε_t and ε_c in the form

$$\hat{\varepsilon} = \frac{(\varepsilon_t - \varepsilon_c)}{2} \quad (6.24)$$

and

$$R = \sqrt{\frac{3(\varepsilon_t - \varepsilon_c)^2}{4} + \varepsilon_c(\varepsilon_t - \varepsilon_c) + \varepsilon_c^2}. \quad (6.25)$$

Inserting the expressions (6.24) and (6.25) in equation (6.20) yields the expression of the failure criterion in the strain space as a function of the uniaxial limit strains

$$F(\boldsymbol{\varepsilon}) = \sqrt{-(\varepsilon_t - \varepsilon_c) \operatorname{tr} \boldsymbol{\varepsilon} + \frac{3(\varepsilon_t - \varepsilon_c)^2}{4} + \boldsymbol{\varepsilon} \cdot \boldsymbol{\varepsilon} - \sqrt{\frac{3(\varepsilon_t - \varepsilon_c)^2}{4} + \varepsilon_c(\varepsilon_t - \varepsilon_c) + \varepsilon_c^2}} \quad (6.26)$$

If we consider an extension/compression test on a cylindric specimen, the sample deforms uniaxially (e.g. $\varepsilon_1 \neq 0$, $\varepsilon_2 = 0$, $\varepsilon_3 = 0$) only if radial strain is prevented. For this reason, especially in extension, tests to identify the uniaxial limit strain parameters are commonly difficult to perform.

Otherwise, if the specimen is free to deform radially and maximum strains in both longitudinal and radial direction are measured, a different expression of the failure criterion can be found by modifying equations (6.22) as

$$\boldsymbol{\varepsilon}_t = \begin{pmatrix} \varepsilon_{t1} & 0 & 0 \\ 0 & \varepsilon_{t2} & 0 \\ 0 & 0 & \varepsilon_{t3} \end{pmatrix}, \quad \boldsymbol{\varepsilon}_c = \begin{pmatrix} \varepsilon_{c1} & 0 & 0 \\ 0 & \varepsilon_{c2} & 0 \\ 0 & 0 & \varepsilon_{c3} \end{pmatrix} \quad (6.27)$$

where ε_{t2} , ε_{t3} , ε_{c2} , ε_{c3} , define the limit strain in radial direction.

It is to note that, in this case, the values in matrix $\boldsymbol{\varepsilon}_t$ and $\boldsymbol{\varepsilon}_c$ are provided with their sign.

Equations (6.24) and (6.25) become respectively

$$\hat{\varepsilon} = \frac{(\varepsilon_t \cdot \varepsilon_t - \varepsilon_c \cdot \varepsilon_t)}{2(\text{tr } \varepsilon_t - \text{tr } \varepsilon_c)} \quad (6.28)$$

and

$$R = \sqrt{-\frac{(\varepsilon_t \cdot \varepsilon_t - \varepsilon_c \cdot \varepsilon_c) \text{tr } \varepsilon_c}{\text{tr } \varepsilon_t - \text{tr } \varepsilon_c} + \frac{3(\varepsilon_t \cdot \varepsilon_t - \varepsilon_c \cdot \varepsilon_c)^2}{4(\text{tr } \varepsilon_t - \text{tr } \varepsilon_c)^2} + \varepsilon_c \cdot \varepsilon_c}. \quad (6.29)$$

The expression of failure criterion in the strain space in its more general form yields

$$F(\varepsilon, \varepsilon_t, \varepsilon_c) = \sqrt{-\frac{(\varepsilon_t \cdot \varepsilon_t - \varepsilon_c \cdot \varepsilon_c) \text{tr } \varepsilon}{\text{tr } \varepsilon_t - \text{tr } \varepsilon_c} + \frac{3(\varepsilon_t \cdot \varepsilon_t - \varepsilon_c \cdot \varepsilon_c)^2}{4(\text{tr } \varepsilon_t - \text{tr } \varepsilon_c)^2} + \varepsilon \cdot \varepsilon - \sqrt{-\frac{(\varepsilon_t \cdot \varepsilon_t - \varepsilon_c \cdot \varepsilon_c) \text{tr } \varepsilon_c}{\text{tr } \varepsilon_t - \text{tr } \varepsilon_c} + \frac{3(\varepsilon_t \cdot \varepsilon_t - \varepsilon_c \cdot \varepsilon_c)^2}{4(\text{tr } \varepsilon_t - \text{tr } \varepsilon_c)^2} + \varepsilon_c \cdot \varepsilon_c}. \quad (6.30)$$

6.4 Material parameters identification

Refractories are characterized by a wide range of compositions, leading to extremely variable mechanical and thermal responses. An efficient procedure to obtain the material parameters appearing in the governing equations from experimental results is important to obtain realistic results in the numerical simulations. This procedure should be sufficiently general to allow an easy characterization of all refractory materials. This procedure has been developed and applied with success to several compositions. In the following, its main steps are described in detail.

6.4.1 Temperature dependent elastic and thermal constants

As anticipated in Sec. 6.1.1 different values of the elastic modulus $E(T)$ are obtained through a series of uniaxial tests at different temperatures. Its expression in the implemented constitutive model is obtained through the polynomial (6.4), whose parameters are passed to the constitutive model as material constants.

The identification of the cited parameters is carried out by polynomial regression in Wolfram Mathematica.

The values of thermal expansion, thermal conductivity and specific heat also depend on temperature and are obtained directly from specific experimental tests.

Only the value of the thermal expansion α_T needs to be passed directly to the subroutine UMAT for the integration of the constitutive model, while Abaqus requires thermal conductivity and specific heat to solve the heat conduction equations.

6.4.2 BP yield function parameters

One of the most challenging tasks in the identification of the parameters for the proposed constitutive model consists in the determination of the parameters governing the shape of the BP yield function. Extremely different shapes of the BP yield function, especially in the meridian plane, have been identified for different refractory materials.

The procedure can be divided into three parts, respectively aiming at the identification of:

- (a) The BP yield function parameters M , m , α , c and p_c at room temperature
- (b) The evolution of p_c depending on temperature
- (c) The value of $p_{c_{max}}$ at room temperature

The shape of the yield function is obtained by identifying the onset of plasticity in a series of experiments at room temperature. In particular, the following experimental tests are usually performed:

- Bi-tensile test
- Uniaxial tensile test
- Three points bending
- Four points bending
- Brazilian test
- Shear test
- Uniaxial compression test
- Triaxial compression tests with different pressure ratios
- Isotropic compression test

These tests lead to a collection of yield points, defining the shape of the BP surface in the $q - p$ plane (see Fig. 6.5). The values of M , m , α , c , p_c are therefore obtained by minimizing the

discrepancy between the BP yield function and these experimental points using the method of least squares.

At this point, it is necessary to identify the thermal evolution of p_c by performing a series of experimental tests at high temperature. Only two tests can currently be performed at high temperature, namely the uniaxial compression test and the Brazilian test. In both cases, heat in the sample is generated through electromagnetic induction as shown in Fig. 6.4.

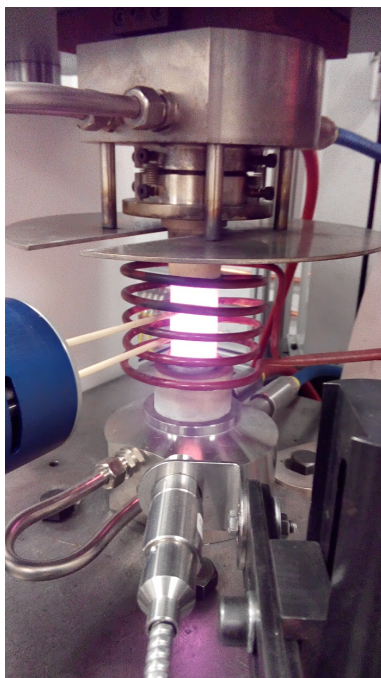


Figure 6.4: Uniaxial compression test at high temperature: the sample is heated through electromagnetic induction.

The tests make available two points on the BP yield surface for each considered temperature, which allow the calculation of the corresponding values of p_c , while c is calculated according to equation (6.6).

The only change of these parameters does not influence the shape of the yield surface, while its size is indeed modified.

It should be noted that the constant shape of the yield function is an assumption that should be experimentally confirmed. If future investigations will detect shape modifications induced by temperature changes, an evolution of the BP yield function shape

depending on temperature could be implemented in a similar way as proposed in Sec. 7.1.1.

Figures 6.5 and 6.6 show respectively the BP yield function and p_c at selected temperatures $T = \{20, 200, 400, 600, 800, 1000\}$ °C for one of the refractory materials considered in this study.

This case is quite unusual for the considered refractories. The material initially shows an increase of p_c , so that higher temperature lead to higher yield strength. After reaching 400°C p_c begins to decrease. As shown in Fig. 6.6, the proposed expression (6.7) for the evolution of p_c depending on temperature is in this case unable to fit adequately well the identified values.

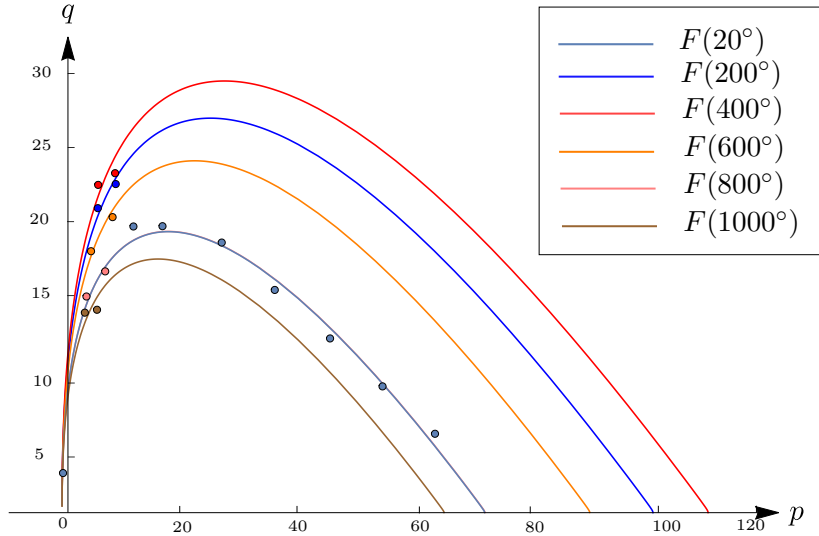


Figure 6.5: Evolution of the BP yield surface depending on temperature: the yield surface at room temperature is identified with a series of experimental tests, while only two (uniaxial compression and Brazilian tests) are performed at high temperature.

The identification of $p_{c_{max}}$ at room temperature follows the same principle described previously for the calibration of p_c depending on the temperature: the yield function shape is kept constant from the onset of plasticity until beginning of softening (corresponding to $p_c = p_{c_{max}}$). Since the identification is carried out at room temperature, the complete series of experimental tests could be performed in order to identify the precise shape of the *ultimate* BP yield function F_{ult} . At present, the procedure has not been carried out yet but is planned for future developments of the

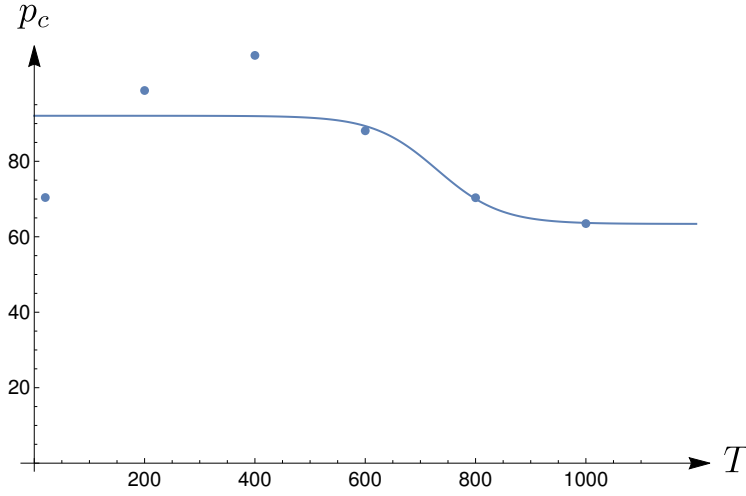


Figure 6.6: Identified value of p_c depending on temperature. This case represents an exception for the considered refractory materials. When increasing the temperature, the material initially becomes more resistant. After reaching 400°C the yield strength of the material starts to decrease. The proposed expression (6.7) is in this case unable to follow properly the identified values of p_c , at least in the first part.

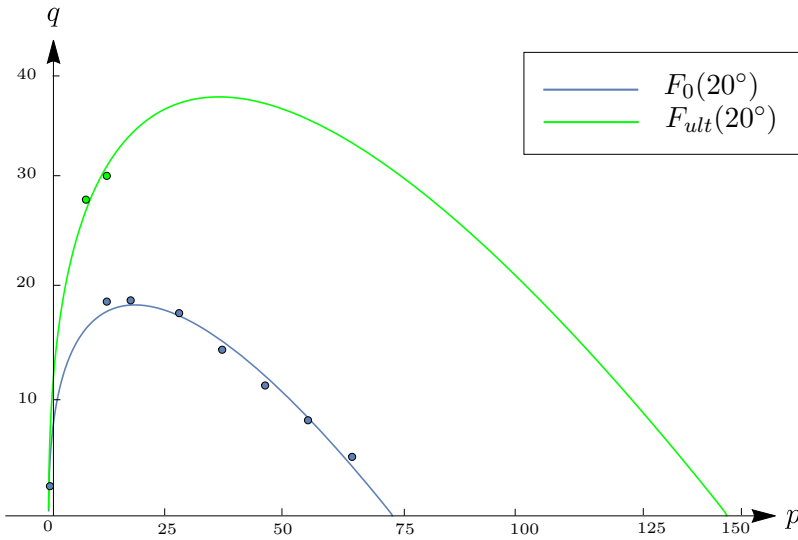


Figure 6.7: BP yield function at the onset of plasticity F_0 and ultimate yield function F_{ult} defining the beginning of softening behavior.

constitutive model.

As already mentioned in Sec. 6.2, the relationship between $p_{c_{max}}$ and temperature is defined analogously as for p_{c_T} in expression (6.7), where A^{p_c} is replaced by the value of $p_{c_{max}}$ at room temperature.

6.4.3 Hardening rule parameters through multi-objective optimization

The identification of the parameters required by the temperature dependent hardening rule are identified through inverse analysis. The main steps and the results of the optimization procedure are summarized in the following.

The inverse problem can be posed in the following form:

- Uniaxial compressive tests at n different temperatures (in this example $T = \{200, 400, 600, 800, 1000, 1200\}$ °C) lead to n values of maximum uniaxial stress σ_{max} and n values of maximum uniaxial strain ε_{max} . According to the procedure described in the previous section, at each temperature a precise value of $p_{c_{max}}$ is identified.
- The values governing the strain hardening rule and its dependence on the temperature (see Eqs. (6.5), (6.8) and (6.9)), namely A^{k_1} , B^{k_1} , C^{k_1} , $T_0^{k_1}$, δ_0 , T_0^δ and T_F , are unknown and must be determined.

The most efficient way to perform the inverse analysis is to couple a FEM simulation with the developed constitutive model (UMAT subroutine) to the powerful optimization algorithms available in Dakota [16].

The FE analysis considers a single three-dimensional finite element, where the maximum experimental strain ε_{max} and associated temperature are imposed as boundary conditions. At the end of the computation, the reached values of p_c and σ are respectively compared to $p_{c_{max}}$ and σ_{max} by calculating the two objective functions

$$f_{p_c} = \frac{|p_c - p_{c_{max}}|}{p_{c_{max}}} 100, \quad f_\sigma = \frac{|\sigma - \sigma_{max}|}{\sigma_{max}} 100, \quad (6.31)$$

at each considered temperature. The considered multi-objective optimization problem has therefore $2n$ objective functions to minimize and seven parameters to identify.

The optimization problem has been successfully solved with an hybrid procedure (see Sec. 4.1.3), by combining the genetic algorithm *moga* (multi-objective genetic algorithm) and the heuristic method *pattern-search* (see Sec. 4.1.2).

The parameter space is first explored using *moga*. However, it is computationally not efficient to persist until complete convergence of this method. Therefore, after a reasonably high number of iterates, the genetic algorithm already found a limited set of promising solutions that can be further improved locally by *pattern-search*, thus speeding up the convergence rate.

Zero order optimization methods have been preferred for this optimization process due to the high noisiness of the responses: some combinations of the material parameters lead to lack of convergence of the simulation, and in this case the gradients of the objective functions with respect to the design variables would be inaccurate or undefined.

In the considered case of six temperature values $T = \{200, 400, 600, 800, 1000, 1200\}$ °C, twelve independent objective functions must be simultaneously minimized.

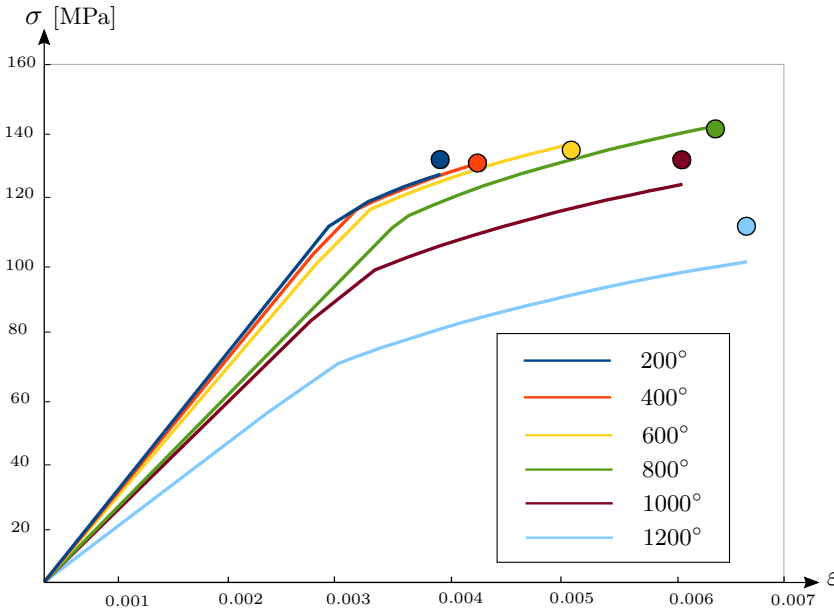


Figure 6.8: Numerical stress-strain curves at different temperatures for uniaxial compressive tests with the identified parameters: the dots represent the maximum stresses σ_{max} measured during the experimental tests.

Figures 6.8 and 6.9 show the results of the optimization procedure, which are summarized in Table 6.1. The parameter identification led to particularly accurate results for several analyzed materials and can therefore be considered of general validity.

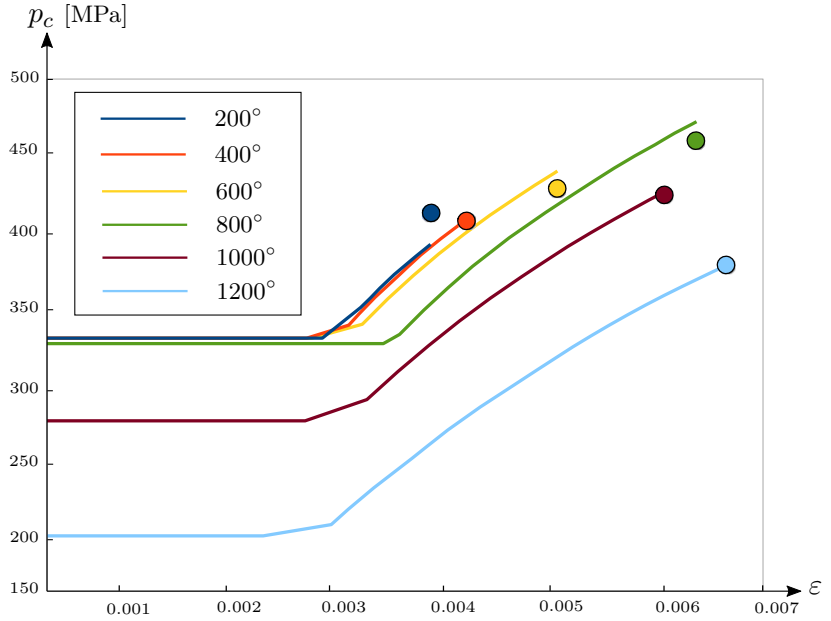


Figure 6.9: Evolution of the isotropic strength p_c in the simulation of uniaxial compressive tests with the identified parameters: the dots represent the values of $p_{c_{max}}$ identified from the experimental tests according to the procedure described in Sec. 6.4.2.

The parameter identification takes into account only the yield points (in the manner described in Sec. 6.4.2), the maximum values of stress σ_{max} and of isotropic strength $p_{c_{max}}$, so that the stress growth is feasible along multiple paths.

The experimental tests make available the complete stress-strain curves at the prescribed temperatures, which could also be taken into account in the optimization in order to obtain more precise results. This improvement will be considered in future developments of the identification procedure.

Temperature [°C]		ε [10^{-3}]	p_c [MPa]	σ [MPa]
200	Experiment	3.75	407.81	130.35
	Simulation		387.00	126.02
400	Experiment	4.11	402.73	129.28
	Simulation		404.73	129.44
600	Experiment	4.99	424.43	133.45
	Simulation		437.12	135.48
800	Experiment	6.35	457.33	139.86
	Simulation		470.84	140.94
1000	Experiment	6.04	420.27	130.40
	Simulation		422.97	122.93
1200	Experiment	6.65	372.23	109.91
	Simulation		372.91	98.97

Table 6.1: Values of stress σ , strain ε and isotropic strength p_c in numerical simulations and experimental tests at the considered temperatures.

6.4.4 Strain limiter criterion

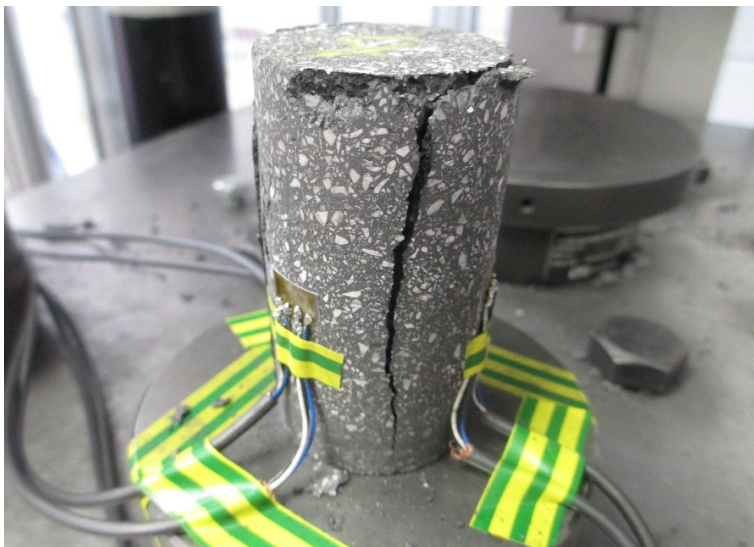


Figure 6.10: Cracked sample used in an uniaxial compression test and strain gages for the measurement of the transversal strains.

The parameters governing the strain limiter criterion described in Sec. 6.3, namely the maximum longitudinal strain ε_1 and transver-

sal strains $\varepsilon_2 = \varepsilon_3$, can be identified through uniaxial compressive and tensile tests. The transversal deformation of the sample has been measured with three strain gages, placed respectively at 120° , 240° and 360° around the specimen as shown in Fig. 6.10.

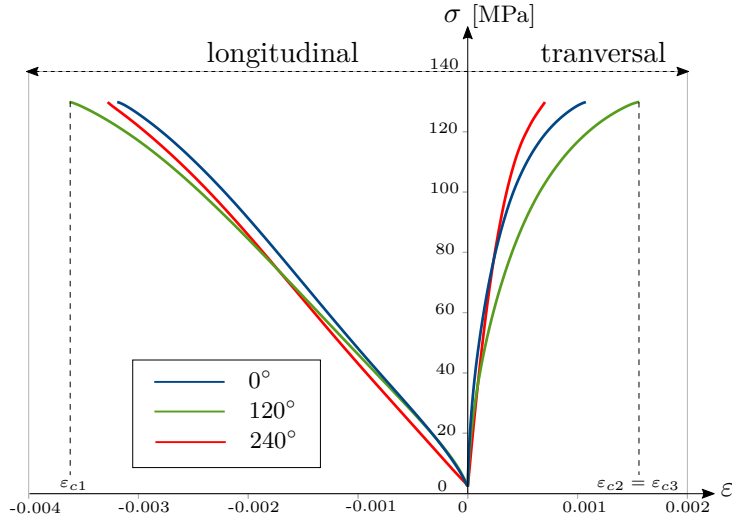


Figure 6.11: Stress strain curves and associated transversal/longitudinal strain in uniaxial compression test. The angles refer to the position of the strain gages around the specimen.

The measurement of the transversal deformations at high temperature is not possible with conventional strain gages, therefore the ratio between longitudinal and transversal deformations is usually kept constant.

6.5 Exploitation of the thermo-elasto-plastic model to describe the behavior of refractories under working conditions

The proposed thermo-elasto-plastic constitutive model has been employed in the simulation of refractory devices. In addition to its numerical precision, already confirmed by the tests described in Ch. 3, the computational efficiency of the implemented code is an important parameter to evaluate. All performed simulations have shown acceptable running times and are for this reason suitable for efficient industrial design of refractories.

The results of the thermo-mechanical analyses show accordance

with the observed behavior of the devices under working conditions. A selection of the performed studies is reported in the following. These outcomes pave the way to more complex numerical analyses involving virtual-prototyping and shape optimization.

6.5.1 Maximum bending load of a steel flow stopper

A series of experimental bending tests at high-temperature has been performed on steel flow stoppers. The tests identified the bending failure loads of these refractory devices at different temperatures, which have been compared with the results of numerical simulations employing the proposed constitutive model.

Experimental set-up

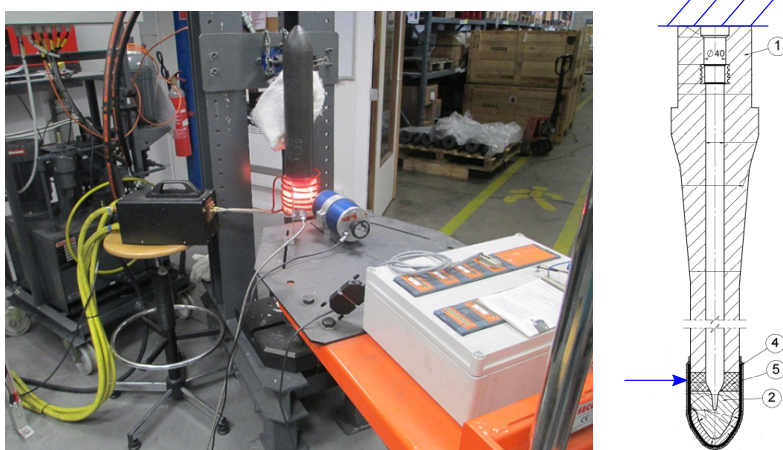


Figure 6.12: Experimental set-up of the bending tests and longitudinal section of the steel flow stopper with the applied boundary conditions.

The refractory device is first clamped at one end as shown in Fig. 6.12. Heat in the central part of the steel flow stopper is then generated through electromagnetic induction employing the specially designed solenoid shown in Fig. 6.13. After temperature stabilization, a concentrated load is applied close to the top of the tube in order to impose bending. The force is increased until failure of the refractory device. The test has been performed at room temperature ($T = 20^{\circ}C$) and at two selected high temperatures ($T = 400, 1000^{\circ}C$).

During the test, precise measurements have been made for the applied force, but not for the displacements, since the pushing

head locally penetrated the surface of the material, leading to over estimated values of deflection. Nevertheless, the measured data allow a precise determination of the failure loads.

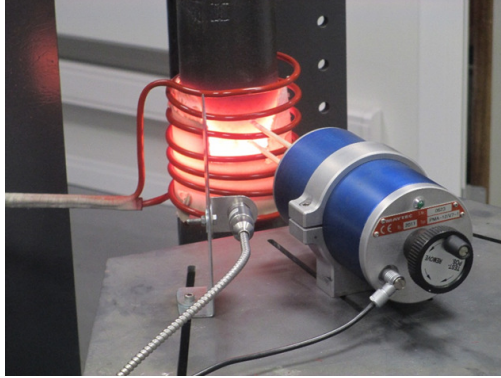


Figure 6.13: Electromagnetically induced heat in the middle part of the refractory steel flow stopper.

Sequentially coupled thermal-stress analysis

A numerical counterpart of the bending experiment has been prepared in Abaqus FEA environment. By exploiting symmetry, only half of the steel flow stopper needs to be modeled. Consequently, half of the applied force is considered, as well.

A ‘sequentially-coupled’ thermal-stress analysis is carried out. This procedure first computes the transient temperature field by solving the heat conduction problem. At each time step the calculated temperature field is then passed to the mechanical analysis, which takes it into account for the computation of the displacement field. In this way, the thermo-mechanical coupling is ‘one-way’: temperature influences the mechanical response, but displacements do not affect the temperature.

As a result, piezocaloric effect and plastic heating (see Eqs. (2.23) and (2.24)) are neglected. Considered the small influence of the cited phenomena and the maximum temperature reached during the test, this approach appears to be reasonable.

The temperature increment generated through electromagnetic induction is simulated by heat flux in the middle part of the device. Analogously to the experimental test, the mechanical load is increased linearly once the temperature reaches a constant value.

Figures 6.14 and 6.15 show the results of the numerical simulations. It should be noted that, while the maximum plastic strain

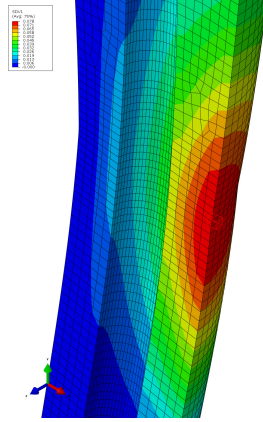


Figure 6.14: Plastic strain distribution in the middle part of the refractory device.

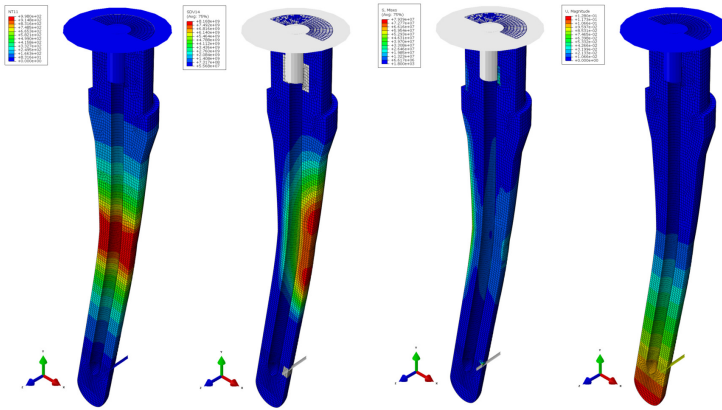


Figure 6.15: From left to right: temperature T , isotropic compressive yield stress p_c , Von Mises stress q and displacement in x direction u_x at the end of the numerical analysis.

is reached in the center of the heated part of the refractory device (Fig. 6.14), the value of p_c (SDV14) is lower at high temperature (Fig. 6.15 second from left). This effect is due to thermal softening according to Eq. (6.7).

Failure of the device is assumed when, due to plastic hardening, the first element of the mesh reaches the value of $p_{c_{max}}$. The parameters governing the evolution of $p_{c_{max}}$ depending on temperature, so as all other material parameters governing the response of the presented constitutive model, have been identified independently from the current numerical analysis in the manner described in Sec. 6.4. Therefore, this comparison between experimental and numerical results represents an important test to ensure that the identification procedure provides parameters of general validity.

The comparison between numerical and experimental break loads is shown in Fig. 6.16 for the three considered temperatures. The numerical results appear to be in the same order of magnitude of the experimentally measured maximum loads. The experimental results show higher dependence on the temperature, which affects negatively the resistance to bending. While comparing the values, it must be considered that the usual variance of the break load has been calculated around 12%. The numerical results are therefore still within a valid range.

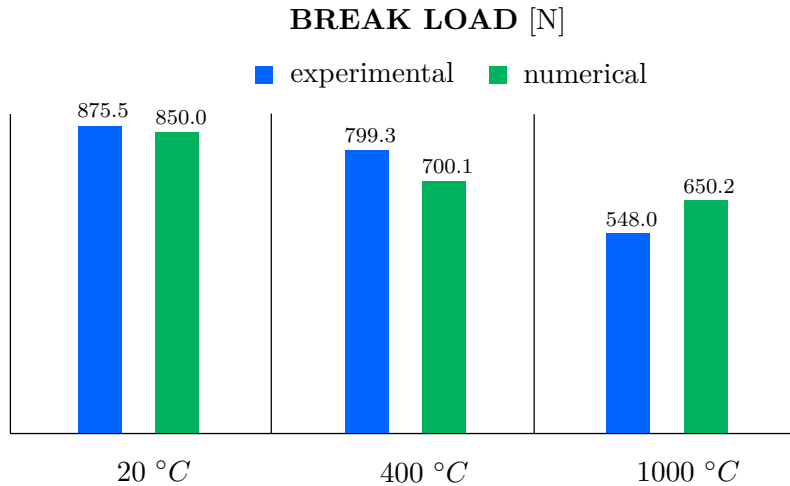


Figure 6.16: Comparison of experimental and numerical values of break load in the bending test of the refractory steel flow stopper.

6.5.2 Slide gate thermal-stress analysis

One of the most important devices for the molten steel industry is the so called ‘slide gate’, which is shown in Fig. 6.17. This device is employed to control the liquid metal flow during the casting processes in foundry industries. The refractory composing the plate is subject to extremely high thermal shock, wear and mechanical loads. For this reason, the refractory must regularly be replaced. Significant research studies focus on possible design improvements for this device.

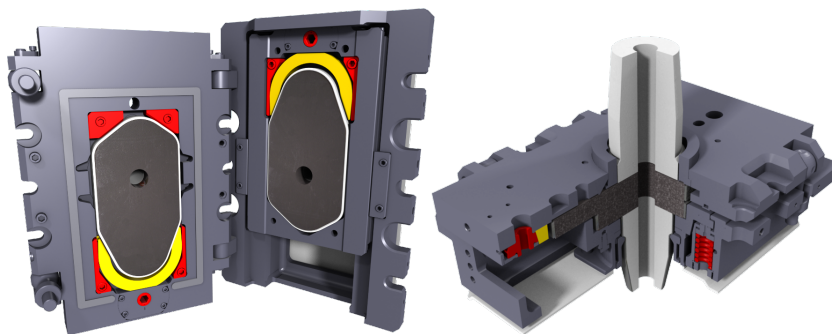


Figure 6.17: A slide gate used for confinement and regulation of molten metal flow during casting.

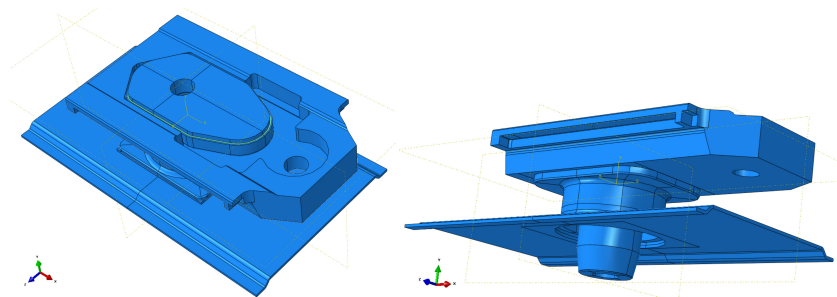


Figure 6.18: Numerical model of the slide gate composed of steel and refractory material.

Modelling

The device is composed of different types of steel and refractory materials. Two refractories with different features respectively compose the plate and the nozzle (see Fig. 6.19). Special focus is

given to the plate, which is subject to high wear and thermal shock, and for this reason designed to be particularly resistant.

In the performed simulation, the aim is to identify the temperature and displacement fields during the casting process, and in the cooling phase, after the metal flow is completed and the temperature in the device decreases.

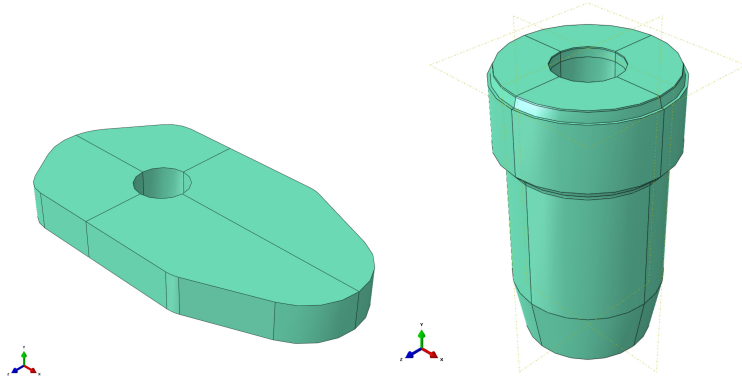


Figure 6.19: Plate and nozzle, composed of different refractory materials.

The parameters governing the constitutive equations have been identified in the manner reported in 6.4 for each refractory material considered in the simulation.

A ‘sequentially-coupled’ thermal-stress analysis is carried out. After the end of the thermal simulation, the mechanical response is computed while taking into account the temperature field at each time step.

As already mentioned in 6.5.1, temperature changes due to elastic or plastic strain are neglected with this kind of computation. Considered the maximum temperature reached by the refractory plate ($T = 1500^{\circ}C$), this approach is certainly appropriate.

In order to perform the heat transfer analysis, it is necessary to define the convection parameters and the temperature of the fluids (liquid steel and air) coming in contact with the structure. The parts coming in direct contact with the molten metal are subject to higher convection, that is modeled with higher film coefficient h (also called convection coefficient). When the structure cools down these parameters change according to the lower convection coefficient of the air.

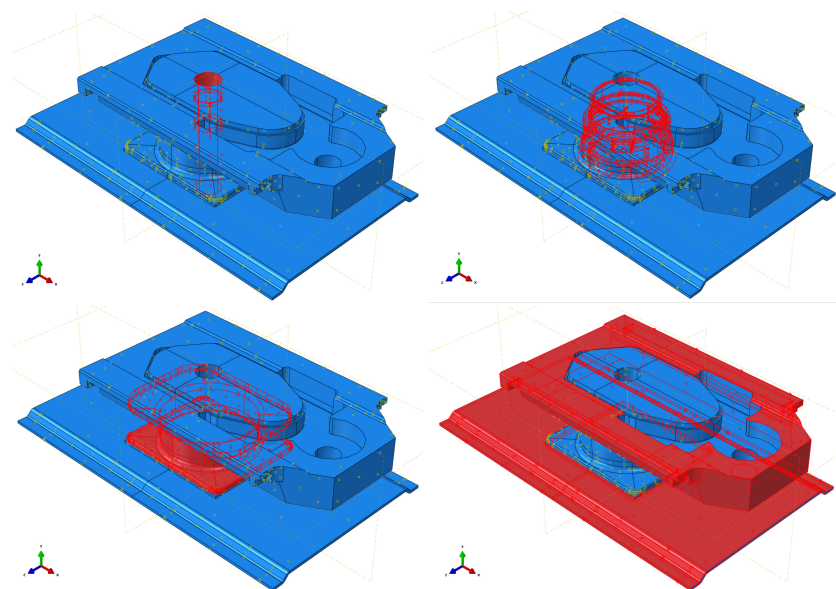


Figure 6.20: Interaction surfaces in the thermo-mechanical simulation. Different convection coefficients are taken into account for molten steel and air.

This modelization can be performed with Abaqus by using the interaction module and setting specific convection parameters on user defined surfaces.

Figure 6.20 shows the different surfaces modeled in the simulation, where thermal conductance and Coulomb friction coefficients are considered in case of contact.

Postprocessing

The post-processing phase shows clearly how, during the casting process, the temperature distribution assumes a circular shape around the area directly in contact with the molten steel, while the rest of the structure increases slowly its temperature (see Fig. 6.21). Due to the high film coefficient assumed in the analysis during the casting process, the maximum temperature around the hole in the refractory plate reaches $1519\text{ }^{\circ}\text{C}$ (see Fig. 6.24 top-right).

During the cooling process the temperature distribution in the refractory plate appears asymmetric (see Fig. 6.24 bottom-right). The temperature field along the X axis is both influenced by the asymmetry of the device and higher air convection from the bottom-lateral surfaces. The asymmetric thermal distribution along Z-axis

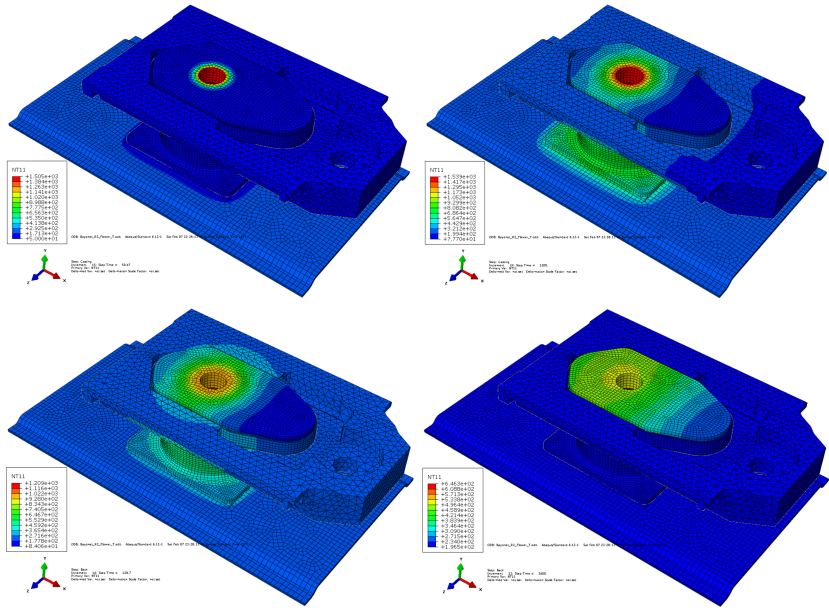


Figure 6.21: Temperature distribution in Slide gate at the beginning of the casting process.

is due to the shape of the object, which is asymmetric also with respect to X-Y plane, even though this detail is difficult to note in Fig. 6.24.

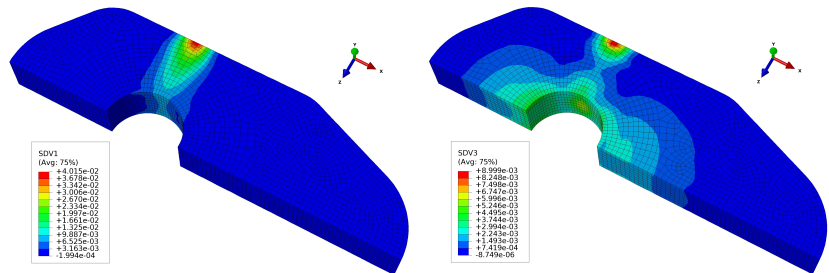


Figure 6.22: Plastic deformation in the refractory plate during the casting process: the results show higher values of inelastic deformation in the external part of the plate, where crack development is typically observed in the real device.

The high temperature gradients induce thermal expansion and mechanical stresses in the refractory plate, which is constrained externally by the steel structure and therefore unable to expand freely. As a consequence, the yield strength of the refractory ma-

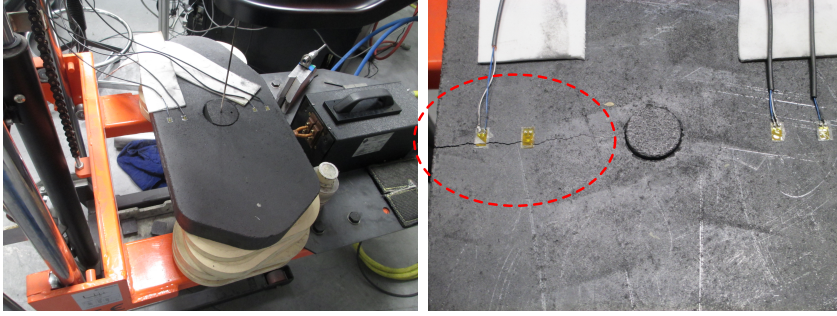


Figure 6.23: Crack development during an experimental test on the refractory plate. The temperature of the material inside the hole is increased, in order to simulate the liquid steel flow.

material is reached and inelastic deformation is generated.

Plastic strain is particularly high in the external part of the plate, as shown in Fig. 6.23. During casting processes in foundry industries, the refractory plate often develops cracks starting from the same location. Thus, the simulation shows the capability of precise prediction of the observed damage mechanisms.

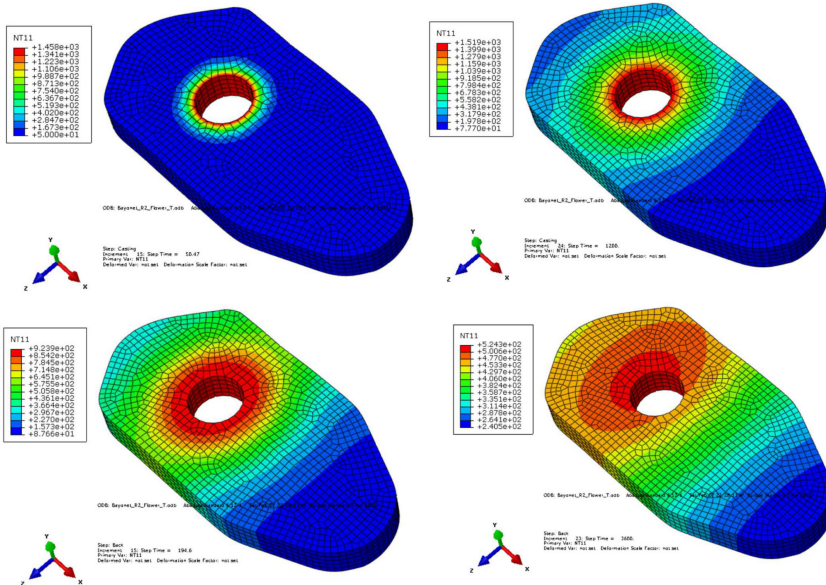


Figure 6.24: Temperature distribution in refractory plate at the beginning (left) and at the end (right) of the casting process.

6.5.3 VISO submerged pouring tubes thermal-stress analysys

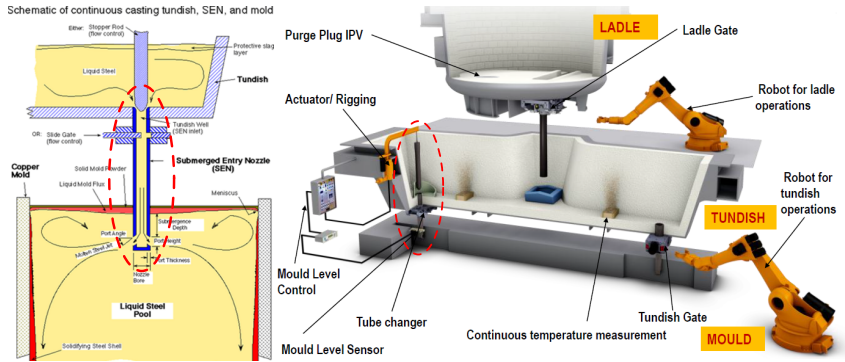


Figure 6.25: Schematic of continuous tundish casting, SEN and mold in a steel industry.

The VESUVIUS Sub-Entry Nozzle (SEN) is a one-piece ceramic tube manufactured from isostatically pressed alumina graphite (VISO). As shown in Fig. 6.25, the molten metal flows through the tube, the end of which is submerged in the liquid material.

The goal of this simulation is to properly describe the stress and temperature fields during the casting process with a thermal-stress simulation.

Modelling

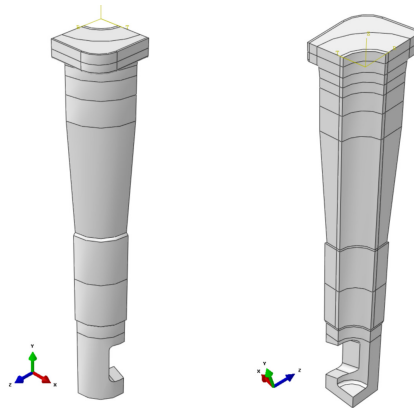


Figure 6.26: Modelization of the refractory VISO - tube.

Thanks to the symmetry of the object and of the heat flux, only a quarter of the VISO-tube needs to be represented in the Abaqus numerical model, which is shown in Fig. 6.26.

During the molten metal flow, the refractory pouring tube is entirely supported by its upper, wider part. In some rare cases, local cracks can develop in this area, so that this phenomenon needs to be properly investigated. In order to model the reaction

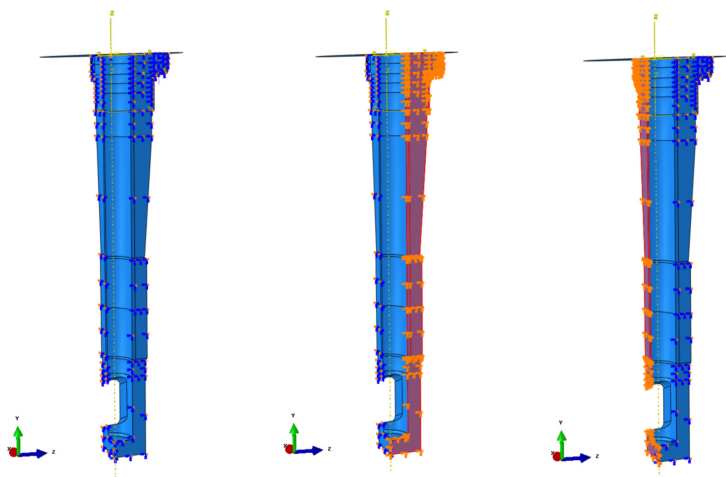


Figure 6.27: Assigned symmetric boundary conditions for the thermo-mechanical simulation of the pouring tube.

forces acting on the top of the tube, a mechanical load (pressure) with magnitude of 4.2 MPa is applied on the bottom surface of the supporting area, as shown in Fig. 6.28.

The temperature flux induced by the molten steel flow is modeled using Abaqus interaction module. On the surfaces directly in contact with the liquid steel, namely the inner part of the tube and its bottom external surface, a very high convection coefficient is assumed in order to describe properly the heat transfer effects. For this surfaces the sink temperature is assumed equal to 1550 °C.

On the surfaces not in direct contact with the liquid metal, such as the external upper surface of the tube, the convection is due to the action of the air. In this case, lower convection coefficient and sink temperature ($T = 50$ °C) are assumed. Figure 6.29 shows the interaction surfaces considered in the numerical model.

The constants needed by the proposed constitutive model have been identified for the particular refractory material according to

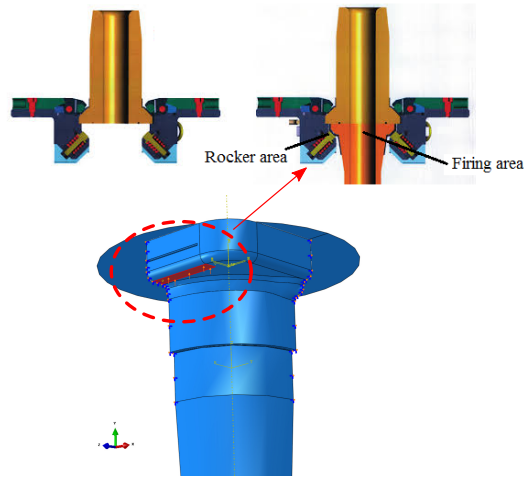


Figure 6.28: Applied pressure of 4.2 MPa (1300 Kg) on the highlighted surface, in order to simulate the blocking mechanism of the nozzle.

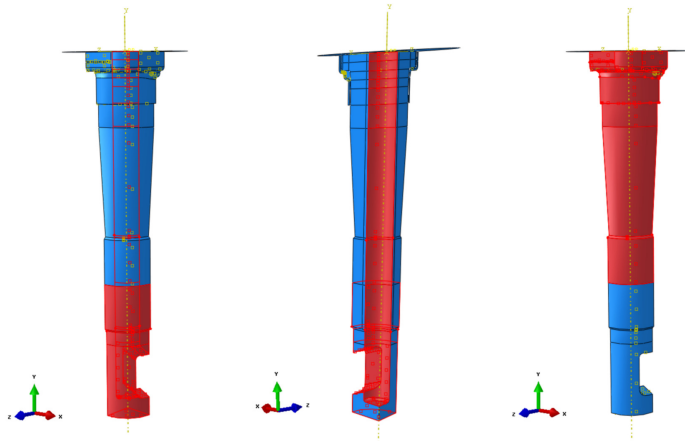


Figure 6.29: Left and center: surfaces directly in contact with the molten metal. Right: surfaces subject to air convection.

the procedure described in Sec. 6.4.

Postprocessing

The thermal-stress analysis shows the gradual temperature increase from the surfaces in direct contact with the liquid metal, until the steady state temperature distribution in the model is reached. It is particularly interesting to note how the inner part

of the submerged pouring tube shows a lower temperature with respect to the external surfaces for about one minute from the beginning of the casting process (Fig. 6.31).

By post-processing the mechanical analysis we note a particularly high Von-Mises stress on the top of the tube, due to the action of the applied pressure. The location of the maximum stress shown in Fig. 6.32 is consistent with the crack development observed during actual use of the refractory device (see Fig. 6.30).

Figure 6.30 shows the values of p_c and $p_{c_{max}}$ in the critical zone during the numerical simulation. The calibrated constitutive model is able to predict the crack development during casting, when the value of p_c reaches $p_{c_{max}}$.

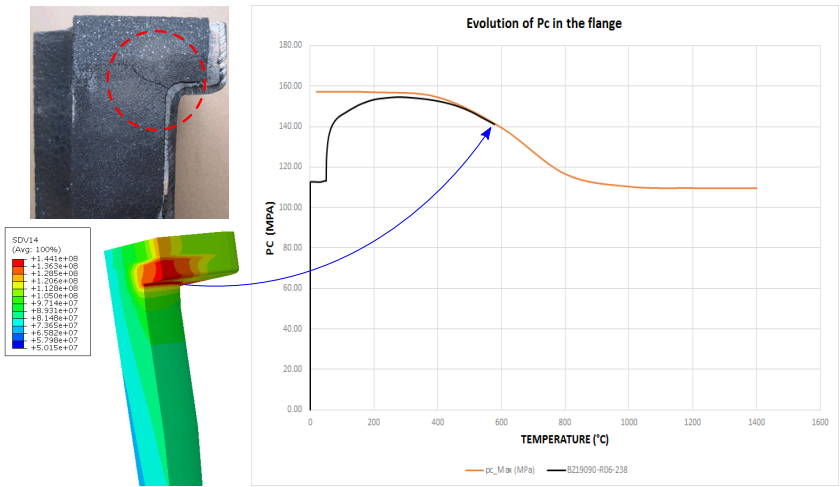


Figure 6.30: Prediction of crack formation on the top part of the Sub-Entry Nozzle under working conditions, when p_c meets $p_{c_{max}}$.

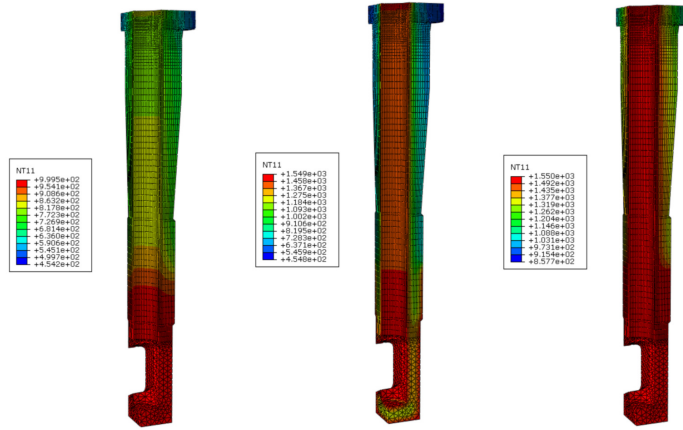


Figure 6.31: Temperature distribution in refractory VISO - tube at different time steps of the casting process. Respectively after one second, one minute and one hour.

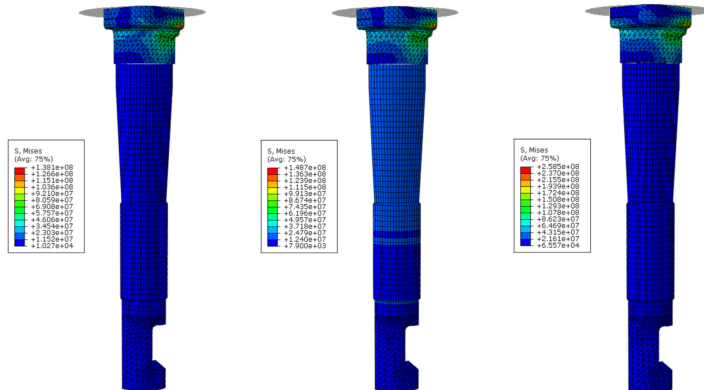


Figure 6.32: Von Mises stress in refractory VISO - tube at different time steps of the casting process. Respectively after one second, one minute and one hour.

Chapter 7

The unified constitutive model for ceramic powder densification and pre-sintering

In the industrial process for the production of ceramic devices, targeted material micro-structure and density are achieved through significant inelastic deformations and temperature changes.

During the cold forming process, the loose ceramic powder is densified through extrusion or compaction in rigid moulds at room temperature. The green bodies obtained this way are subsequently heated, with the purpose of initiating the sintering process.

Remarkable influence of density and temperature on the mechanical strength of ceramic materials is suggested by several experimental tests [1, 2, 14]. However, thermo-plastic models accounting for the flexible evolution of the yield locus as a function of density and temperature are still not available.

The present Chapter introduces a phenomenological constitutive model focused on the description of the behavior of ceramics subject to prominent plastic deformations and temperature loads, with emphasis on the pre-sintering phase, where specific experiments [2] show a reduced mechanical strength of the investigated materials.

The model has proven to correctly describe the behavior of alumina during the compaction process and subsequent uniaxial compression tests at different temperatures on the formed green bodies. This result has been accomplished thanks to a particu-

lar formulation of the Bigoni-Piccolroaz yield surface, that allows shape evolution, combined with the identification of constitutive parameters through multi-objective optimization.

7.1 Thermo-plastic constitutive formulation

The most peculiar capability of the constitutive model presented herein is the possibility of ‘shape evolution’: the parameters of the BP yield function (see Sec. 2.4), can evolve during the analysis, changing radically the form of the elastic locus.

This evolution is particularly important in the process of powder compaction, as detected in the experimental tests performed by Piccolroaz et al. [14] and Bosi et al. [1]. In particular, the experiments revealed remarkably different BP yield surface shapes for loose powder and formed green bodies.

Increased resistance to deviatoric loads that depends on the material density is achieved through a proper density-dependent hardening rule, which is described in Sec. 7.1.4.

A particular plastic potential is introduced, so that a linear combination of two different hardening contributions is adjusted depending on the plastic flow direction.

Thermal softening and temperature-dependent hardening are also included in the proposed constitutive model. The dependence on the temperature is considered with the goal of reproducing the material behavior observed in the experimental tests performed by Gupta et al. [2] where, before sintering is completely activated, elastic modulus, yield strength and ultimate strength in simple compression tests decrease by increasing the temperature of the samples.

7.1.1 The evolution of the BP yield surface

In the most common models for plasticity (see Sec. 2.1.2), hardening increases the size of the considered yield surface, while its proportions are usually kept constant. In the BP yield criterion, this effect can be achieved by imposing a dependence of the isotropic compressive strength p_c on the plastic deformation ε_p .

However, the assumption of a constant-shape yield surface is often far from being correct, especially if the material is subject to large deformations and thus in case of powder densification. In particular, reference BP yield function parameters for alumina loose

powder and aluminum silicate green bodies were experimentally identified respectively by Piccolroaz et al. [14] and Bosi et al. [1].

An improved implementation of the BP criterion allows shape evolution of the elastic domain during the deformation process (see Figures 7.1 and 7.2), by imposing a dependence of the yield function parameters listed in Eq. (2.61) on the plastic strain ε_p .

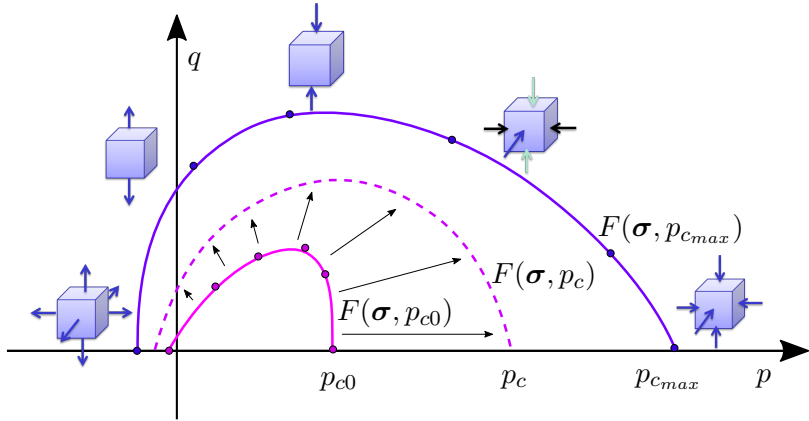


Figure 7.1: Example of evolution of the meridian shape of the BP yield function during a simulation. The calibration of the yield function shape of the loose powder (first yielding) $F(\sigma, p_{c0})$ and of the formed green body $F(\sigma, p_{c_{max}})$, should be based on multiple experimental tests. The meridian shape of the yield function is influenced by M , m and α .

The parameter c , which represents the isotropic tensile yield strength of the material, can both be constant or evolve during the process as

$$c = \omega p_c \tag{7.1}$$

so that, if ω is a constant, p_c and c will maintain their proportion during the analysis.

The evolution can be efficiently customized when experimental tests make available the BP parameters at the onset of plasticity and at a following state, for example the end of the compaction process or the failure of the sample.

The evolution of the yield function parameters M , m , α , β and γ is enforced through a linear dependence on the compressive isotropic strength of the material parameter p_c .

In the current implementation of the constitutive model the evolution of the yield function can also be subject to the condition $p_c \leq p_{c_{max}}$. In this case, if $p_{c_{max}}$ corresponds to the isotropic

Note that p_c evolves during the analysis according to Eq. (7.11).

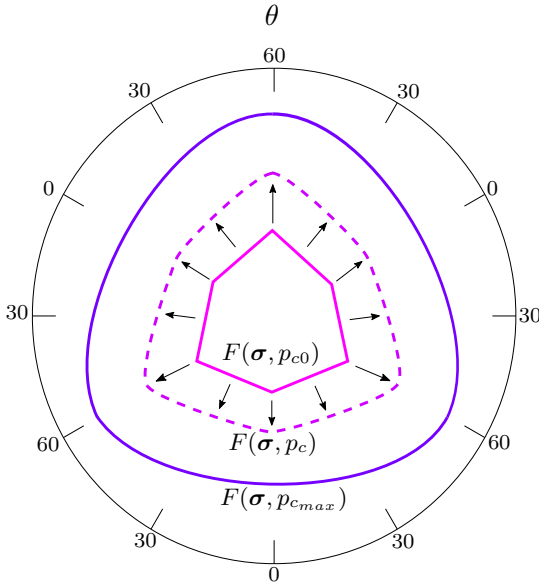


Figure 7.2: Example of evolution of the deviatoric shape of the BP yield function during a simulation. The BP yield function parameters that influence the deviatoric shape are β and γ .

strength at the end of the compaction process, we obtain that the yield function shape evolves only during densification. Consequently, the increase of plastic strain during the unconfined uniaxial deformation tests on formed green bodies is assumed not to influence the shape of the yield function, while changing its size.

As an example, the evolution of parameter M can be described as

$$M(p_c) = \begin{cases} M_{max} - \frac{(p_{c_{max}} - p_c)}{(p_{c_{max}} - p_{c_0})} (M_{max} - M_0) & \text{if } p_c \leq p_{c_{max}} \\ M_{max} & \text{if } p_c > p_{c_{max}} \end{cases} \quad (7.2)$$

where $p_{c_{max}}$ and M_{max} are, respectively, the compressive isotropic stress and the yield function parameter M at the desired time-step (e.g. at the end of the compaction phase). The parameters p_{c_0} and M_0 are respectively the compressive isotropic stress p_c and the parameter M at first yielding.

It should be noted that relationships different from Eq. (7.2), for example based on the relative density of the sample, could alternatively be selected for the evolution of the BP yield function parameters.

The parameter $p_{c_{max}}$ can be identified through triaxial experimental tests.

7.1.2 Elastic potential and temperature dependence

The experimental tests performed by Gupta et al. [2] have shown the dependence of the elastic properties of alumina on temperature.

Therefore, in the same way as reported in Sec. 6.1.1 for refractory materials, the elastic potential is written as

$$W(T, \boldsymbol{\varepsilon}) = \frac{\lambda(T)}{2} \text{tr } \boldsymbol{\varepsilon}^2 + \mu(T) \boldsymbol{\varepsilon}^2, \quad (7.3)$$

where $\lambda(T)$ and $\mu(T)$ are the Lamè constants. In the following, we consider a temperature-dependent Young's modulus $E(T)$ and a constant Poisson ratio ν . Consequently, the Lamè constants are obtained as

$$\lambda(T) = \frac{E(T)}{(1 + \nu)(1 - 2\nu)}, \quad (7.4)$$

and

$$\mu(T) = \frac{E(T)}{2(1 + \nu)}. \quad (7.5)$$

The experimental data suggest the following relationship for the elastic modulus

$$E(T) = \frac{E_0}{e^{-E_3 \cdot (1 - \frac{T}{T_0})}}, \quad (7.6)$$

where

$$E_3 = C + \tilde{E} \cdot (T - T_{02})^2. \quad (7.7)$$

In the above relationships T_0 is the reference temperature, whereas the material parameters E_0 , E_3 , C , \tilde{E} , and T_{02} have been identified by inverse analysis, as specified in Section 7.3.

7.1.3 Plastic potential and non-associative flow rule

As already mentioned, the proposed constitutive model was formulated for non-associative plasticity. In particular, the following plastic potential G is introduced

$$G(q, p) = \frac{(p - \Delta_p)^2}{a^2} + \frac{q^2}{b^2} - 1, \quad (7.8)$$

where a and b are the p -axis and q -axis of the ellipse, respectively. Eq. (7.8) defines a shiftable ellipse in the p - q space. The material parameter Δ_p determines the shift of the ellipse along the p axis, see Fig. 7.3.

This parameter can also be defined as a function of the current values of p and q , so that the ellipse varies its position depending on the stress point (\hat{p}, \hat{q}) along the loading path. Assuming a linear dependence on \hat{q} only, Eq. (7.8) becomes

$$G(q, p) = \frac{(p - \Delta_p \hat{q})^2}{a^2} + \frac{q^2}{b^2} - 1. \quad (7.9)$$

The vector \mathbf{P} (see Eq.(2.32)) is therefore written as

$$\mathbf{P} = \left. \frac{\partial G}{\partial \boldsymbol{\sigma}} \right|_{\hat{q}=\text{const}}. \quad (7.10)$$

Figure 7.3 shows the operating principle of the proposed non-associative constitutive model. The BP yield function describes the elastic enclosure, while the plastic flow direction is determined by the gradient of the plastic potential G .

The ratio between the major and minor axes of the ellipse regulates the plastic flow direction, which is not influenced by the effective size of the ellipse.

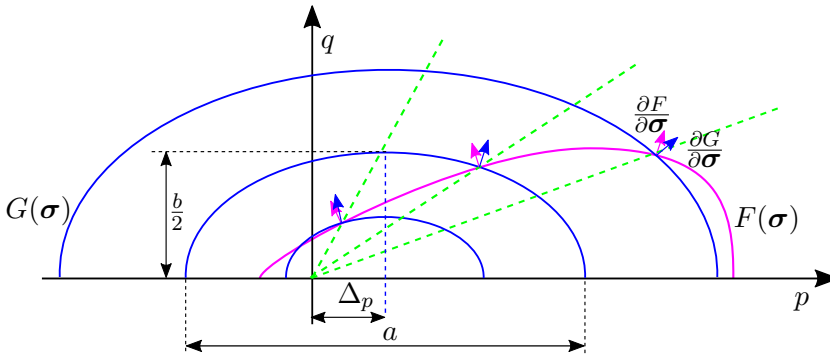


Figure 7.3: Plastic potential function $G(\boldsymbol{\sigma})$ for constant Δ_p and BP yield function $F(\boldsymbol{\sigma})$ in the p - q plane. The plastic flow direction is shown for three arbitrary loading paths.

7.1.4 Density-dependent strain hardening

The proposed hardening formulation takes separately into account the contributions of isotropic and deviatoric plastic strain.

The increase of isotropic strength p_c , which also regulates size/shape of the yield function, must satisfy the following condition

$$p_c - p_{c_0} + p_{c_T} = H_1 - \eta H_2, \quad (7.11)$$

where

$$H_1 = \frac{\Lambda_1}{\log \frac{-\text{tr} \boldsymbol{\varepsilon}_p}{a1} + \exp \frac{-\Lambda_1}{p_{c_0}}}, \quad (7.12)$$

$$H_2 = \frac{k_1(T)}{\delta(T)} \frac{(1 + J_{2p})^{n-1} - 1}{(n-1)(1 + J_{2p})^{n-1}}, \quad \text{where } n \neq 1, \quad (7.13)$$

$$J_{2p} = \left| \boldsymbol{\varepsilon}_p - \frac{\text{tr} \boldsymbol{\varepsilon}_p}{3} \right|, \quad (7.14)$$

being Λ_1 , $a1$, $k1$, n , δ the material parameters regulating the hardening. The parameter p_{c_0} is the initial (small) isotropic strength of the ceramic powder, while p_{c_T} is defined by Eq. (7.19) and is active only at high temperature.

The following dependencies on the temperature are introduced for $k_1(T)$ and $\delta(T)$

$$k_1(T) = A_k + B_k \tanh \left(\frac{T - T_{0k}}{C_k} \right), \quad (7.15)$$

$$\delta(T) = \delta_0 \cdot \exp \delta_3 \cdot \left(1 - \frac{T}{T_0} \right), \quad (7.16)$$

where

$$\delta_3 = C_\delta + \tilde{\delta} \cdot (T - T_{0_\delta})^2, \quad (7.17)$$

with A_k , B_k , T_{0k} , C_k , $\tilde{\delta}$, C_δ and T_{0_δ} constant material parameters, while T_0 is the reference temperature.

Equations (7.12) and (7.13) define the proposed hardening laws, depending respectively on isotropic and deviatoric plastic strain.

Expression (7.12) is based on the micromechanical model proposed by Cooper and Eaton (1962), where a single exponential function is considered for simplicity. The relationship (7.13) was obtained through modification of the hardening law proposed by Poltronieri et al. [39] for concrete.

The combination of different hardening laws is motivated by the usual low resistance of poorly densified samples subject to deviatoric loading. Therefore, the parameter η , which regulates the deviatoric hardening in Eq. (7.12), is assumed to depend on the relative density of the material in the following way

$$\eta(\rho_R) = \frac{\tanh\left(B\left(\rho_R - \frac{\rho_{R1} + \rho_{R0}}{2}\right)\right) + 1}{2}. \quad (7.18)$$

The relationship between parameter η and relative density is shown in Figure 7.4: depending on B , the value of η increases more or less rapidly, while ρ_{R1} and ρ_{R0} regulate respectively start and end of its transition between 0 and 1.

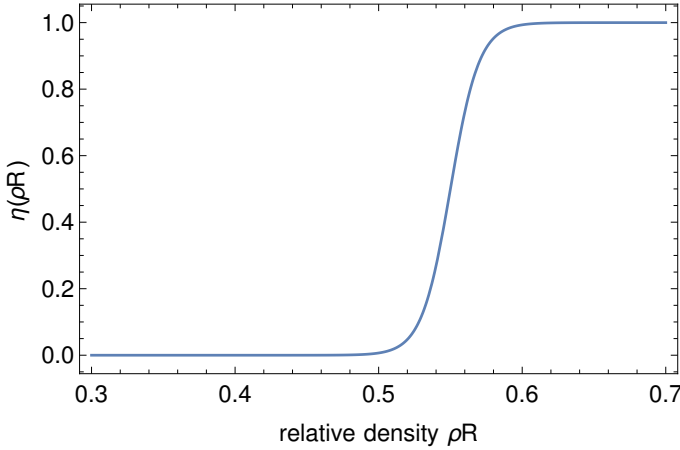


Figure 7.4: Dependence of parameter η (Eq. (7.18)) on the relative density.

7.1.5 Thermal softening

The experimental results presented by Gupta et al. [2] show a clear reduction of the yield strength of the samples by increasing their temperature. This effect can be efficiently reproduced by introducing thermal softening in the constitutive model. The isotropic yield strength of the material p_c is lowered depending on temperature, so that the yield function ‘shrinks’ homothetically, yielding to lower yield stress for each possible loading path.

The parameter p_{cT} influences the value of p_c in expression (7.11) depending on temperature. The following relationship

$$p_{cT} = A_{p_c} + B_{p_c} \tanh\left(\frac{T - T_{0p_c}}{C_{p_c}}\right), \quad (7.19)$$

has shown to fit in a particularly good way the results of experimental tests on alumina green bodies at pre-sintering temperatures.

In Section 7.3, the procedure for the identification of the material parameters A_{p_c} , B_{p_c} , T_{0p_c} and C_{p_c} from the results of the experimental tests is explained in detail.

7.2 Experimental tests and numerical simulation of cold forming and pre-sintering of alumina

Finite element simulations with the thermo-plastic material model have been carried out in Abaqus both for compaction of alumina powder and unconfined compressive tests of formed green bodies at pre-sintering temperatures. The analyses have been performed in a single process: uniaxial compression is applied to the same green bodies obtained from cold forming of alumina. In this way, at each step of the analysis the mechanical properties of the material depend on its complete loading history.

The numerical results have been compared to the available experimental data, which are obtained from the literature as specified in the following.

7.2.1 Forming of cylindrical green bodies

The experimental data for powder compaction of alumina are made available by Piccolroaz et al. [14]. In this paper, Piccolroaz analyzes uniaxial deformation tests on cylindrical samples at different forming pressures $\sigma_1 = \{60, 80, 100, 120\}$ MPa. Force-displacement curves were produced from the performed tests.

Piccolroaz et al. [14] also identified the shape of the BP yield function for undensified alumina. Specifically, the BP parameters $m_0=2$, $\alpha_0=0.1$, $\beta_0=0.19$, $\gamma_0=0.9$ and $M_0=1.1$ are indicated for the loose ceramic powder.

These BP yield function parameters therefore define the initial shape of the yield surface (see Section 7.1.1).

Conversely, the yield surface shape at the end of the compaction process is assumed to be similar to that identified by Bosi et al. [1]. Through a series of triaxial tests at different confining pressures, Bosi was able to numerically identify the BP parameters for aluminum silicate green bodies. The yield points corresponding to the examined loading paths were used for the calibration.

Accordingly, the assumed BP parameters at the end of the compaction process are $m_{max}=4.38$, $\alpha_{max}=1.95$, $\beta_{max}=0.10$, $\gamma_{max}=0.9$ and $M_{max}=0.25$.

7.2.2 Uniaxial compression tests at pre-sintering temperatures

In the uniaxial compression tests performed by Gupta et al. [2], extruded alumina specimens have been heated at different temperatures. The cylindrical samples were either 8 mm in height and 8mm in diameter or 26 mm in height and 18 mm in diameter.

The experimental tests showed a strong decrease of the mechanical properties of the green bodies by increasing the temperature up to 500 °C. In particular, the UCS (Unconfined compressive strength) and the yield stress both reduce as a consequence of temperature.

On the contrary, at temperatures higher than 1000 °C the mechanical properties of the samples start to increase again. This effect is due to the beginning of sintering and will not be analyzed in the following simulations.

The experimental tests made available stress-strain curves at 25, 190, 250 and 500 °C, which have been compared to numerical simulations with the proposed constitutive model.

7.2.3 Thermo-mechanical FE analysis

The performed simulation can be divided into four main steps:

1. **Ceramic powder densification by uniaxial deformation:** a vertical pressure of 32 MPa is applied on transversally confined cylindrical samples, which are modeled with axis-symmetric elements. The forming pressure has been calibrated to obtain green bodies with mechanical properties equivalent to those of the samples investigated by Gupta et al. [2].
2. **Unloading and extraction:** the vertical pressure is progressively reduced until complete unloading of the FE model. The extraction of the sample is then simulated by deactivating the lateral boundary conditions.
3. **Heating at pre-sintering temperature:** the unloaded sample is uniformly heated at one of the considered pre-

sintering temperatures $\{25, 190, 250, 500\}$ C°. This condition is then maintained for the rest of the analysis.

4. **Uniaxial compression:** on the upper face of the FE model a fixed displacement (greater than the measured displacement of the samples at failure) is imposed.

The constitutive parameters governing the material response have been obtained from the available experimental data and with a peculiar optimization strategy, which is described in following Sec. 7.3.

7.3 Material parameters identification by inverse analysis

Some material parameters influence only particular responses of the proposed constitutive model. Thus, different numerical strategies have been independently employed for the identification of small groups of parameters. This strategy is particularly efficient, since it reduces the size of the optimization problem and enhances the precision of the identified parameters.

In the following, the single procedures carried out for the identification of the constitutive parameters are explained in detail.

7.3.1 Temperature dependent elastic modulus

The elastic modulus of alumina green bodies at the considered temperatures $T = \{25, 190, 250, 500\}$ °C has been determined from the experimental results made available by Gupta et al. [2], by evaluating the steepness of the first linear-elastic part of the stress-strain curves. The obtained values are summarized in Table 7.1.

T [°C]	E [MPa]
25	945.17
190	424.69
250	307.66
500	8.6

Table 7.1: Values of the elastic modulus in the experimental tests of Gupta et al. [2].

Equation (7.6) expresses the proposed dependency of the elastic modulus on temperature. The parameters T_0 and E_0 represent respectively the reference temperature and the associated elastic modulus. The parameters C , \tilde{E} , T_{02} , have been obtained through least squares regression with Wolfram Mathematica. Figure 7.5 shows expression (7.6) computed with the identified parameters and the experimental values of the elastic modulus.

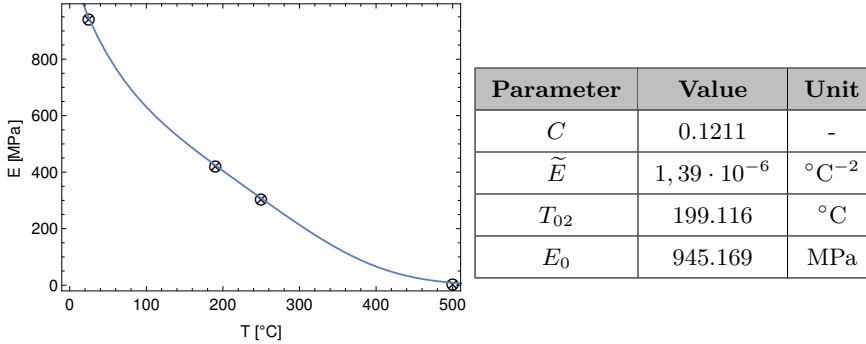


Figure 7.5: Experimental values of the elastic modulus and proposed relationship for $E(T)$ (see Eq. (7.6)) with the identified material parameters.

7.3.2 Thermal softening

The implementation of thermal softening aims to reduce the yield stress as a consequence of temperature increase. The values of yield stress can be obtained from the experimental stress-strain curves provided by Gupta et al. [2], by measuring the stress corresponding to the first non-linear response of the material.

The experimental values of split tensile strength allow an estimation of the tensile yield stress within a sufficiently small range. The yield stress values at the considered temperatures are listed in Tab. 7.2.

The increase of temperature reduces the size of the BP yield function, modifying p_c according to expression (7.19). However, temperature is assumed to have no effect on the yield surface shape (see Section 7.1.1). Accordingly, the parameters M , m , α , β and γ result unaffected.

The values of p_c and c at the considered temperatures can be found by forcing the yield surface to intercept the yield stresses σ_{yt} and σ_{yc} provided in Tab. 7.2.

T [°C]	σ_{yt} [MPa]	σ_{yc} [MPa]	p_c [MPa]
25	0.959 - 1.163	5.676	50.88
190	0.733 - 1.016	3.98	35.60
250	0.4 - 0.6	1.997	17.50
500	0.0066 - 0.0106	0.040893	0.35

Table 7.2: Yield stresses in tension σ_{yt} and compression σ_{yc} and identified compressive isotropic strength p_c at the considered temperatures for the experimental tests of Gupta et al. [2].

The dependence of c and p_c on the temperature appears very similar, so that the ratio $\Omega = c/p_c$ results well-approximated by the constant value 0.0105.

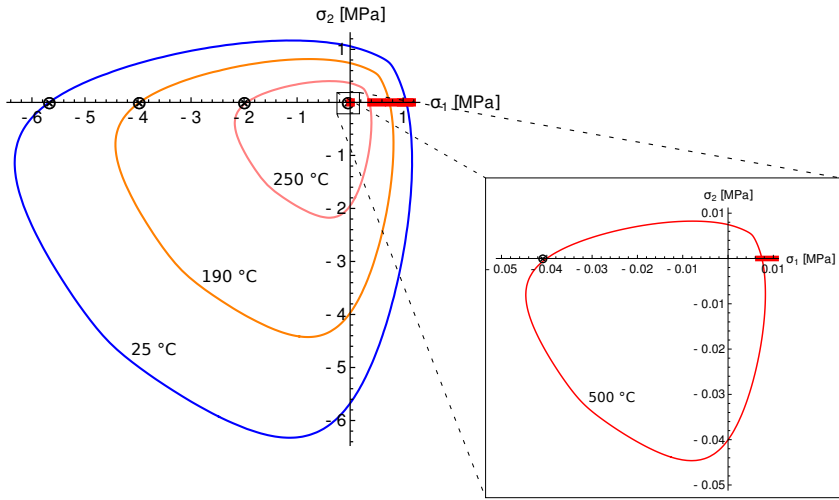


Figure 7.6: BP yield criterion at the considered temperatures $T = \{25, 190, 250, 500\}$ °C: the yield function shrinks homothetically according to the governing parameter p_c (see (7.19)).

Figure 7.6 shows the BP yield surface in the $\sigma_1 - \sigma_2$ biaxial plane for the values of p_c at the considered temperatures, which are listed in Table 7.2.

Given the values of p_c (see Tab 7.2) at the selected temperatures, the material parameters appearing in expression (7.19) can be easily obtained through least squares regression. Figure 7.7 shows the variation of p_c at the end of compaction phase depend-

ing on temperature with the identified parameters.

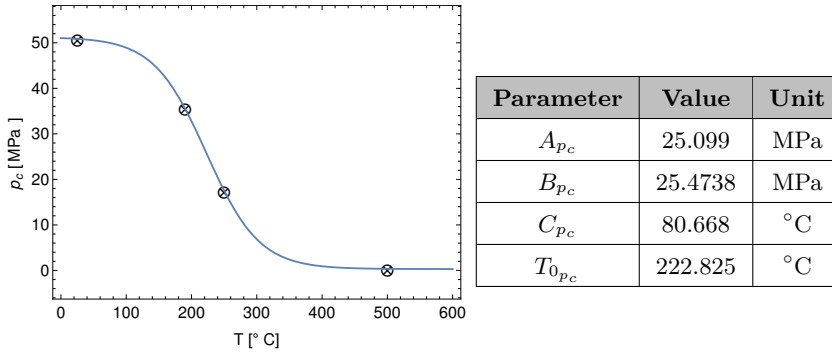


Figure 7.7: Dependence of hardening parameter p_c and identified parameters for relationship (7.19).

7.3.3 Hardening laws

The parameters governing the hardening laws (7.12), (7.13) and the transition law (7.18) are of difficult analytical or experimental identification.

For this reason, their determination has been carried out by inverse analysis, by coupling the FE simulation (see Section 7.2) to the extensible optimization algorithms available in the Dakota Framework [16].

The iterative optimization has the goal to minimize the discrepancy between numerical and experimental stress-strain curves.

The procedure can be divided in the following three main steps:

1. Identification of parameters for the isotropic hardening law (7.12) (Λ_1, a_1), for the transition law (7.18) (B, ρ_1, ρ_0) and for the deviatoric hardening law (7.13) ($k1, \delta, n$) at $T=25$ °C by hybrid multi-objective optimization (see Sec. 4.1.3). The entire parameters domain is first explored with a genetic algorithm (moga). After this, the best solutions are refined with a local optimization algorithm (pattern-search). The choice of derivative-free optimization methods enhanced the robustness of the procedure.
2. Identification of deviatoric hardening parameters $k1$ and δ at $T= 190, 250, 500$ °C by employing a local optimization

method (pattern-search).

The remaining material parameters determined at step 1 are kept constant. At each temperature, the starting value for k_1 and δ are those obtained at step 1. The identified parameters at the considered temperatures are listed in Table 7.3.

3. Identification of the parameters for expressions (7.15) and (7.17), namely A_k , B_k , T_{0k} , C_k , $\tilde{\delta}$, C_δ and $T_{0\delta}$, which regulate the evolution of k_1 and δ depending on temperature. The results of the optimization at step 2 are provided as targets for a least squares regression carried out with Wolfram Mathematica.

Figures 7.8 and 7.9 show k_1 and δ depending on temperature.

T [°C]	δ [-]	k_1 [MPa]
25	284.989	155933
190	298.167	110397
250	331.038	66070.4
500	2538.95	5955.19

Table 7.3: Values of the parameters k_1 and δ at the considered temperatures identified through inverse analysis.

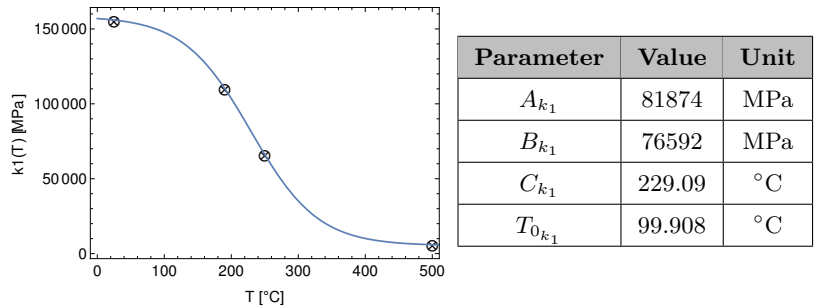


Figure 7.8: Dependence of hardening parameter $k_1(T)$ on the temperature and identified parameters appearing in expression (7.15).

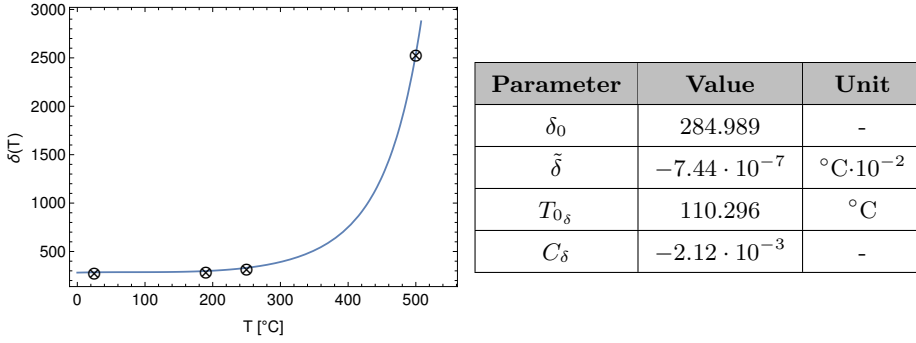


Figure 7.9: Dependence of hardening parameter $\delta(T)$ on the temperature and identified parameters appearing in Eq. (7.16).

7.4 Results and comparison with experimental tests

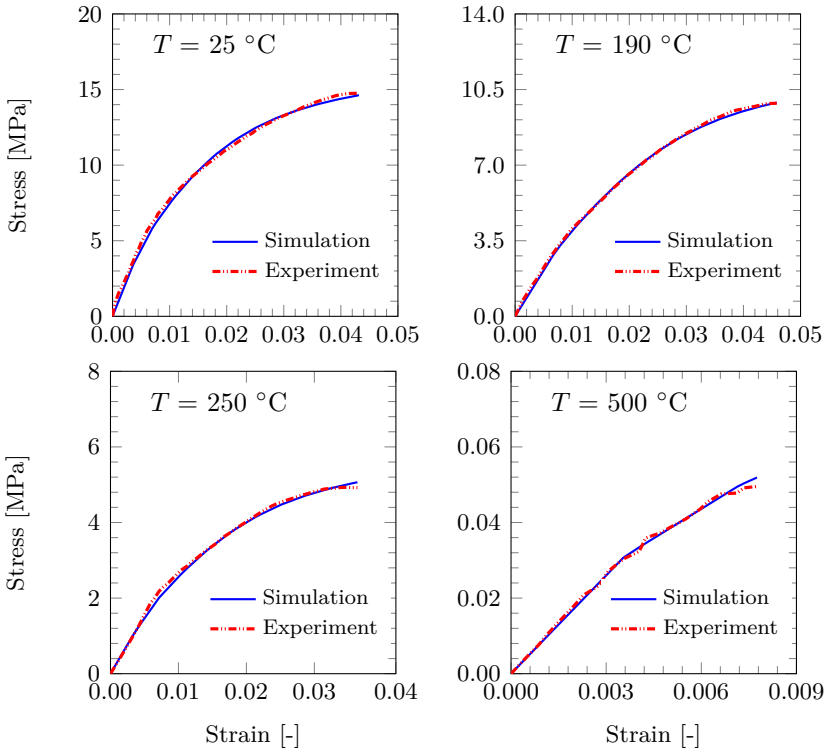


Figure 7.10: Comparison between numerical simulations and experimental tests on alumina green bodies reported by [2]. The results are shown at the considered temperatures $T=\{25, 190, 250, 500\}$ C $^{\circ}$.

The results of the simulations with the identified material parameters, which are summarized in Tab. 7.4, have been compared with the experimental results made available by Piccolroaz et al. [14] and Gupta et al. [2].

As shown in Figures 7.10 and 7.11, the discrepancy between numerical and experimental results is negligible. Good agreement is observed both during powder compaction and uniaxial compression of the green bodies at different temperatures.

At the beginning of the compaction phase (see Fig. 7.11), the numerical value of the stress appears slightly lower than in the experiments. Here, the results could be further optimized including a nonlinear elastic potential and elastoplastic coupling in the constitutive model. These improvements will be considered for future developments of the thermo-plastic formulation presented herein.

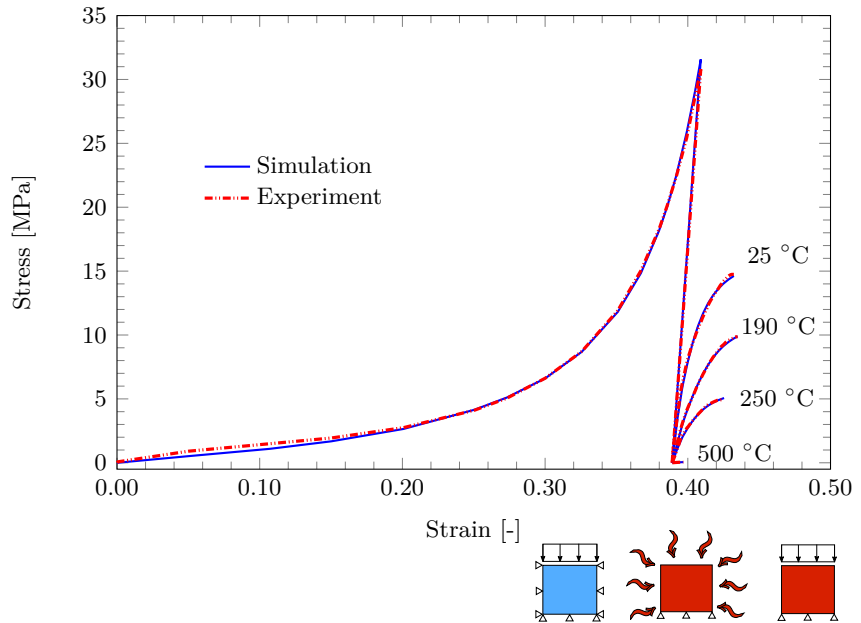


Figure 7.11: Comparison between numerical simulations (continuous line) and performed experimental tests (dashed line) [14] [2]. The alumina samples are first formed through uniaxial compaction, extracted from the cylindric mould, heated at the considered temperatures $T=\{25, 190, 250, 500\}$ C° and tested through unconfined uniaxial compression.

Parameters identified directly from experiments			
Elastic Properties	E_0	945.169	MPa
	\tilde{E}	$1,39 \cdot 10^{-6}$	$^{\circ}\text{C}^{-2}$
	C	0.1211	-
	T_{02}	199.116	$^{\circ}\text{C}$
	ν	0.37	-
Initial Yield Surface	p_{c0}	0.09	MPa
	M_0	1.1	-
	m_0	2.0	-
	α_0	0.1	-
	β_0	0.19	-
	γ_0	0.9	-
Final Yield Surface	Ω	0.0105	-
	p_{cmax}	50.87	MPa
	M_{max}	0.25	-
	m_{max}	4.38	-
	α_{max}	1.95	-
	β_{max}	0.1	-
Thermal Softening	γ_{max}	0.9	-
	A_{pc}	25.099	MPa
	B_{pc}	25.4738	MPa
	C_{pc}	80.668	$^{\circ}\text{C}$
	T_{0pc}	222.825	$^{\circ}\text{C}$
Parameters identified by multi-objective optimization			
Non-Associativity	a	400	-
	b	400	-
	Δ_p	0.333	-
Isotropic Hardening Law	Λ	3.228	-
	a_1	0.4188	-
Deviatoric Hardening Law	n	2.303	-
	A_{k_1}	81874.2	MPa
	B_{k_1}	76592	MPa
	C_{k_1}	229.085	$^{\circ}\text{C}$
	T_{0k_1}	99.9076	$^{\circ}\text{C}$
	δ_0	284.989	-
	$\tilde{\delta}$	$-7.44 \cdot 10^{-7}$	$^{\circ}\text{C} \cdot 10^{-2}$
	$T_{0\delta}$	110.296	$^{\circ}\text{C}$
Hardening Transition Law	C_{δ}	$-2.12 \cdot 10^{-3}$	-
	B	50	-
	ρ_0	0.5	-
	ρ_1	0.6	-

Table 7.4: Material parameters for cold forming and pre-sintering of alumina.

Bibliography

- [1] F. Bosi, A. Piccolroaz, M. Gei, F. Dal Corso, A. Cocquio, and D. Bigoni. Experimental investigation of the elastoplastic response of aluminum silicate spray dried powder during cold compaction. *J. Eur. Ceram. Soc.*, 34: 2633–2642, 2014.
- [2] S. Gupta, D.J. Green, and G.L. Messing. Thermomechanical behavior of ceramic green bodies during presintering. *J. Am. Ceram. Soc.*, 93(9): 2611–2615, 2010.
- [3] D. Bigoni and A. Piccolroaz. Yield criteria for quasibrittle and frictional materials. *Int. J. Solids Struct.*, 41:2855–2878, 2004.
- [4] Andrea Piccolroaz and Davide Bigoni. Yield criteria for quasibrittle and frictional materials: A generalization to surfaces with corners. *Int. J. Solids Struct.*, 46(20):3587 – 3596, 2009. ISSN 0020-7683.
- [5] D. Bigoni. *Nonlinear solid mechanics. Bifurcation theory and material instability*. Cambridge University Press, Cambridge, 2012.
- [6] R.M. Brannon and S. Leelavanichkul. A multi-stage return algorithm for solving the classical damage component of constitutive models for rocks, ceramics, and other rock-like media. *Int. J. Fract.*, 163:133–149, 2010.
- [7] S. Stupkiewicz, R. Denzer, A. Piccolroaz, and D. Bigoni. Implicit yield function formulation for granular and rock-like materials. *Comput. Mech.*, 54:1163–1173, 2014.
- [8] G. Duvaut and J. L. Lions. *Les Inequations en Mecanique et en Physique*. Dunod, Paris, 1972.
- [9] R. M. Brannon. Elements of phenomenological plasticity: Geometrical insight, computational algorithms, and topics in shock physics. In Yasuyuki Horie, editor, *ShockWave Science and Technology Reference Library*, volume 2, pages 187–274. Springer Berlin Heidelberg, Berlin, 2007.
- [10] R. M. Brannon, T. J. Fuller, O. E. Strack, A. F. Fossum, and J. J. Sanchez. Kayenta: Theory and user’s guide. *SANDIA REPORT*, 2015.
- [11] J. C. Simo and T. J. R Hughes. General return mapping algorithms for rate-independent plasticity. In C.S. Desai, editor, *Constitutive Laws for Engineering Materials*. Elsevier, New York, 21987.

- [12] Korelc J. Multi-language and multi-environment generation of nonlinear finite element codes. *Eng. with Comput.*, 18:312–327, 2002.
- [13] Korelc J. Automation of primal and sensitivity analysis of transient coupled problems. *Comput. Mech.*, 44:631–649, 2002.
- [14] A. Piccolroaz, D. Bigoni, and A. Gajo. An elastoplastic framework for granular materials becoming cohesive through mechanical densification, Part I: Small strain formulation. *Eur. J. Mech. - A/Solids*, 25(2):334 – 357, 2006.
- [15] G. Duvaut and J. L. Lions. *Inverse Problem Theory and Methods for Model Parameter Estimation*. . Society for Industrial and Applied Mathematics, Philadelphia, 2005.
- [16] B.M. Adams, L.E. Bauman, W.J. Bohnhoff, K.R. Dalbey, M.S. Ebeida, J.P. Eddy, M.S. Eldred, P.D. Hough, K.T. Hu, J.D. Jakeman, L.P. Swiler, and D.M. Vigil. Dakota, a multilevel parallel object-oriented framework for design optimization, parameter estimation, uncertainty quantification, and sensitivity analysis: Version 6.2 user’s manual. *Sandia Tech. Rep.*, 2015.
- [17] David E. Goldberg. *Genetic Algorithms in Search, Optimization and Machine Learning*. Addison-Wesley Longman Publishing Co., Inc., Boston, MA, USA, 1st edition, 1989.
- [18] Donald R. Jones, Matthias Schonlau, and William J. Welch. Efficient global optimization of expensive black-box functions. *J. Glob. Optim.*, 13(4):455–492, 1998. ISSN 1573-2916.
- [19] P.A. Cundall and O.D.L. Strack. Discrete numerical model for granular assemblies. *Geotech.*, 29(1):47–65, 1979.
- [20] P.A. Cundall. Formulation of a three-dimensional distinct element model, Part I: A scheme to detect and represent contacts in a system composed of many polyhedral blocks. *Int. J. Rock Mech. Min. Sci.* , 25(3):107–116, 1988.
- [21] R. Hart, P.A. Cundall, and J. Lemos. Formulation of a three-dimensional distinct element model, Part II: Mechanical calculations for motion and interaction of a system composed of many polyhedral blocks. *Int. J. Rock Mech. Min. Sci.* , 25(3):117–125, 1988.
- [22] S. Nosewicz, J. Rojek, K. Pietrzak, and M. Chmielewski. Viscoelastic discrete element model of powder sintering. *Powder Technol.*, 246:157–168, 2013.
- [23] J. Rojek, S. Nosewicz, K. Pietrzak, and M. Chmielewski. Simulation of powder sintering using a discrete element model. *Acta Mech. et Autom.*, 7(3):175–179, 2013. doi: 10.2478/ama-2013-0030.
- [24] C. Thornton and J. Lanier. Uniaxial compression of granular media: numerical simulations and physical experiment. In Behringer and eds. Jenkins, editors, *Powders & Grains 97*, pages 223–226. A.A.Balkema/Rotterdam/Brookfield, 1997.

-
- [25] J.-F. Jerier, B. Hathong, V. Richefeu, B. Chareyre, D. Imbault, F.-V. Donze, and P. Doremus. Study of cold powder compaction by using the discrete element method. *Powder Technol.*, 208(2):537–541, 2011. doi: 10.1016/j.powtec.2010.08.056.
- [26] C. O’Sullivan, J.D. Bray, and L. Cui. Experimental validation of particle-based discrete element methods. In *GeoCongress 2006: Geotechnical Engineering in the Information Technology Age*, volume 2006, page 5, 2006. doi: 10.1061/40803(187)5.
- [27] Subhash C. Thakur, Jin Y. Ooi, and Hossein Ahmadian. Scaling of discrete element model parameters for cohesionless and cohesive solid. *Powder Technol.*, 2015. ISSN 0032-5910. doi: <http://dx.doi.org/10.1016/j.powtec.2015.05.051>.
- [28] C. Della Volpe, G. Fronza, A. Pedrotti, and S. Siboni. Una nuova procedura per la determinazione non distruttiva della densità e della porosità di materiali di interesse archeologico. In *Atti del IV Congresso Nazionale AIA*, pages 253–254, 2006.
- [29] A. Piccolroaz, D. Bigoni, and A. Gajo. An elastoplastic framework for granular materials becoming cohesive through mechanical densification, Part II: The formulation of elastoplastic coupling at large strain. *Eur. J. Mech. - A/Solids*, 25(2):358 – 369, 2006.
- [30] M. Penasa, A. Piccolroaz, L. Argani, and Bigoni. Integration algorithms of elastoplasticity for ceramic powder compaction. *J. Eur. Ceram. Soc.*, 34(11):2775–2788, 2014.
- [31] S. Stupkiewicz, A. Piccolroaz, and D. Bigoni. Finite-strain formulation and fe implementation of a constitutive model for powder compaction. *Comput. Methods Appl. Mech. Eng.*, 283:856–880, 2014.
- [32] A. R. Cooper and L. E. Eaton. Compaction behavior of several ceramic powders. *J. Am. Ceram. Soc.*, 45(3):97–101, 1962. ISSN 1551-2916.
- [33] L. P. Argani, D. Misseroni, A. Piccolroaz, Z. Vinco, D. Capuani, and D. Bigoni. Plastically-driven variation of elastic stiffness in green bodies during powder compaction, Part I: Experiments and elastoplastic coupling. *ArXiv e-prints*, November 2015.
- [34] L. P. Argani, D. Misseroni, A. Piccolroaz, D. Capuani, and D. Bigoni. Plastically-driven variation of elastic stiffness in green bodies during powder compaction, Part II: Micromechanical modelling. *ArXiv e-prints*, November 2015.
- [35] T. Hueckel. On plastic flow of granular and rocklike materials with variable elasticity moduli. *Bull Acad Pol Sci Ser Sci Tech*, 23(8):665–674, 1975.
- [36] T. Hueckel. Coupling of elastic and plastic deformations of bulk solids. *Meccanica*, 11(4):227–235, 1976. doi: 10.1007/BF02128296.
- [37] J.W. Dougill. On stable progressively fracturing solids. *Z. Angew. Math. Phys.*, 27(4):423–437, 1976. ISSN 0044-2275. doi: 10.1007/BF01594899.

- [38] S. Stupkiewicz, A. Piccolroaz, and D. Bigoni. Elastoplastic coupling to model cold ceramic powder compaction. *J. Eur. Ceram. Soc.*, 34(11): 2839–2848, 2014. doi: 10.1016/j.jeurceramsoc.2013.11.017.
- [39] F. Poltronieri, A. Piccolroaz, and D. Bigoni. A simple and robust elastoplastic constitutive model for concrete. *Eng. Struct.*, 60:81–84, 2014.
- [40] A. Perez-Foguet, A. Rodriguez-Ferran, and A. Huerta. Consistent tangent matrices for substepping schemes. *Comput. methods applied mechanics engineering*, 190(35-36):4627–4647, 2001.
- [41] XX. Tu, J.E. Andrade, and QS. Chen. Return mapping for nonsmooth and multiscale elastoplasticity. *Comput. Methods Appl. Mech. Eng.*, 198(30-32):2286–2296, 2009. ISSN 0045-7825. doi: {10.1016/j.cma.2009.02.014}.
- [42] W.F. Chen and D.J. Han. *Plasticity for structural engineers*. Springer-Verlag, New York, 1988.

Three constitutive models for the mechanical description of the behavior of ceramic materials are developed, implemented into a numerical code, calibrated on experimental data, and validated.

-The first model is elastic-plastic and addresses the cold compaction of ceramic powders, combining nonlinear elasticity, elastoplastic coupling and increase of cohesion.

-The second model is thermal-viscous-elastic-plastic and is specifically tailored to describe the thermo-mechanical behavior of refractory devices under working conditions at high-temperature.

-The third model is thermal-elastic-plastic and implements a shape evolution of the BP yield function, calibrated to simulate the forming of green bodies and their pre-sintering phase.

Three algorithms are developed for the integration of constitutive equations when pathological yield functions are involved. The algorithms are coded in user material subroutines to be used in commercial FE softwares and their accuracy is evaluated in model problems allowing for semi-analytical solutions.

Material constitutive parameters are obtained from a combination of experimental tests and multi-objective optimization and employed in FE simulations of industrial processes, such as cold-forming of combed finish ceramic tiles and metal flow confinement by means of refractory devices.

This PhD thesis is the outcome of the secondment period at the Vesuvius Group, within the framework of the IAPP European project HOTBRICKS (contract number PIAPP-GA-2013-609758).

Massimo Penasa, received his M.Sc. in Civil Engineering at Vienna University of Technology (TU Wien - Austria) and the Engineer professional habilitation at the University of Trento (Italy), where he joins the Solid and Structural Mechanics Group. His Ph.D. research, which involved joint work between the University of Trento and the Vesuvius Group (Belgium), focused on the development of computational tools for virtual prototyping of industrial refractory devices under working conditions.